Canada

UNIVERSITY OF ALBERTA

SCANNING TUNNELING MICROSCOPY AND BALLISTIC ELECTRON
EMISSION MICROSCOPY IN METAL-SEMICONDUCTOR APPLICATIONS

BY

RONG ZHANG   ©

A thesis submitted to the Faculty of Graduate Studies and Research in partial fulfillment
of the requirements for the degree of MASTER OF SCIENCE

IN

METALLURGICAL ENGINEERING

DEPARTMENT OF MINING, METALLURGICAL AND PETROLEUM
ENGINEERING

EDMONTON, ALBERTA
FALL 1995

Your file   Votre référence

Our file   Notre référence

Canada

UNIVERSITY OF ALBERTA

LIBRARY RELEASE FORM

NAME OF AUTHOR: RONG ZHANG

TITLE OF THESIS: SCANNING TUNNELING MICROSCOPY AND
BALLISTIC ELECTRON EMISSION MICROSCOPY
IN METAL-SEMICONDUCTOR APPLICATIONS

DEGREE: MASTER OF SCIENCE

YEAR THIS
DEGREE GRANTED: 1995

Permission is hereby granted to the University of Alberta Library to reproduce single copies of this thesis and to lend or sell such copies for private, scholarly or scientific research purposes only.

The author reserves all other publication and other rights in association with the copyright in the thesis, and except as hereinbefore provided neither the thesis nor any substantial portion thereof may be printed or otherwise reproduced in any material from whatever without the auther's prior written permission.

<div align="right">

signature

1, 10620 - 83AVE
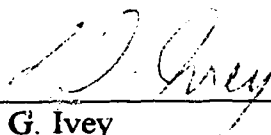
Edmonton, Alberta, Canada T6E 2E2

</div>

Date: Oct 2/95
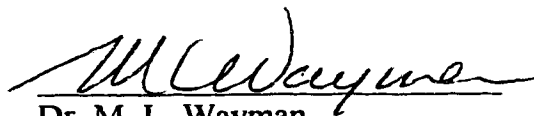
UNIVERSITY OF ALBERTA

FACULTY OF GRADUATE STUDIES AND RESEARCH
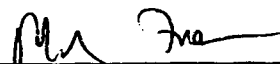
The undersigned certify that they have read, and recommend to the Faculty of Graduate Studies and Research for acceptance, a thesis entitled SCANNING TUNNELING MICROSCOPY AND BALLISTIC ELECTRON EMISSION MICROSCOPY IN METAL-SEMICONDUCTOR APPLICATIONS submitted by RONG ZHANG in partial fulfillment of the requirements for the degree of MASTER OF SCIENCE in METALLURGICAL ENGINEERING.

Dr. D. G. Ivey
Supervisor

Dr. M. L. Wayman

Dr. M. R. Freeman

Dr. J. L. Luo

Date: Sept 21/95

To Lucia

Abstract

Ever since the first demonstration of Binnig and Rohrer [1, 2] in early 1980s, Scanning Tunneling Microscopy (STM) has been shown to be unique among surface analysis techniques in that it allows measurements of geometric and electronic structure with extremely high vertical and lateral resolution. However, the contrast in the STM image includes the geometric and electronic structures of both the sample and the tip. Thus the geometric and electronic structure of the tip become extremely important in interpretation of the STM images, as well as the achievement of image resolution. The main goals of my research have been the fabrication of reproducible polycrystalline tungsten tips, the study of the tip geometry effects on the STM images, and tip electronic influences on image resolution.

Reproducible STM tips, prepared from polycrystalline W wire, were also used for the topographic study of the Au/InP system after annealing. Tips were prepared by electrochemical polishing or a combination of electrochemical polishing and ion milling.

An important new technique that has emerged from the STM for the study of the subsurface interface electronic structure is Ballistic Electron Emission Microscopy (BEEM). It utilizes STM in a three-electrode configuration, allows characterization of interface properties and measurement of Schottky barriers with nanometer spatial resolution.

Modification of an existing STM to BEEM is carried out, including the design of electronic circuitry and programming. The performance of electronic circuits and the quality of the interfaces will have dominant effects on BEEM. BEEM studies on the

Au/Si (100) system show that the modification is successful. Initial experiments of BEEM on metal/InP systems have been carried out. Although these trials have failed, further directions of BEEM measurements on these systems are proposed.

Acknowledgments

Table of Contents

PART 2

List of Tables

List of Figures

Appendices

Appendix

Abbreviations

AES	Auger Electron Spectroscopy
AFM	Atomic Force Microscopy
AMC	Alberta Microelectronic Center
API	Application programming interface
BEEM	Ballistic Electron Emission Microscopy
CBED	Convergent Beam Electron Diffraction
EBD	Electron Beam Deposition
EDX	Energy Dispersive X-ray
FIM	Field Ion Microscopy
HOPG	Highly Oriented Pyrolytic Graphite
IAD	Ion Assisted Deposition
PZT	$Pb(Zr, Ti)O_3$
RIE	Reactive Ion Etch
SAD	Selected Area Diffraction
SE	Secondary Electron
SEM	Scanning Electron Microscopy
SPM	Scanning Probe Microscpe
STM	Scanning Tunneling Microscopy
TEM	Transmission Electron Microscopy
UHV	Ultra High Vacuum
WKB	Wentzel-Kramers-Brillouin

Symbols

a	the diode junction area
A^*	the Richardson constant
d_{ij}	the piezoelectric constant
$d(\vec{u})$	the electron path length through the metal film
$d\Omega$	the solid-angle segment with direction $\vec{u}$
D	the tube diameter
D (E)	tunneling probability
E	the electron energy
E_F	Fermi energy
E_M^o	the conduction band minimum in the metal layer
E_S^o	the conduction band minimum in the semiconductor ($E_S^o = V_b$)
E_{th}	the ionization threshold
E_x	energy component parallel to the interface
F (E,V,T)	the Fermi function of the tip electrons at temperature T
$\hbar$	Planck's constant divided by 2π
I_c	BEEM current or collector current
k_1	the spring constant of the isolation stage
k_2	the spring constant of the tunneling unit
k	Bolzman's constant
$\vec{k}$	electron momentum
k_t	momentum component parallel to the interface
k_{tM}	momentum component parallel to the interface in the metal layer
k_{tS}	momentum component parallel to the interface in the semiconductor layer
k_x	momentum component perpendicular to the interface
k_{xM}	momentum component perpendicular to the interface in the metal layer

k_{xS}	momentum component perpendicular to the interface in the semiconductor layer
l	the length of the tube or bar scanner
m	the free-electron mass
m_1	the effective mass of the isolation stage
m_2	the effective mass of the tunneling unit
m_s	the effective mass in the semiconductor
m_{ts}	the component of the effective mass in the semiconductor parallel to the interface
P_{ii}	the probability for excitation of a secondary electron
R_{ac}	the average surface roughness
R_{qc}	root-mean-square roughness
R_t	peak-to-peak roughness
R_o	the diode resistance
s	the barrier width (tip-sample separation)
t	the thickness of the tube or bar
T	the absolute temperature
$T(E, \bar{k})$	the transmission probability at the interface
T_1	transfer function of the isolation stage to the external vibration
T_2	transfer function of the tunneling unit to the isolation stage
$\bar{u}$	the direction of the electron path length through the metal film
U	the barrier height
V	the bias voltage
V_b	the Schottky barrier of the interface
V_p	the applied voltage to the piezoelement
W	the depletion width
x_i	the displacement of the isolation stage
x_t	the displacement of the tunneling unit

x_b	the amplitude of the displacement of the floor
Z	overall transfer function of the tunneling unit to the external vibration
Z_1	transfer function of the isolation stage to the external vibration
Z_2	transfer function of the tunneling unit to the isolation stage
Z_i	the absolute height value in a profile
Z_{max}, Z_{min}	the highest and lowest height values in a profile
Z_m	the average height in a profile
λ_B	the ballistic mean free path
λ_ε	the mean free path of inelastic scattering
λ_σ	the mean free path of elastic scattering
λ_{ii}	the mean-free path of impact ionization
γ_i	the damping factor of the isolation stage
γ_t	the damping factor of the tunneling unit
μ	$\sqrt{\dfrac{2m(U-E)}{\hbar^2}}$
ω_i	the eigenfrequency of the isolation stage
ω_t	the eigenfrequency of the tunneling unit
θ_c	the critical angle
$\psi(x)$	the wave representation of an electron

CHAPTER 1. INTRODUCTION

Scanning Tunneling Microscopy (STM), which was invented by Binnig and Rohrer in the early 1980s [1, 2], has the unique capability to image the surface geometry and electronic structure with atomic resolution. The concept of STM is based on a blend of quantum physics, mechanical design and electronic control. A sharp metal tip is brought within a nanometer distance from a conducting surface while a voltage is applied between them. The distance between the tip and the sample is so small that electrons can tunnel from the very end of the tip to the nearest atom on the surface and generate a current. The tunneling current decreases an order of magnitude for approximately every 0.1 nm increase in gap separation. This current is compared with a reference current and generates an error signal, which is applied to a position transducer to move the tip in order to maintain a constant current as the tip is rastered across the sample.

One of the most crucial components of STM is the tunneling tip. Both the geometry (shape and sharpness) and chemical identity (electronic states) of the tip influence the resolution and topographic images. It is usually believed that the best images are obtained when tunneling is from a single metallic atom at the end of the tip. However, imaging artifacts of multi-tips [3] or blunt tips [4] are constantly reported in STM study. Moreover, the STM images invariably include the contributions of both the sample and the tip. Thus the preparation of sharp metal tips is essential to STM imaging and the characterization of the tips is also important for correct image interpretation.

Since its invention, STM has proved to be a very versatile instrument. It can operate in various environments, such as ultra high vaccum (UHV), air, liquid [5, 6] or cryogenic temperatures [7-9]. The construction and operation of an air-STM is much simpler compared to the UHV-STM, but the tunneling current is easily affected by contaminants from the ambient atmosphere. The main applications of the air-STM include the study of surface roughness, film growth mechanism and surface diffusion.

Inert surfaces, such as gold, are ideal for STM study in air. Au-based metallizations are most widely used in ohmic contacts to III-V semiconductors, although Au topographic study on these substrates is still very limited. In this work, the topographic study of Au thin films on InP substrates, and the influence of annealing, were carried out by STM with carefully prepared tips.

In the last decade, the applications of the STM have expanded rapidly, ranging from the characterization of surface roughness to atomic reconstructions. STM has been directly applied to metal surfaces to study the structure, phase transitions, adsorbate reaction, as well as the corrugation, to semiconductor surfaces to detect the most fascinating phenomena, i.e., surface reconstructions, and to superconductor surfaces to measure the local density of state. A number of new instruments have been derived from the STM for various new applications, as shown in Table 1-1 [10]. One example is Atomic Force Microscopy (AFM), which measures the force between the tip and the sample, in both contact and non-contact modes, with samples being both conducting and insulating [11, 12]. Another example is Ballistic Electron Emission Microscopy (BEEM), which permits imaging and provides electronic information at metal-semiconductor interfaces [13, 14].

BEEM employs an STM tip as an injector of ballistic electrons into the metal-semiconductor heterostructure. It operates as a multi-electrode system, with electrical contact to each layer of the sample surface. The metal base layer serves as a biasing electrode, and the n-type semiconductor functions as a collector of ballistic electron current. As a tip-base bias voltage is applied, electrons tunnel across the gap, propagate through the metal layer, and reach the interface. Some of the electrons may cross the interface and be measured as a current in the collector layer. By varying the voltage between the tip and the base, interface carrier transport and the metal-semiconductor Schottky barrier can be measured. Using the BEEM technique, ballistic hole spectroscopy and therefore the Schottky barriers of the metal-p-type semiconductor interfaces can also be measured.

According to current-voltage characteristics, metal-semiconductor contacts can be divided into two types: rectifying contacts with Schottky barriers higher than 0.3eV, and ohmic contacts with Schottky barriers lower than 0.3eV. Traditionally, the characterization of the interface and the measurement of the Schottky barrier rely on electrical probes, such as current-voltage or capacitance-voltage techniques. The disadvantage of all these techniques is that they are spatially averaging. BEEM techniques, on the other hand, allow these measurements to be made with nanometer spacial resolution.

Since its invention, BEEM has been applied to several metal-semiconductor interfaces, primary metals on Si and GaAs. There has not been a single literature citation, however, on its application to metal-InP interfaces. Metal-InP contacts are important in the formation of high quality and reliable ohmic contacts for optoelectronic devices. The initial goal of this project was to utilize the BEEM technique to measure the Schottky barrier height of a metal-InP interface, with the ultimate aim of developing a better understanding of ohmic contact mechanisms.

Motivated by this initial thought, a project of economically modifying an existing STM to BEEM was started. Although there have been a number of applications of BEEM, the experimental details of instrument modification from STM is still lacking.

This thesis is organized into nine chapters, separated into two parts: STM and BEEM. In the STM part, a comprehensive literature review is carried out in Chapter 2, which consists of the theory of STM, the instrument design, the fabrication and characterization of the STM tips and a review of Au thin film topography studies on various substrates. Chapter 3 describes the experimental procedures used for fabricating polycrystalline tungsten tips and gold thin films on Si(100) and InP(100) substrates, and the techniques used for characterizing the tips and the film topographies. The Discussion and Conclusions, with regard to instrument limitations, tip preparation procedures, tip effects on STM study, Au topography study on InP substrate, and tip deformation during imaging, are presented in Chapters 4 and 5. In the BEEM part, a comprehensive review

3

of the theory of BEEM and its application to various metal-semiconductor interfaces is provided in Chapter 6. Chapter 7 deals with the experimental methods of the instrument modification from STM to BEEM, including the design of circuitry and sample mounting stage, the installation of the data acquisition card and the software design, the fabrication procedures of metal thin films on semiconductors, and the characterization techniques used for the metal-semiconductor interfaces. Discussion of the calibration of the modified BEEM and its failure in application to metal-InP interfaces is provided in Chapter 8. Chapter 9 presents recommendations for further work on application of BEEM to metal/InP interfaces.

Table 1-1. The extension of STM and their applications [10].

(Table 1-1 continued)

that the material involved has been removed because of copyright restrictions

PART 1

SCANNING TUNNELING
MICROSCOPY

CHAPTER 2. LITERATURE REVIEW

The basic idea behind STM is quite simple, as illustrated in Fig. 2-1 [15]. A sharp metal tip is brought close enough to the sample surface that electrons can tunnel through the barrier separating the tip and the sample.

The position of the tip in three dimensions is accurately controlled by piezoelectric drivers. The coarse positioner brings the sample to within the tunneling distance of the tip. The tip is scanned in two lateral dimensions, while a feedback electronics constantly adjusts the tip height, to keep constant current, so the shape of the surface is reproduced by the path of the tip. This procedure yields an image of surface topography.

2.1   The Fundamental Principles of STM

The underlying physics of the STM is electron tunneling. When two metal surfaces are separated by a sufficiently thin insulating layer, the work functions of the two metals combine to make a potential barrier. Classically, electrons can move freely at either side of the barrier (within one metal), but cannot cross the barrier region. Quantum mechanically, electrons are described by wavefunctions, which have both particle and wave nature, and can extend into the barrier with an exponentially decaying tail. Upon impinging on the barrier, electrons will be reflected if the barrier is too thick (Fig. 2-2a). On the other hand, if the barrier is thin enough, electrons may penetrate the barrier and appear on the other side (Fig. 2-2b) [16]. This process is called tunneling. The tunneling probability can be calculated by solving the Schrödinger equation for a system consisting of the two metals and a barrier. By simplifying the system to a one-dimension, free electron metal and a rectangular barrier height, the Schrödinger equation can be solved [17]:

8

$$\psi(x) = Ae^{-ikx} + Be^{+ikx}, \qquad k = \sqrt{\frac{2mE}{\hbar^2}} \qquad \text{(metal 1)} \qquad (2\text{-}1)$$

$$\psi(x) = Ce^{-ikx} + De^{+ikx} \qquad \text{(metal 2)} \qquad (2\text{-}2)$$

$$\psi(x) = Ge^{-\mu x} + He^{+\mu x}, \qquad \mu = \sqrt{\frac{2m(U-E)}{\hbar^2}} \qquad \text{(barrier)} \qquad (2\text{-}3)$$

where U is the barrier height, E is the energy of the electron, m is the mass of the electron, and $\hbar$ is Plank's constant divided by 2π, and $\psi(x)$ is the wave representation of an electron. Considering that the electron wavefunction and its first derivative must be continuous (join smoothly) at the sample-barrier and tip-barrier boundaries to conserve energy, the tunneling probability can thus be derived as [18, 19]:

$$T(E) \propto e^{-\mu s} \qquad (2\text{-}4)$$

where s is the barrier width (tip-sample separation), and μ is $\sqrt{\frac{2m(U-E)}{\hbar^2}}$. The tunneling current, which is proportional to the tunneling probability, decays exponentially with barrier width s. In the simplest case, U is assumed to be the vacuum level, so (U - E) is just the work function of the metal. Since typical work functions of the metals are around 4-5 eV, the tunneling current drops by nearly an order of magnitude for every 0.1nm of separation. It is this sensitivity of the tunneling current to the distance between the tip and sample that provides the atomic resolution capability of the microscope.

2.2 Instrumentation

While the basic principle of the STM looks simple, the design and structure of STM are complex because the tip has to be brought into the tunneling range (about 0.6nm separation) and scanned in a raster pattern without crashing into the sample. Low frequency vibrations, small thermal drifts and electrical noise are the main obstacles to the accurate placement of the tip.

2.2.1 Vibration Isolation

Vibration isolation is designed to suppress the change in the distance between the tip and the sample due to the external mechanical vibration, because the mechanical stability of an STM has to be better than the desired resolution. While the internal vibration can be reduced by a mechanical and electrical low-pass filter in the tip control loop, external vibrations have to be reduced by a proper isolation system.

An important source of vibration that reaches the sample-tip junction originates from the building, through the table on which the microscope sits. Typical building vibrations are in the range of 0.1-50 Hz. The maximum resonances occur at frequencies between 10-25 Hz. The table can have additional resonances in the range of 30-100 Hz [20].

In order to understand the mechanism of vibration isolation, the mechanical system of an STM can be divided into two parts: the tunneling unit and the vibration isolation stage (Fig. 2-3) [21]. Both of these have their own mechanical eigenfrequencies. According to Okano et al. [21], the transfer function of the isolation stage to the external vibration is defined as:

$$Z_1 = 20 \log(x_i/x_b) \tag{2-5}$$

The transfer function of the tunneling unit to the isolation stage is defined as:

$$Z_2 = 20 \log[(x_t - x_i)/x_i] \tag{2-6}$$

where x_i and x_t are the displacements of the isolation stage and the tunneling unit, respectively, and x_b is the amplitude of the displacement of the floor.

The overall transfer function of the tunneling unit to the external vibration is

$$Z = 20 \log[(x_t - x_i)/x_b] \tag{2-7}$$

By considering the damping factor and defining $T_1 = 10^{Z_1/20}$, $T_2 = 10^{Z_2/20}$, then the transfer functions of both systems are [22]

$$T_1 = \frac{\omega_i^2 + 2i\gamma_i\omega}{\omega_i^2 - \omega^2 + 2i\gamma_i\omega} \tag{2-8}$$

10

$$T_2 = \frac{\omega}{\omega_t^2 - \omega^2 + 2i\gamma_t\omega} \qquad (2\text{-}9)$$

where γ_i , γ_t are the damping factors of the isolation and tunneling unit, respectively, and ω_i, ω_t are the eigenfrequencies of the isolation and tunneling unit, and defined as

$$\omega_i = \sqrt{\frac{k_1}{m_1}} \qquad (2\text{-}10)$$

$$\omega_t = \sqrt{\frac{k_2}{m_2}} \qquad (2\text{-}11)$$

where k_1, k_2, m_1, m_2 are the spring constants and the effective mass of the isolation stage and the tunneling unit, respectively.

T_2 is plotted in Fig. 2-4 for $\gamma_t = 0.025\omega_t$ [22]. In the lower frequency range ($\omega \ll \omega_t$), T_2 becomes ω^2 / ω_t^2. Therefore, as the external vibration frequency ω decreases by a factor of 10, the tunneling unit response becomes smaller by a factor of 100. T_1 is plotted in Fig. 2-5 for several values of γ_i. For small damping ($\gamma_i \ll \omega_i$), high frequency vibration is more efficiently suppressed, with large oscillation at resonant frequency. On the other hand, heavy damping ($\gamma_i = \omega_i$) will reduce the resonance oscillation, with less attenuation at high frequency vibration. Therefore, the damping factor should be adjusted such that both the vibrational noise and resonance peaks are minimized.

Fig. 2-6 shows the overall response of the tunneling gap to external vibration for the case of $\omega_t/\omega_i = 1000$ [22]. The best vibration isolation is at intermediate frequency, and its efficiency depends on the ratio of ω_i and ω_t. Therefore, the design principle of the mechanical system of an STM is to make resonant frequency ω_i for the vibration isolation stage as low as possible, and resonant frequency ω_t for the tunneling unit as high as possible. However, the resonant frequency is determined by the physical dimensions of the microscope. Rigid and compact STMs are more immune to vibration.

Three types of isolation systems which have been used so far are: magnetic levitation of permanent magnets on a superconducting lead bowl [1], coil spring suspension [21, 23- 25], and multiply stacked metal plates, separated by pieces of viton

11

which act as springs and dampers [26, 27]. The last two stages are schematically shown in Fig. 2-7 [20].

Magnetic levitation has not been widely used because of its complexity and undesirable effects, especially thermal drift.

For a spring suspension stage, the springs act as a low-pass filter: up to the cutoff frequency (resonance frequency), the STM allows the movement of the suspension of coils. At frequencies much higher than the cutoff frequency, the response decreases logarithmically. Clearly, it is advantageous to choose the cutoff frequency as low as possible.

For better isolation, two stages of the spring suspension are commonly used. According to Park et al. [23], it is desirable to make the springs of the two stages overlap each other rather than simply attaching the inner stage spring to the bottom of the outer stage spring. This overlap results in longer springs and therefore lowers the cutoff frequencies.

As a damping mechanism (eddy current damping), permanent magnets and copper blocks are usually used [23]. Okano et al. [21] concluded that the best performance is obtained if only the second spring stage is damped. The damping factor can be adjusted easily by varying the strength of the magnets, the size of the copper blocks, and the spacing between them [22].

For a stacked metal plate isolation system, the stiffness of the rubber is higher than that of the coil springs. Since the compression of the vitron is limited, the performance is poorer than spring suspension stages. Increasing the number of stacked plates will reduce the cutoff frequency and improve the vibration isolation. However, it is impractical to achieve a resonant frequency below 10Hz. Practically, the performance of the metal plate can be improved by suspending it with springs, or supporting it with a rubber tube, or replacing the viton with small springs [22, 26]. All these methods are aimed at achieving higher compression or expansion lengths, thus lowering the cutoff frequency.

Details of the performance of both the spring suspension stage and stacked metal plates are given by Okano et al. [21].

2.2.2 Coarse Positioner

The aim of a coarse positioner is to bring the sample and the tip to within the tunneling distance and to keep them there as rigidly as possible to minimize the influence of vibrations. In order to avoid contact between the tip and the sample, the motion of the coarse positioner must be smooth down to 5nm, while exhibiting a wide range. To simplify the sample approaching procedure, a control electronics and computer can be used to step either the sample or the tip a small distance. After each step the tip is extended to see if any tunneling current can be detected. In this way, the sample or the tip is automatically brought to within tunneling distance.

The devices that have been used can be divided into three categories: screw [28], clamp-step [24, 29], and stick-slip [30]. Screws can be used with lever or spring reduction mechanisms [5, 6, 31-34]. The screws can be turned by either a stepper motor mounted on the microscope, or with an external motor. Using a lever reduction mechanism, the mechanical displacement that occurs at the screw can be reduced by the ratio of the distance l_2 from the screw to the fulcrum and the distance l_1 from the tip to the fulcrum (Fig.2-8 [20]). The design goal is then to put the fulcrum as near to the tip as possible, thus increasing the ratio of the distances.

Clamp-step devices consist of a piezoelectric plate sitting on feet. The device "walks" like an inchworm if two clamped feet are used [35]: clamping one foot to the base, expanding the body, clamping the other foot to the base while releasing the first foot, and then contracting the body (Fig. 2-9 [20]). The motion of an inchworm is in one dimension. If three feet are used, the motion can be in two dimensions, and the device is called a "louse" [24, 29]. The major disadvantage of these types of devices is their sensitivity to dust and other effects which influence the sticking of their feet to the supporting base.

Stick-slip stages are sample positioners in which the sample holder is rested on piezoelectric tubes [34]. A sawtooth signal is applied to one of the tubes so that the sample moves horizontally.

2.2.3 The Scan Unit

The scanner is the device that moves the tunneling tip across the sample surface and controls the tip-sample separation. The requirements of a good scanner are [24]: 1) high resolution; 2) orthogonality - movement of the three axes should be independent; 3) linearity - the amount of the movement should be proportional to the applied voltage; 4) mechanical rigidity - a rigid scanner will have a high resonant frequency, which is desirable for high scan speed, vibration isolation and feedback performance; and 5) large range.

The piezoelectric ceramic PZT [Pb(Zr, Ti)O$_3$] meets most of the requirements. In general, PZT ceramics consist of two different charged crystalline grains, one is positively charged and the other is negatively charged, which will expand in one direction and contract in the other in response to external electric fields and cause the dimensions of the PZT to change. Common problems with piezoelectric actuators include non-linearity, hysteresis, and creep. The desired sensitivity for the piezoelectric elements should be determined by considering both the scan range and the resolution. Higher sensitivity is not always desirable because of the noise level of the driving signal, and it may cause more uncertainty in the tip position. To increase the scan range, it is better to increase the piezoelectric constant rather than the size of the scanner. The latter will reduce the resonance frequency, which will further affect the mechanical vibration and electronic noise.

Four typical STM scanners are shown in Fig. 2-10: (a) bar tripod [2, 24], (b) tube tripod [22], (c) single tube [36], and (d) stacked disks [22]. Bar tripod and single tube scanners are the most commonly used. The bar tripod scanner was the original scan unit used by Binnig and Rohrer [24]. By applying a voltage across each of the bars, the tripod

scanner moves the tip in the X, Y or Z direction. It has reasonably high resonant frequency, ranging from 3KHz [29] to 20 KHz [37], relatively low sensitivity (nm/V), and good orthogonality [23, 32, 38]. The single tube scanner has become popular due to its compact and simple structure, resulting in high sensitivity and high resonant frequency. Resonance frequencies of 10KHz parallel to the surface and 100KHz perpendicular to the surface are easily obtained. Various sensitivities and scan ranges are reported by several groups [23, 36, 39 - 41]. The outside electrode of the single tube scanner consists of four sections of equal area. By applying a symmetric voltage across two diagonally opposite electrodes, the tube is bent perpendicular to its axis, producing lateral motion [22]. The amount of the lateral displacement is proportional to: $(l^2/Dt)V_p$, where l is the length, D is the tube diameter, t is the wall thickness, and V_p is the applied voltage. The vertical Z voltage is applied to the inner electrode relative to the outside electrode to adjust the height [22], and its displacement is represented by : $d_{31} V_p l/t$, where l is the length of the tube, t is the thickness, V_p is the voltage, and d_{31} is the piezoelectric constant. For a typical PZT, the value of d_{31} is $(- 1$ to $- 2) \times 10^{-10}$ m/V [22]. The maximum displacement is limited by the piezo material. A more detailed analysis of the single tube has been carried out by Carr [42].

2.2.4   Control Electronics

The feedback electronics is used to control the tip-sample separation in order to maintain a stable tunneling junction.   Fig. 2-11 is a typical block diagram for the z-motion of an STM [22]. A current-to-voltage preamplifier is used to detect the tunneling current and convert it to a voltage to be used by the feedback electronics. Because the tunneling current varies exponentially with the separation, a logarithmic amplifier is used to linearize the current from the preamplifier. This value is subtracted from the reference current to obtain the error signal. The goal of the feedback system is to minimize the error signal. If a simple proportional feedback is used, the error signal can be reduced by increasing the proportional gain. On the other hand, sufficiently high gain could cause

15

system oscillation. By adding an integrator, the error signal can be eliminated. This integrator causes a small error signal to be integrated in time, producing more and more control action until the error is eliminated. A typical STM application uses both proportional and integral control functions, with adjustable gain of the proportional stage from 0.01 to 100, and integral gain from 0.1 to 10^4 s^{-1}. Signals from the proportional stage and integral stage are summed to generate the feedback output, which goes to a high-voltage amplifier to drive the piezoelectric actuator.

Fig. 2-12 [22] is the circuitry for the lateral scan control, allowing adjustment of the location of the sample to be scanned. The necessary adjustments are x, y scan size, and x, y position offset. Generally a raster scan with one fast scan signal (horizontal) and one slow scan signal (vertical) is generated. These signals can be either triangle waves or sine waves. Finally these x and y signals, like the z signal from the feedback electronics, are amplified to the high-voltage levels required for the piezoelectric elements.

2.2.5 Burleigh STM

A Burleigh Instructional STM was used in this study and is comprised of three subsystems: the tunneling assembly (head), the control system (control electronics), and the display device (computer).

The head houses the sample and the tip. The tip is attached to a single tubular PZT, which has a range of about 1.2 microns in Z and 3 microns in X and Y. The coarse positioner is a stepper motor mounted in the microscope, in combination with a motion-reduction lever mechanism (Fig. 2-13 [16]). The motion-reduction mechanism allows a finer motion than the step size of the motor. The tip is stepped toward the sample automatically. The control electronics drives the motor and terminates the motion of the tip when a reference tunneling current is detected. The vibration-isolation mechanism used in the STM head consists of a stack of four metal plates with special rubber damping material between them. To achieve the best results, the head is placed on a vibration isolation table, which consists of a stack of two granite plates separated by rubber, sitting

on a heavy steel plate on top of a small, partially inflated inner tube. The head also contains an amplifier circuit which converts the tunneling current to a voltage to be used by the feedback electronics.

The control electronics uses negative feedback to keep the sample and tip within the tunneling distance as the tip is scanned over the sample. The feedback electronics consists of three parts:

(1) Time Constant (Integral): This control is used to adjust the time constant of the contour tracing capability. If the time constant is set to minimum, the feedback will respond to any variations in the surface very quickly.

(2) Gain (Proportional): As the gain is increased, the tip will make large motions to correct for changes in tunneling current. The feedback system may oscillate if the gain is increased too high.

(3) Filter: It is a low-pass filter. All the freguencies higher than the set value will be rolled off. Usually it is set close to the maximum (with minimum filtering).

2.3　Operating Modes

There exist two operating modes for STM (Fig. 2-14 [43]): constant current mode [44, 45] and constant height mode [46].

2.3.1　Constant Current Mode

In this mode, the tip should follow the sample surface as closely as possible. As the tip is scanned in the two lateral dimensions controlled by x-y piezoelectric driver, a voltage is applied to the z piezoelectric driver to adjust the tip height to maintain constant tunneling current. The contour of the surface is thus reproduced by the path of the tip, and the height z is plotted versus the scan position (x, y). This mode can be used to trace surfaces which are not atomically flat. However, the scan speed should be reduced to allow the feedback to reach equilibrium at each new location of the tip.

17

2.3.2   Constant Height Mode

In constant height mode, a tip is scanned across a sample at an average height and constant voltage, while the current is monitored. Surface features on the sample are reflected in the fluctuation of the tunneling current. The surface information is derived from the tunneling current, which is plotted versus the scan position (x, y).

This mode is usually used in the situation where scan speed is required and the sample surface is extremely flat. It also requires a good orthogonality scanner. A high speed can be obtained because only the electronics, not the height of the tip, must respond to the atoms passing under the tip. However, in the case where the surface corrugations are larger than the tip sample separation (0.5 - 1nm), the tip will crash into sample.

2.4   Tip

The tunneling tip is the most crucial component of the STM. Both the geometry (shape and sharpness) and the electronic states of the tip influence the image quality. The best images are obtained when the tunneling is limited to a single metallic atom at the end of the tip, and the parameters of the tip geometry become much more important when imaging significant topography.

2.4.1   Tip Fabrication

There has been considerable interest in making sharp metal tips for high resolution imaging, ever since the STM was invented. The various tip preparation procedures can be divided into two main categories [47]: (i) mechanical or (ii) physicochemical. Mechanical procedures include cutting [48], machining [2], and fragmentation [49] of metal wires to form sharp tips. The first tunneling tip produced by Binnig et al. [1, 2] was mechanically ground from 1mm diameter W wire. Atomic

18

resolution can be achieved with these tips because when a tip is formed, it is likely that a single atom will be protruding from the end of the tip. However, limited stability and abrupt changes in resolution were also constantly reported [50]. Tips usually suffer poor reproducibility, lack of tip symmetry, large cone angle and multiple tip formation. For samples with rough surfaces, such tips will produce non-representative images of the surface, creating the need for tips with well-defined geometry.

Physicochemical processes can be used to produce tips with well-defined shapes by controlling the processing parameters. Techniques include electrochemical etching/polishing [51], ion milling [52, 53], vapor deposition [54] and electron beam deposition (EBD) [55, 56]. Historically, electrochemical etching/polishing was the earliest technique for sharpening metal tips to very small radii for field ion microscopy (FIM) purposes [57], and continues to be extensively used for making STM tips. Because of the sensitivity to vibration, STM tips should be rather thick and come to a point rapidly. So the production parameters for FIM tips and STM tips are quite different. A variety of methods, such as dc, ac or pulsed voltage etching/polishing, as well as/or combinations of these, by downward or upward (reverse) immersion of the metal wire into an appropriate electrolyte [28, 34, 47, 51, 58-77] have been reported. The electrochemical etching/polishing procedure usually involves the anode dissolution of the metal electrode. Each procedure gives different tip shapes. For normal downward immersion, dc etching/polishing usually gives a hyperboloid shape and sharper tips, while ac etching/polishing results in conical shapes with large cone angles.

The dc electrochemical etched/polished tips are generally prepared by a drop-off method (Fig. 2-15a [60]). The surface tension of the aqueous solution causes a meniscus to form around the wire solution interface once the wire is dipped into the electrolyte. After applying a positive voltage to the wire, the etching/polishing process, which involves the oxidative dissolution of metal wire to metal anions at the anode and the reduction of water to form bubbles of hydrogen gas and OH^- ions at the cathode, occurs at the electrolyte/air interface. A sheath of descending metal anions around the lower part of the wire shields it from further OH^- attack. So the etching/polishing rate at the lower

19

portion of the wire is less than that at the meniscus portion, resulting in a neck-in effect (Fig. 2-15b [60]). When the the weight of the lower part of the wire exceeds the tensile strength of the neck, the "drop off" event occurs.

The dc drop-off method will produce two tips simultaneously: the part above the air/electrolyte interface and the part below the interface. Bryant et al. [59] have stated that the lower tip had more desired asperities since the etching/polishing stops as soon as the tip drops off.

The etching mechanism for the ac method involves bubble dynamics [47]. The bubbles at the anode formed during one half cycle by the ac voltage will push upward in a strong and directional stream due to their buoyancy forces. The directional bubble stream affects substantially the local etching rate at the tip surface depending on its attachment to the tip surface.

In the normal downward orientation (Fig. 2-16a [47]), the bubbles, pushed by buoyancy directly upward and toward the wire (Fig. 2-17a [47]), can only move along the metal surface in a divergent stream at a flow rate that depends on the etching voltage. The attachment of the bubbles acts as a mask to the side surface of the tip, resulting in a slow, nonuniform etching rate. On the other hand, the etching at the very end of the tip is not hindered since bubbles are pushed away by buoyancy.

In reverse etching (Fig.2-16b [47]), the bubble flow along a tip is determined by the shape of the surface. The bubbles slide upward along the tip surface while attached to it by the surface tension. The normal component F_N of the buoyant force F_B detaches the bubbles from the surface when it overcomes the surface tension. Because of the uneven masking effect along the tip surface by the bubble flow, the etching rate increases with the distance from the very end of tip, which is the reverse of the downward method, resulting in a progressively sharpened tip. However, the overall tip shape produced by reverse etching depends on the initial tip shape, so reverse etching is usually used as a second step in tip fabrication. Ultra sharp mini tips with radii of 1nm have been reported [47, 58].

Attempts at controlling relevant polishing parameters to improve tip reproducibility have been made. These include cutoff time, immersion depth, voltage, wave shape, phase angle and frequency [60, 70]. The response time to turn off voltage is the most important parameter in making sharp tips. Many innovations have been aimed at minimizing the cutoff time. These include automated processes [60, 70, 71, 78], with 100nm radii tips being produced in some instances [71], optical microscopes [51] to monitor the process, as well as electrolyte dilution after neck-in has begun [51].

Additional sharpening can be accomplished by localized polishing which is designed to minimize the region of wire in contact with the electrolyte. Examples include the floating layer technique [64, 79] and the loop technique [80]. Other techniques, such as zone electropolishing [81], were designed to control the near-apex region aspect ratio or to make a desired tip geometry after the initial tip had already been made.

It is well known that W tips prepared by electropolishing are usually covered by a very thin layer of oxide (WO_3). The presence of surface oxide adversely affects STM image quality, as well as tunneling stability. Attempts to remove the oxide layer have been made. Biegelsen et al. [52, 53] and Garnaes [82] have used ion milling with argon ions directed at the W tip surface. No detectable oxide grows after tips have been subsequently exposed to air for one day. In the case of cold drawn polycrystalline tungsten tips, sharp and oxide free tips can be fabricated with short sputtering time, while longer sputtering results in very rough tips because of different sputtering rates at the grain boundaries. In the case of the single crystal tungsten tips, a very sharp faceted tip with radius of 3nm can be produced. Other processes, like annealing with electron bombardment at 1800K [83] or simply applying a wet chemical treatment to dissolve the oxide [84], have been reported. An electronic phase control unit has also been designed to control the second stage of electropolishing to make oxide free tips [72].

EBD tips, usually made for AFM imaging, have also been reported by several groups [55, 56] to be successfully used for STM. The tunneling mechanism for EBD tips is unknown as EBD tips are mainly composed of amorphous carbon, hydrogen, and oxygen [55]. Imaging with EBD tips on metal line gratings shows more pronounced and

accurate deep grooves compared to the cut Pt-Ir tips, because of their remarkably small diameter and straight shank.

The deposition of EBD tips is done in the scanning electron microscope (SEM) by exposing a single spot on the preformed tip to the electron beam for a period of time. The most common way is to focus the beam onto the top surface of the tip and maintain the beam position. Electron beam deposition takes place at the beam spot and results in a needle-like tip (Fig. 2-18 [55]). The size of the EBD tip depends both on the focusing condition and the irradiation time.

EBD tips can also be fabricated by bringing the electron beam in at 90° to the direction of the tip growth. When the beam hits the end of the tip, a small dot is deposited. The beam is then repositioned at the end of the new dot, and so on. The growth rate is four or five times faster than for growth along the direction of beam.

The mechanism of the growth of EBD tips does not seem to be known in detail, but is assumed to involve the decomposition of the "contaminant" organic gas molecules by primary and secondary electrons of the incident beam [86].

Details of the above techniques can be found in the cited references and a number of review papers [47, 51, 87].

2.4.2 Tip Characterization

As has already been mentioned, both tip shape and sharpness are of central importance for interpretation of STM images. Most tips are examined by SEM at modest magnifications [48, 51, 60, 61, 63-66, 71, 73, 74, 77, 83, 84, 88-92]. Recently, however, ultrasharp tip geometries have been characterized by high resolution transmission electron microscopy (TEM) at high magnifications. Examples of tips that have been examined include polished and ion milled W tips with radii of 10 to 200 nm [82] and 3 nm [53], upward etched W tips with 1nm minitips [47, 58], two-stage tips prepared with an electronic phase control unit to radii of 20 nm [72], EBD tips with radii of 20 nm [55] and Au-coated W tips with 20nm gold clusters [93].

22

Direct STM characterization has also been used, usually using atomic resolution of highly oriented pyrolytic graphite (HOPG) [63, 89-91, 94, 95] to determine the tip quality.

Theoretical morphological estimation of the tip geometry has also been given by several groups [96, 97]. Calculations are based on the fact that broad tips cannot produce sharp image protrusions; thus feature sizes within the image can be used as an upper bound of the tip size [96]. Efremov et al. [97] have developed a mathematical method to determine the profile of two unknown tips by their mutual scanning when the two tips are oriented differently.

2.4.3. Tip Performance

The chemical identity and morphology of the tip determine the stability and resolution of the STM image. STM imaging on atomically flat surfaces often relies on the presence of mini-tips on a macroscopic tip, and the obtained images can in many cases be interpreted as tunneling through a single atom on the tip. However, the resolution of STM on rough surfaces is clearly limited by the corresponding shape of the tip. In such cases, the shape and arrangement of the minitips are important factors that can affect the stability of the image and the true surface structure.

Theoretical calculations aimed at determining the true surface structure from images distorted by finite-size tips have been done by several groups [98-102]. Keller [101] has reported that the local curvature of the sample surface is the sum of the tip curvature and the distorted STM image surface curvature (Fig. 2-19 [101]). In some extreme cases, the distorted image cannot be completed reconstructed (Fig.2-20 [101]). Most of these numerical reconstruction calculations are done under the assumption of a parabolic or spherical shaped tip with an estimated tip radius. An attempt has also been made to reconstruct the surface topography from an STM image based on the knowledge of the tip shape obtained from SEM [99].

23

A second aspect of the tip quality is the chemical purity and homogeneity, strictly speaking, the tip electronic states. The importance of the tip electronic states in the imaging process was first realized by Baratoff [103], who conjectured that a single dangling-bond state protruding from the apex of the tip is probably the origin of atomic resolution. Numerous experimental and theoretical studies indicate that the STM imaging process, especially the resolution, does depend dramatically on the tip electronic structure. Wintterlin et al. [104] found that atomic resolution on close-packed metal surfaces can be easily obtained after an electrical treatment on electrochemically etched W tips. They proposed that a metal cluster is formed on the blunt tip by this tip preparation procedure, and an elastic deformation of this cluster, caused by the adhesion forces between the tip and the metal sample, is responsible for the resolution of the individual atoms. Behm [105] summarized that with such a tip-treatment procedure, atomic resolution was obtained on many other metal surfaces. Thus, they concluded that atomic resolution is not specific for certain surfaces, but rather depends on specific tip states. Although the tip electronic states are crucial in the understanding of STM images, experimental determination of the tip electronic states has been very difficult because the tip states changes frequently and spontaneously during the imaging process.

2.4.4   Tip deformation

Tip deformation during scan has also been investigated by comparing TEM images of tips before and after STM imaging. According to Garnaes [82], an electropolished W tip, which is usually covered with several nm of oxide, severe tip bending or sometimes flattening of the tip is observed after scanning on platinum samples. They concluded that this deformation is due to the oxide on the top of the tip causing tip-sample contact during tunneling. This is schematically shown in Fig. 2-21 [87]. When the tip tunnels through an insulating layer, the tunneling barrier height is decreased and the sensitivity of the tunneling current to the tunneling gap is reduced, thus causing contact between the tip and the sample.

24

2.5   Au Thin Film Topography

The study of the nucleation, growth and orientation of thin metal films began shortly after the interpretation of electron diffraction patterns presented by Linnik [106]. Renewed interest in the deposition of smooth, well-oriented metal films has developed recently, to a large extent related to the development of the STM. One of the applications of an air-STM is surface topographic study, especially the surface roughness. Because of their stable inert surface and lack of oxides, Au surfaces are ideal systems for STM studies in air. A number of papers describing the topography of gold films on various substrates, investigated by STM, have been published in recent years.

The structure of thin evaporated metal films, such as the surface flatness and lateral size of the crystallites depends on a number of parameters, including the substrate material, substrate temperature during deposition, deposition rate, film thickness, annealing time and temperature after deposition, and the method of deposition. The grain size and surface roughness of metallic films are the two important parameters used to describe the morphology of the film during layer growth and to compare the influence of different parameters on the film deposition quality. The surface roughness is usually calculated from mathematical equations [107], shown below:

Average roughness:

$$R_{ac} = (1/N) \sum_{i=1}^{N} |Z_i - Z_m| \qquad (2\text{-}12)$$

Root-mean-square (rms) roughness:

$$R_{qc} = [(1/N) \sum_{i=1}^{N} (Z_i - Z_m)^2]^{1/2} \qquad (2\text{-}13)$$

$$\text{where } Z_m = (1/N) \sum_{i=1}^{N} Z_i \qquad (2\text{-}14)$$

Peak-to-peak roughness:

$$R_t = Z_{max} - Z_{min} \qquad (2\text{-}15)$$

Usually these roughness parameters can be obtained by drawing several line profiles from every image. From each profile the following measurements are made:

(1) The height absolute value Z_i of each grain and the highest and lowest values (Z_{max}, Z_{min}) are obtained from the surface profile manually, as well as the grain diameter, which are schematically illustrated in Fig. 2-22 [108].

(2) The average height (Z_m) is then calculated from equation (2-14).

(3) The average roughness, rms roughness and peak-to-peak roughness can be calculated according to the above equations.

For gold thin films, Au on mica, glass and silicon substrates have been substantially studied. According to Vancea et al. [109], the topographies of gold thin films can be classified into three types :

(1) Rough surface: the surface of the thin film is much rougher than the substrate, showing a hilly landscape.

(2) Smooth surface: the surface of the thin film is much smoother than the substrate, showing features of the underlying substrate together with much smaller features of film topography.

(3) Mixed surface: the film surface shows both smooth and rough regions due to the difference in local growth of the film on the substrate.

Both Vancea et al. and DeRose et al. [110] concluded that Au films on mica show the smoothest surfaces for substrates of mica, glass and Si.

2.5.1 Au/Mica

The topography of Au films on mica belongs to the mixed surface category. Atomically smooth plateaus of 60 to 100nm in the lateral direction are observed, along with typical polycrystalline surfaces of hillocks in the height range of a few nanometers. Such a varying topographic character has also been previously reported by Marchon et al.

26

[111] on samples annealed at 250°C. This structure is believed to be due to the imperfection in cleavage of mica and different incipient growth mechanisms.

(1)   Substrate Temperature

Among the influences, the substrate temperature during the deposition is the most important factor affecting gold film morphology. Several groups have studied substrate temperature effects in the Au/mica system [112-114]. Despite differences in other deposition parameters, the surface topography changes from grainy hills and valleys to atomically flat plateaus with steps, and occasionally holes and grooves as the substrate temperature increases, while the peak-to-peak roughness decreases. With further increase in temperature to high values, Au films can be very rough on a large scale because of degradation of the mica substrate. According to Putnam et al. [112], the morphology of Au thin films on mica can be divided into four regions: (1) At mica temperatures below 200°C, the surfaces consist of hills and valleys, with no atomically flat regions. (2) At substrate temperatures ranging from 200°C to 400°C, surface topography changes to atomically flat tops, while valleys and depressions between crystallites still exist. Monatomic steps can sometimes be seen on top of the plateau regions. (3) At substrate temperatures from 400°C to 600°C, the surface is flat in large areas, with atomic steps and occasional holes (grooves). Individual crystallites separated by valleys no longer exist. This is the temperature range to obtain the smoothest surface. (4) The fourth region is at substrate temperatures higher than 600°C. Degradation of the mica results in rougher films with deep holes and trenches.

The actual temperature ranges for the above processes are affected by the quality of the mica substrates [113]. Details of mica temperature relationship with the film structure, lateral size and peak-to-peak roughness are given by Putnam et al. [112] for a 100nm gold film and Chidsey et al. [113] for 120nm gold films.

These topographic observations can be explained by the nucleation of crystallites and film growth. At low substrate temperature, the mobility of gold atoms on the substrate is low, thus the growth of nuclei is faster than the fusion of nuclei before the

27

film coalesces, resulting in hillock structures. At higher temperature, the mobility of the gold atoms on the hot substrate increases, thus the rate of nuclei fusion is much faster than at low temperature, resulting in flat surfaces.

(2)   Film Thickness

Film thickness effects were also studied by Chidsey et al. [113] and associated with the substrate temperature. At a mica temperature of 45°C, as the film thickness increases, the surface topography remains grainy, but the spacing of the hills increases from 15nm for 50nm thick gold film to 120nm for 480nm thick gold film, while the peak-to-peak roughness decreases from 7.5nm to 2.5nm. That the topography of grains is nearly unchanged is due to the low mobility of gold at low temperatures. At a mica temperature of 225°C, the surface topography of 50nm Au films is flat-topped grains with prominent holes (grooves). Dislocations and depressions were also observed. For 480nm of Au, similar flat plateaus with depressions were observed, with absolutely no holes (grooves). This is because thicker films had more material to fill in the topography, showing less pronounced holes than thinner films.

(3)   Annealing process

Generally, low temperature annealing changes the hillock structure of an as deposited film (room temperature substrate) to a very flat topography with occasional bumps as mentioned previously [111].

(4)   Deposition Rate

Deposition rates of 1-20 nm/s for mica temperatures of 425°C and 10nm gold film are also reported by Putnam et al. [112]. Higher rates give larger plateau sizes and more atomic steps.

Surfaces of gold on mica showing flat terraces of 20 to 100nm widely separated by sharp steps that can be monoatomic, diatomic, or triatomic are also reported by Moritz

28

et al. [115]. Step motion, which was believed to be due to contamination during the film preparation process, was also observed in their study.

Another phenomenon, i.e. atomic corrugation, was first observed by Hallmark et al. [116] on a close-packed Au (111) thin film surface, which normally exhibits large terraces separated by broad steps of monatomic height.

2.5.2   Au/Glass

The topography of Au/glass belongs to the rough surface category; it has a mountain-like landscape, with hills of various heights and lateral extensions statistically distributed on the surface. For a 80nm gold film, a typical surface roughness of 11nm and grain sizes between 20 and 40nm are observed [109]. With a thin chromium film on the glass prior to the Au deposition, the hill landscape of the Au film is dramatically flattened due to chromiun nucleation centers, and the surface roughness is reduced to 2 to 3nm. It is believed that the island size prior to the coalescence of a film is the main reason for the roughness of the polycrystalline metal film [109].

The effects of the substrate temperature during deposition, film thickness and annealing after deposition have been thoroughly studied for Au/glass system.

(1)   Substrate Temperature

The effect of the substrate temperature on the surface topography of Au/glass is similar to the Au/mica system [117]. At room temperature, the grains show a hillock structure with an average size of 30nm. At a substrate temperature of 105°C, some of the grains have already developed flat tops with terraces separated by multiatomic steps, with most of the grains maintaining a hillock structure. The average grain size is also increased to 100nm. At substrate temperatures ranging from 185°C to 300°C, films clearly develop top facets, and the largest step-free terrace was obtained at a temperature of 300°C. At substrate temperatures higher than 400°C, rounded bumps frequently occur on the tops of the flat grains. The size of the bumps increases with temperature, and

29

eventually these protrusions, which are caused by the creep of the glass at high temperature, destroy the terraces.

(2) Film Thickness

As in the Au/mica system, film thickness effects were studied in association with the substrate temperature [117]. The average grain size and roughness are nearly independent of the film thickness at substrate temperatures below 105°C, while the grain size increases with the film thickness at substrate temperatures above 185°C. Thinner films (20nm) become discontinuous and break up into isolated islands.

(3) Annealing Process

Lin and Chung [108, 118] have measured the activation energy for surface diffusion of gold on glass substrates by studying the decay rate of the surface roughness amplitude as a function of annealing temperature, ranging from 125°C to 170°C. The roughness was found to decrease monotonically with time with a rate increasing with temperature, consistent with the process of surface diffusion. Thus surface diffusion is believed to be the dominant mechanism of morphology change in this temperature range.

The change in the surface morphology as a function of annealing temperature and time for the Au/glass system is very similar to the Au/mica system with the films on mica frequently showing a wider grain size distribution [119]. The grains typically have a hillock structure, and remain unchanged upon annealing at 400°C. During 500°C annealing, the contours of the grains change from rounded to straight lines, typically 100nm long, with angles of 60°, 90° and 120° between each other, suggesting the development of the well defined crystallographic facets. The grain size increases monotonically with the annealing temperature, 30nm for as deposited films and 200-400nm for 400 to 500°C annealing. Roughness, on the other hand, shows a more complicated dependence on the annealing temperature. It decreases for annealing temperatures up to 300°C, but increases considerably at an annealing temperature of 500°C. Porath et al. [119] concluded that surface diffusion is the dominant mechanism

30

for low temperature annealing (300°C and below), while other mechanisms, such as evaporation-condensation and bulk diffusion, are dominant in the high temperature range.

2.5.3   Au/Si

Gold layers on silicon single crystals are reported to be rougher than on glass because of the diffusion of Au into Si. A hill-like landscape was observed, with an average height variation of 16nm [109]. The lateral extension of the hillocks is increased from 40nm for Au on glass to 80nm for Au on Si, with a more homogeneous grain-size distribution. Au on Si with film thicknesses below 10nm were also reported [30, 39, 120]. These films have a cluster-like structure with cluster size of 10 to 30 nm laterally and 3 to 10nm in height even with such low film thickness. A mechanism for the nucleation of gold on silicon, which is proposed by Vancea [109] and Mathieu [121], can be used to explain this rough surface. It is based on the formation of an amorphous gold silicide (Au-Si alloy) layer on the silicon surface. With increasing film thickness, new layers of pure gold crystallites are deposited.

(1)   Film Thickness, Evaporation Rate, Annealing Temperature

The influences of parameters, such as film thickness, evaporation rate, and annealing temperature, on the topography of a gold thin film on a Si substrate have been systematically studied by Hammiche et al. [122]. The results show tendencies similar to the Au/mica and Au/glass systems. Surface grains are roughly rounded and randomly oriented. The gold grain size increases with evaporation rate for a given film thickness. On the other hand, for a given evaporation rate, a similar increase in grain size is observed for increasing film thickness. The grain size also increases, while mean roughness decreases with increasing annealing temperature.

(2)   Deposition Methods

The surface topography of evaporated and ion-assisted deposited (IAD) 50nm gold films were studied by STM [123]. The films display rounded structures, with typical grain size of 40-80nm for evaporated films, and 20-40nm for IAD films. The reason that IAD films show a lower average grain size is that the recrystallization effects which normally occur during evaporation growth are disrupted in IAD method.

2.5.4 Au/GaAs

The influences of the deposition methods on Au topography on n-type GaAs have also been studied by STM [124]. Electroless films were obtained with a low content of Pd (4×10^{-6} M), which acted as a catalyst. Evaporated films show hillock structures, uniformly distributed, 5nm in height and 10nm in diameter. On the other hand, electroless films are much less regular, with smaller grains of 10nm in height and 25nm across, and larger grains of 40nm in both the vertical and horizontal directions. The differences in the surface topography reflect the differences in the film growth mechanisms. Thermally evaporated films are controlled by surface diffusion, while electroless films are controlled by the nucleation sites initiated by Pd atoms on GaAs surfaces.

that the material involved has been removed because of copyright restrictions

Fig. 2-1   A schematic view of STM [15].

33

that the material involved has been removed because of copyright restrictions

Fig. 2-2   Electrons have both a wave and particle nature [16]. (a) If the barrier is too
thick, the electrons will be reflected. (b) If the barrier is thin, the electrons can
tunnel across the barrier.

34

that the material involved has been removed because of copyright restrictions

Fig. 2-3 Schematic diagram of the tunneling unit and the vibration isolation stage [21].

35

that the material involved has been removed because of copyright restrictions

Fig. 2-4   Frequency response of the tunneling unit to external mechanical vibrations [22].

that the material involved has been removed because of copyright restrictions

Fig. 2-5   Vibration attenuation of a single stage vibration isolation system for three
different damping factors [22].

that the material involved has been removed because of copyright restrictions

Fig. 2-6 Vibration attenuation for the tunneling unit combined with a single isolation
stage [22].

37

that the material involved has been removed because of copyright restrictions

Fig. 2-7 Two types of vibration isolation stages [20]. (a) multiply stacked metal plates; (b) coil spring suspension with magnet damping.

38

that the material involved has been removed because of copyright restrictions

Fig. 2-8 Schematic diagram of the lever reduction mechanism [20].

39

that the material involved has been removed because of copyright restrictions

Fig. 2-9 Schematic illustration of the operation of inchworm walkers [20].

that the material involved has been removed because of copyright restrictions

Fig. 2-10   Several geometries of STM scanners [22]: (a) bar tripod; (b) tube tripod;
(c) single tube; (d) stacked disks.

41

that the material involved has been removed because of copyright restrictions

Fig. 2-11   Block diagram for the feedback control system of an STM [22].

that the material involved has been removed because of copyright restrictions

Fig. 2-12   Block diagram for a scan controller to adjust the scan size, rotation and position [22].

that the material involved has been removed because of copyright restrictions

Fig. 2-13   The tip coarse reduction positioner of the Burleigh STM [16].

43

that the material involved has been removed because of copyright restrictions

Fig. 2-14   The two operational mode of STM [44].

44

Fig. 2-15   (a) Schematic diagram of dc electrochemical etching/polishing.

(b) Schematic illustration of the dc etching/polishing mechanism [60].

that the material involved has been removed because of copyright restrictions

Fig. 2-16   Schematic diagram of the ac electrochemical etching [47]. (a) downward; (b) upward.

that the material involved has been removed because of copyright restrictions

Fig. 2-17   Schematic diagram of the bubble dynamic mechanisms under ac voltage [47]. (a) downward; (b) upward.

that the material involved has been removed because of copyright restrictions

Fig. 2-18   Schematic diagram of the formation of EBD tip [55].

47

Fig. 2-19   Reconstruction in the case of a parabolic tip and a parabolic image surface [101].

Fig. 2-20   Reconstruction in the case of double contact [101].

48

that the material involved has been removed because of copyright restrictions

Fig. 2-21   The difference between a vacuum gap and a contact gap of an insulator [87].

49

that the material involved has been removed because of copyright restrictions

Fig. 2-22   Schematic diagram of a surface profile [108].

CHAPTER 3. EXPERIMENTAL METHODS[1]

3.1 Tip Preparation

3.1.1 Electrochemical Polishing

The dc downward polishing method was selected as the first stage for tip fabrication. Tungsten tips were prepared by placing several millimeters (1-3mm) of the lower end of a polycrystalline W wire (0.5mm in diameter) into an aqueous NaOH solution (2M or 3M) and applying a positive dc voltage to the wire, making W the anode. The counter electrode (or cathode) was stainless steel. To obtain macroscopically reproducible tip shapes and to study the immersion depth effect on the tip shape and sharpness, a micrometer assembly was used to accurately control the length of wire immersed in the solution. The electrochemical process was carefully monitored and stopped by turning off the voltage when the submerged portion of the wire dropped off. The tip was then immediately withdrawn and washed in two separate water baths for about 7s each.

3.1.2 Ion milling

A Gatan ion mill (Model #600CTMP), which is commonly used for TEM sample preparation, was employed (at room temperature) for the second stage of tip fabrication. Tips were mounted on a tip holder vertically with the tip pointing downward and rotating at 2 rpm in a flux of 4.5 kV Ar ions. A single ion gun was employed using a current

---

[1] A version of this chapter has been submitted for publication.

density of 1 mA/cm^2 and an incident angle of 20° to 40° to the horizontal. This arrangement is shown schematically in Fig. 3-1.

3.2   Tip Characterization

Electropolished tips were examined by a Hitachi S-2700 SEM operating at 20kV, to obtain the overall morphology of the tips made under different preparation conditions. In order to examine the very end of the tip and to compare the tip radius of electropolished and ion milled tips, electropolished tips before and after ion milling were examined by a Philips EM300 TEM operated at an accelerating voltage of 100 kV. The TEM images of tips presented here are all shadow images.

More than 50 fabricated tips were characterized by SEM and TEM, in an attempt to find a reproducible tip-forming procedure.

To obtain the information regarding tip deformation during imaging and the influences of the tip geometry on the STM images, both electropolished tips and ion milled tips (more than 100 tips used in the study), were analyzed before and after STM imaging using TEM.

3.3   Thin Film Deposition

Deposition of the metal thin films on Si(100) and InP(100) was done at Alberta Microelectronic Center (AMC) by means of electron beam evaporation.

3.3.1   Au/Si (100)

For Au/Si (100) samples, the substrate was <100> oriented n-type Si, doped to a level of 10^{15} cm^{-3}. The wafer was cleaned in a 10 : 1 buffered hydrofluoric acid solution

for about 1 min, rinsed thoroughly in deionized running water and blown dry with dry nitrogen. The substrate was loaded into the vacuum chamber immediately after cleaning.

B use samples were also used for BEEM measurement, the Au was fabricated with a two-lobed pattern, with each lobe in a circular form 2.5 mm in diameter. A special shadowing mask was designed, shown in Fig. 3-2, and the substrate was covered by this mask to get the specific pattern. The thickness of the deposited layer required for BEEM was $\leq$ 10nm. The quartz thickness monitor was not suitable as a means of controlling the thickness. Thus, the amount of the gold was calculated according to the thickness, weighed, and evaporated completely during deposition. The base pressure was 1×10^{-6} torr during deposition.

The reason for the specific Au pattern and thickness will be explained in the BEEM section below.

3.3.2 Au/InP

The substrates used were Fe doped <100> oriented InP semi-insulating wafers, with a doping level of 5×10^{16} cm^{-3}. Prior to the Au deposition, the substrate was cleaned using a standard procedure consisting of two steps: (1) Oxygen plasma cleaning using a reactive ion etch (RIE), which is a dry etch to remove organics by oxidizing them. It also oxidizes the InP surface. It was set at 25W power, 51 mtorr pressure, and 110V self bias. The InP sample surfaces were bombarded for 5 min. (2) Etching procedure used to remove the oxide layer on the InP surface. The dry etched samples were dipped in 1:5:450 HF:HNO$_3$:H$_2$O (volume ratio) solution at 25°C for 30s. The substrate was then thoroughly rinsed in deionized running water and blown dry with dry nitrogen. The time between substrate cleaning and the vacuum chamber pumping was about 5 min. Au was deposited under a base pressure of 2×10^{-7} torr with a deposition rate of 0.23nm/s. The film thickness was monitored during deposition by a quartz thickness monitor, but

was more accurately determined by cross section TEM. The gold layer was found to be ≈ 50nm thick.

3.3.3 Au Grating

A gold grating on a glass substrate sample was provided by AMC. The structure has a height of 0.65μm and width of 1.70μm, with an aspect ratio of 0.38, shown in Fig. 3-3.

3.4. Annealing Procedure

After deposition, Au/InP samples were sectioned into 1cm x 1cm pieces in order to fit the STM mounting stage. Annealing was done in a small quartz furnace. The furnace temperature was monitored and controlled by an electronic controller. After placing a sample in the furnace and closing the chamber, the chamber was purged with forming gas (N_2 + 5%H_2) for 5 - 10 min. Annealing was also done in forming gas. Annealing temperatures ranged from 175°C to 450°C for various times. The annealing regime is listed in Table 3-1. After annealing, the furnace was not opened until it had cooled down to 50°C, with continued purging. Purging with forming gas helps prevent any surface degradation due to oxidation because any oxidation on the surface would cause noise in the STM images or even prevent STM imaging.

3.5 STM Apparatus

The details of the Burleigh STM modification will be described in the BEEM section. The modified STM was tested for both electronic delay and thermal stability. For electronic delay tests, the STM was operated at different scan delays (5ms and 10ms)

and scan directions (scans from left to right and from right to left) while imaging the gold grating structure discussed in Section 3.3.3. For thermal stability tests, the zoom capability of the STM was utilized to observe change in microstructure at a specific location of the Au/InP sample annealed at 400°C, during a 30min imaging period.

3.6 Au Film Microstructural Characterization

3.6.1 TEM

The grain size and thickness of the gold thin films on both the Si and InP substrates were obtained from plan view and cross section samples using a Hitachi H-7000 TEM operating at an accelerating voltage of 125kV.

(1)   TEM Specimen Preparation

Both plan view and cross section TEM specimens were prepared by mechanical thinning, followed by either ion milling or chemical thinning [125, 126]. The procedure for plan view specimen preparation is summarized as follows: An ultrasonic disc cutter was used to cut 3mm discs from the specimens. These were polished from the substrate side down to a thickness of about 200µm. The discs were then dimpled from the substrate side, to a central thickness of about 50µm for the Au/InP samples, and to a small hole or optical transparency at the center for the Au/Si samples. Chemical thinning from the InP side in a 1% Br in methanol solution was used as the final step for the Au/InP samples, and ion milling from the Si side as a final step for the Au/Si samples.

The procedures for cross section specimen preparation include the following: Two 1.5mm x 5mm slabs were cut from the specimen, glued together face-to-face with three Si or InP slabs at each side, and cured at 100°C for 1h. After curing, the structure was thinned to about 600µm, and a 3mm disc was cut at the centre of it. The disc was then

ground to a thickness of about 200μm, dimpled from one side to about half the thickness and polished. The other side of the disc was dimpled to a small hole or optical transparency at the center and polished. Ion milling was used as the final step. Both sides of the specimen were sputtered while the specimen was cooled with liquid nitrogen.

Details of the preparation procedures for both plan view and cross section specimen can be found in Ref. 127.

(2)   Topographical and Structural Information

Both bright field and dark field images were used to determine the grain size and the topography of as deposited and annealed films. The dark field images were taken using the 220 reflection of Au.

Selected area diffraction (SAD) was used to monitor the polycrystalline growth of the thin films. Phase changes during annealing of the Au/InP samples were also identified using convergent beam electron diffraction (CBED). Both the SAD and CBED patterns were obtained from a Hitachi H-7000 TEM.

3.6.2   STM

Prior to TEM analysis, all specimens were examined by STM to obtain topographical information. STM images were obtained from a modified Burleigh STM operated in air and at room temperature. All images were taken in the constant current mode. The tip was biased at -50 mV relative to the sample with a tunneling current of 2 nA. Electropolished W tips, ion milled W tips and mechanically cut Pt-Ir tips were used for imaging. STM images were taken on the same day as the deposition or annealing for the Au/InP samples, and seven days after deposition for the Au/Si samples. The STM images for both Au/Si and Au/InP samples have not been processed, except for leveling, while the STM images of the gold grating are not leveled.

56

3.6.3 AFM

Only Au/Si (100) samples were examined by AFM at CANMET. The images were obtained using a Topometrix TMX 2000 Discoverer Scanning Probe Microscope (SPM) operated in AFM contact mode. The force between the tip and sample was set at 0.08 nN, with a scanning speed of 4 - 8 Hz. EBD tips were used for imaging. The tips were grown in the SEM, which was operated at 20kV and a filament emission current of 75-100μA at a working distance of 5-12mm. The beam was positioned at the end of the pyramidal shaped Si_3N_4 tips for various time intervals. Repositioning was required due to beam drift. Tip lengths of 1.5-2.0μm (determined by SEM) were obtained after 45min of growth time. The AFM images have not been processed, except for leveling. AFM images were taken seven days after deposition.

Table 3-1.　　The annealing regime for Au/InP samples.

Temp (°C)	175	275	320	360	400	450
Time	0.5	0.5	0.5			
(hrs)	1	1	1	1	1	1
	4	4	4			
	18	18	18			
			65			
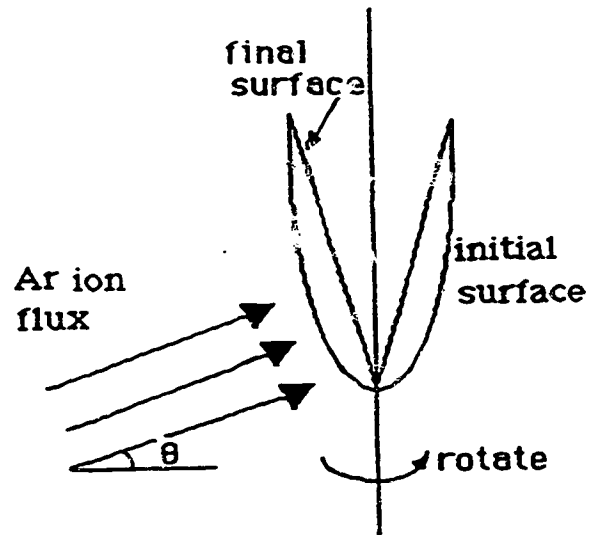
Fig. 3-1   Schematic illustration of ion milling process.

75mm sq.
stainless steel
shim, 0.015"
thick

2.50mm   0.50 mm   2.50mm

0.25mm

1.25 cm

1.25 cm

1.25 cm

1.85 cm   1.85 cm   1.85 cm
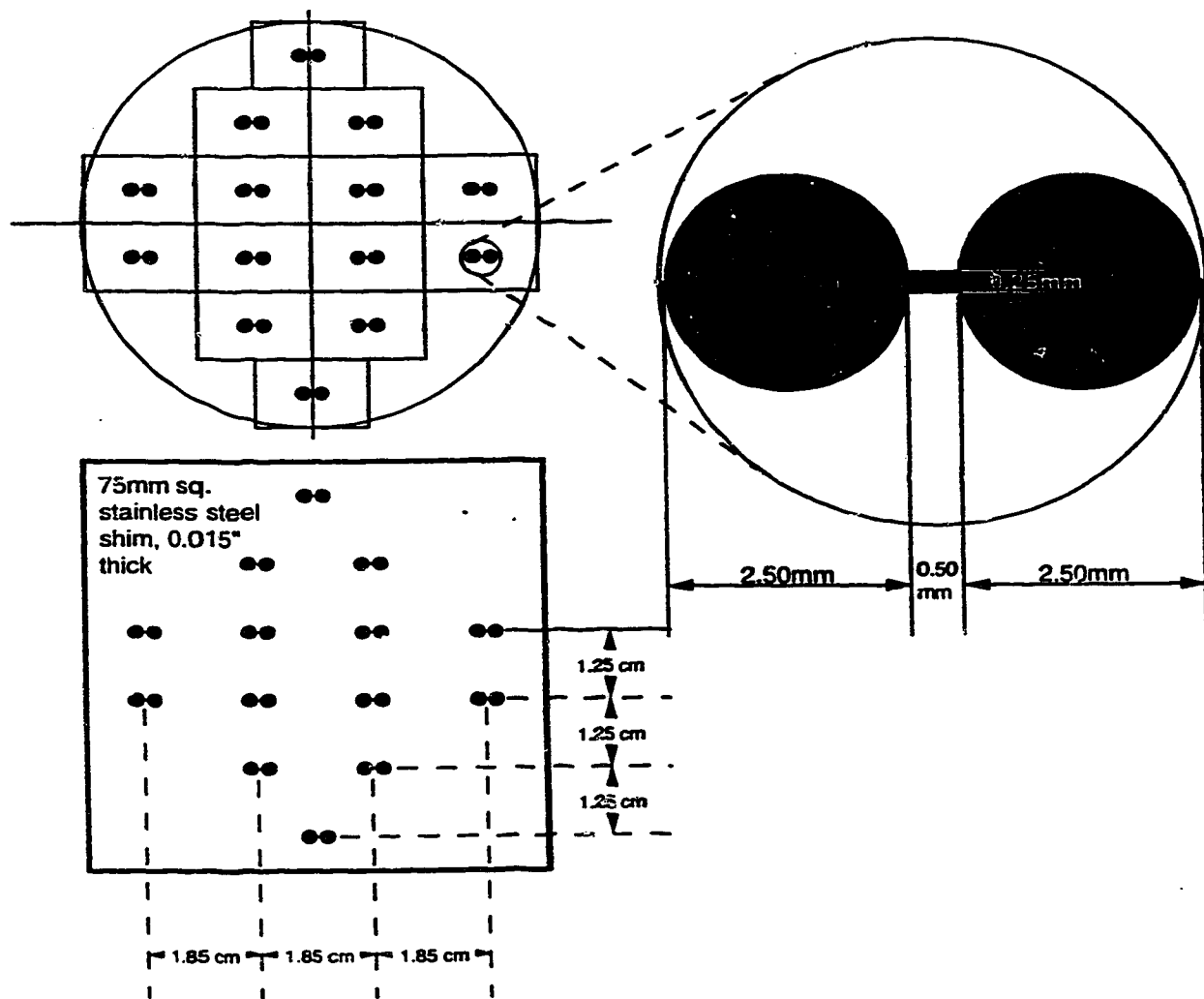
Fig. 3-2   Schematic diagram of the shadowing mask.

60
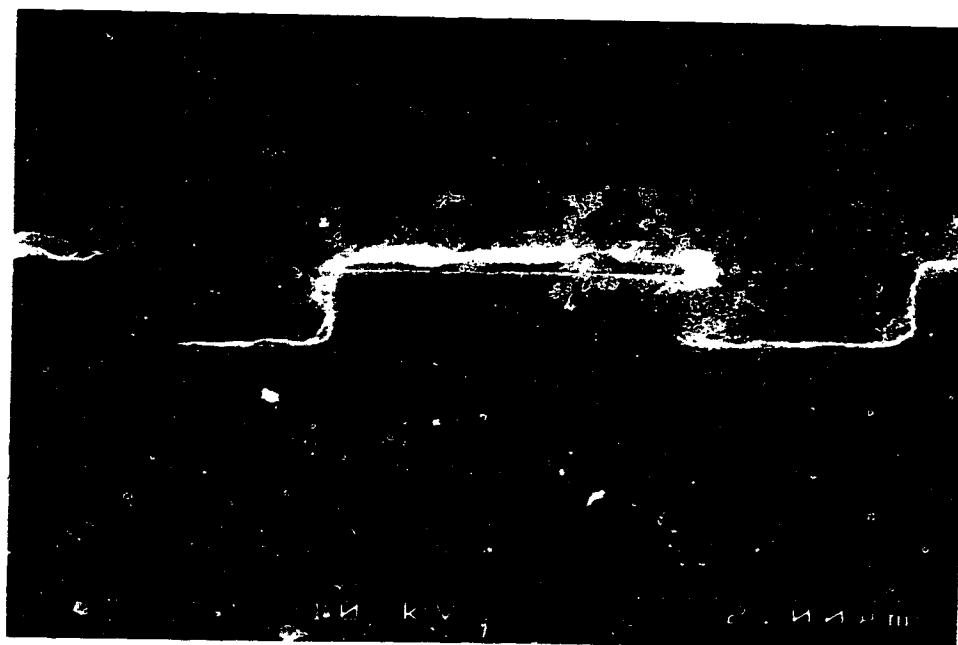
Fig. 3-3   SEM secondary electron (SE) image of gold grating structure.

CHAPTER 4. RESULTS AND DISCUSSION[2]

4.1   Tip Preparation and Characterization

4.1.1   Electrochemical Process

The electrochemical process is comprised of etching, polishing or pitting, which depend on the current-voltage (I-V) relationship. Etching and pitting remove material at different rates locally producing surfaces with rough topography, and depend on factors such as crystallographic orientation, composition and microstructure. Polishing tends to be insensitive to the above factors, removing material more rapidly from protrusions, producing a smoother surface. Since polycrystalline W was used to fabricate tips, the polishing regime was selected to produce well defined tip surfaces. Typical I-V curves are shown in Fig. 4-1 for 2M and 3M NaOH solutions, for a wire immersion depth of 2mm. Taking into account both polishing time and solution stability as will be discussed below, 11V and 9 V were selected as the polishing conditions for 2M and 3M NaOH solutions respectively.

When W wire is dipped into a NaOH solution, surface tension effects between the solution and wire control the interface shape (Fig. 4-2). On application of a positive voltage to the wire, the W will be oxidized to WO_4^{2-} which goes into solution. The overall electrode reactions are given below [60]:

$$\text{cathode:}\quad 6\ H_2O + 6\ e^- \rightarrow 3\ H_2\ (g) + 6\ OH^- \tag{4-1}$$

$$\text{anode:}\quad W\ (s) + 8OH^- \rightarrow WO_4^{2-} + 4\ H_2O + 6\ e^- \tag{4-2}$$

$$\text{overall:}\quad W\ (s) + 2\ OH^- + 2\ H_2O \rightarrow WO_4^{2-} + 3\ H_2\ (g)\quad (E^\circ = -1.43\ V) \tag{4-3}$$

---
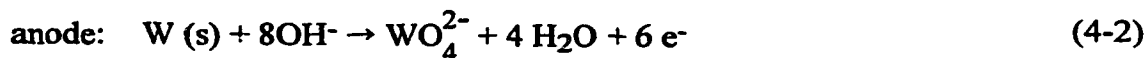
[2] A version of this chapter has been submitted for publication.

The reaction mechanism is much more complex and the actual reaction involves a number of side reactions.

A sheath of descending WO_4^{2-} around the lower part of the W wire shields it from further NaOH attack [60]. Thus, the reaction occurs mainly near the liquid surface, resulting in a necked-in effect.

4.1.2. Polishing Parameters

Electropolished tips exhibited nearly exponential shapes (Fig. 4-3), due to the slow decrease in current before the lower portion of the wire dropped off. Microscopically, maintaining a higher current means the concentration of OH⁻ at the W-liquid interface is higher, producing additional WO_4^{2-}. The effects of initial current (I1) and final current before drop-off (I2) are shown in Table 4-1. The initial current I1 increases as the length of the W wire in contact with the solution increases, however, tip shape remains unchanged. Sharp tips can be reproducibly fabricated when the current is maintained at I1 for at least half the process time, before it slowly decreases to I2, prior to drop-off.

Parameters, such as voltage, solution concentration and immersion depth, will affect the distribution of WO_4^{2-} and OH⁻ in the electrolyte during the polishing process and change the interface shape, affecting the tip shape and sharpness.

(1)   Voltage

A higher dc polishing voltage will reduce the processing time, thereby minimizing outside disturbances. On the other hand, additional oxygen bubbles form from water or OH⁻ at the anode as a consequence of the higher voltage. Although the number of

63

bubbles is insignificant compared to ac etching, bubbles do disturb the stability of the solution around the neck-in region, particularly for fresh solutions, so that maintenance of the distribution of WO_4^{2-} and OH^- is not easy. The surface level always drops a little due to the neck-in effect, with a second neck-in region forming beneath (Fig. 4-4). Studies of voltage effects show that for 2M NaOH and 3M NaOH solutions, voltages of 10-11 V and 8-9 V respectively will produce good tips. Voltages below 9V for 2M solutions and below 7V for 3M solutions will result in much longer processing times (more than 30 min), reducing stability, and increase the likelihood of poorly defined tips.

(2)   Cutoff Time

The important factor in making sharp tips is the response time to turn off the voltage after drop-off, i.e., cutoff time. A delay of only 1s can result in a broadened tip with a large cone angle (Fig. 4-5).

(3)   Immersion Depth

The effect of immersion depth has also been studied. Tips with an immersion depth of 3mm in both 2M and 3M solutions had, in addition to a macroscopic exponential shape, bent points (Fig. 4-6). It appears that too much of the wire is submerged in this case leading to, according to Nicolaides et al [61], recoil or plastic flow when the tip is formed.

Table 4-2 summarizes the electropolishing results. The total processing time for a 2M NaOH solution at 11V is 12-14 min, which produces tips with a radius of curvature of 200-250 nm and a cone angle of 25-35° at an immersion depth of 1-2 mm. Similar tips were obtained with 3M NaOH solutions at 9V and an immersion depth of 1.5-2 mm, after a total processing time of 7-8 min. Tip reproducibility was better than 90%.

64

4.1.3   Ion Milling

Biegelsen et al [52, 53] have reported that ion milling is a useful technique for removing the thin oxide layer, which invariably forms during the electrochemical polishing process, and reducing the tip radius. Although our ion milling set up (Fig. 3-1) is different from theirs, the results are quite similar. Parameters such as voltage and current density affect thinning time, while incident angle affects the cone angle. Too small an incident angle will result in a larger tip cone angle. The optimum time for ion milling appears to be 30-40 min for a current density of 1mA/cm^2 and an incident angle of 30°. TEM images of tips before and after ion milling are shown in Fig.4-7, for 2 different ion milling times. For an ion milling time of 40 min, the tip radius is reduced from 250nm to 20nm and the cone angle is reduced from 35° to 25° (Fig. 4-7a and 4-7b). For longer milling times, blunted tips or even multiple tips can form (Fig. 4-7c), which has been reported previously [52]. Multiple tip formation is due to the polycrystalline nature of W and selective thinning at W grain boundaries [52].

4.2   STM Apparatus

In order to obtain reproducible images, not only the shape and sharpness of the tips are important, but also good STM stability is necessary. The basic designs involving mechanical stability and electronic control, and the basic operation of the Burleigh STM were provided in the literature review. The scan rate of the Burleigh STM was substantially reduced after the modification, which will be described in the BEEM part. As a result, stability and thermal drift become more important.

Fig. 4-8 shows STM images of an Au/InP sample after annealing at 400°C for 1h. The scan delay (dwell time at each pixel) was increased to 2ms to obtain noise free images. From Fig. 4-8b to 4-8d, the magnifications are increased to obtain finer detail of

the central structure/hole in Fig. 4-8a. The time lag between each image (pixels of 256 x 256) recording was typically 5-8min corresponding to a 2ms scan delay. Within this 30min interval (for 4 images), a certain structure in the central part of the image can be captured and expanded to search for finer detail. This indicates that the STM has reasonable high stability and low thermal drift, which is necessary for imaging.

To test both the W tips and the modified instrument further, a gold grating, shown in Fig. 3-3, was used.

Three kinds of tips were used for imaging: electropolished tips, ion milled tips and mechanically cut Pt-Ir tips. Because the aspect ratio of the cut Pt-Ir tip is too small, usually 0.3 or smaller, Pt-Ir tips were unable to generate images of the structure. In fact, the tip constantly crashed into the edge of the structure, even for large scan delays of 10ms. Both the electropolished W tips with an aspect ratio of 1 and the ion milled W tips with an aspect ratio of 2 to 3 give similar images, scanned from left to right, shown in Fig. 4-9a, with a scan delay of 10ms. Two observations were made: (1) ion milled tips and electropolished tips produce virtually the same STM images; (2) the images always show a tapering effect on the left side of the structure when the tip is scanned from left to right.

To explain the first point, we examined both types of the tips, after imaging, in the TEM (Fig. 4-10). Ion milled tips show a severe bending after several images were scanned (Fig. 4-10a), while the electropolished tips were flattened at the very end of the tip (Fig. 4-10b). One explanation is that the ion milled tip is too thin to withstand sudden changes in topography. Although the initial radius of the ion milled tips is much smaller than the electropolished tips, ion milled tips start bending as soon as the scan begins, so that the virtual tip radius of both tips are similar. In addition, electropolished tips lasted much longer than the ion milled tips. Fig. 4-9b is the last image scanned by the ion milled tip before the tip was imaged in the TEM. Comparison of the right side of the

66

structure shown in the STM images (Fig. 4-9a and b) shows the tip deformation effect on the image.

During imaging, I suspect that the tapering effect at the left side of the structure was caused by the electronic delay. As a result, the scan delay and scan direction were varied. Fig. 4-11 shows line scans with a scan delay of 5 ms. A scan from right to left is shown in Fig. 4-11a and a scan from left to right in Fig. 4-11b. Fig. 4-12 shows similar line scans with a scan delay of 10 ms. From the figures, we can see that the tapering effect occurs at right side during scanning from right to left, and occurs at left side during scanning from left to right. Also, the tapering length was approximately doubled for a scan delay of 5ms compared to a scan delay of 10 ms. A long scan delay gives the tip more time to respond to changes in topography. These results confirm that electronic delay is the main reason for the imaging artifacts in the gratings.

For all subsequent STM studies reported here, several scan delays were tried until the images at the different scan delays were similar to reduce the electronic delay effect. For surfaces with topographies at nanometer to submicrometer scales, scan delays of 2ms to 5ms are usually adequate.

4.3   STM Imaging

4.3.1   Tip Geometry Effects

(1)   Au/Si(100)

In order to test the W tips, Au/Si(100) samples were used. Fig. 4-13 shows TEM images of the Au/Si(100). The Au film is continuous but very much nonuniform, with a thickness varying from 8-33 nm, which is, at least in part, caused by the significant diffusion of Au into Si [121]. The Au grain size was measured from the plan view image and determined to be 20-50 nm.

Three types of tips were used for imaging the Au/Si sample after deposition for seven days. Mechanically cut Pt-Ir tips were unable to produce noise free images. The reason for this is not clear at this time, however, it may be related to the electronic states of both the tip and sample, which will be discussed further. Both electropolished W tips and ion milled W tips can produce STM images, although a little distortion can be seen in the images. Fig. 4-14 shows TEM images of an ion milled W tip before and after STM imaging of the Au film. The tip radius was originally 20nm with a cone angle of 23°. After scanning the tip is broadened and contaminated. TEM images of an electropolished W tip before and after scanning of the same sample are shown in Fig. 4-15. The tip radius is about an order of magnitude larger than the ion milled tip (200nm vs. 20nm) and the cone angle is 35°. Again, after scanning the tip is contaminated and slightly deformed at the end. STM images of Au/Si(100) obtained with the two tips are shown in Fig. 4-16. The Au grains exhibit a typical hillock structure. The apparent grain size for the ion milled tip is 40-90 nm with a typical peak-to-peak roughness of 25nm (Fig. 4-16a), while the maximum height variation for the image is about 70nm. The apparent grain size for the electropolished tip (Fig. 4-16b) is larger, i.e., 90-160 nm, although the peak-to-peak value remains similar (22nm), and the maximum height variation is about 70nm.

The STM results were also compared with AFM images, taken with EBD tips, of the same Au film (Fig. 4-17), seven days after deposition. The EBD tips had similar tip radii to the ion milled STM tips, but with higher aspect ratios. The apparent grain size from the AFM images is 30-90 nm with a typical peak-to-peak roughness of 23nm, while the maximum height variation is again around 70nm. The TEM, STM and AFM results are summarized in Table 4-3 for comparison purposes.

According to Keller [101], the reconstructed true surface grain radius is equal to the STM image grain radius minus the tip radius (or plus the tip radius in the case of a hole). When the tip radius is smaller than or equal to the grain size, as for the case of ion milled tips in the STM or EBD tips in AFM, the true grain radius is roughly within the

range of the STM or AFM grain radius minus the tip radius (here, half the grain size is used instead of the curvature of the Au grain). However, for the case where the tip radius is much larger than the grain size (electropolished tips), although Au grains can be resolved, the grain size resulting from these tips does not fit the reconstructed theoretical calculation. The grain size is doubled compared to the grain size resulting from sharper tips. Also, the broad tips may not protrude between the grains. Fig. 4-18 schematically illustrates this effect. Grains 1, 4, 5, 7 can be resolved by the tip, although the images of those grains are much larger than the actual size. Grains 2 and 3 may be resolved as one grain in the image, and grain 6 shows up as a hole. This result can be drawn by comparing Fig. 4-16a and b.

The STM and AFM imaging was done after the same period of time (7 days) following deposition to permit direct comparison. Diffusion of Au into Si is so significant even at room temperature, and the gold layer is so thin that the topography and the surface electronic states will change significantly. Mechanically cut Pt-Ir tips can produce reasonable images within the first three days after deposition. Fig. 4-19 shows an image of an Au/Si sample taken with a Pt-Ir tip right after deposition. The image exhibits a very smooth surface with a grain size of 8-18nm, a peak-to-peak value of 3-8nm, and a maximum height variation of around 10nm. It is believed that this image reveals the true Au surface structure. The effect of the tip radius is much less significant in this case because of the much smoother surface so that the tip does not have to protrude deeply between the grains. Therefore only atoms at the very end of the tip are contributing to the tunneling. However, because of the significant diffusion caused by the TEM sample preparation procedure, this interpretation cannot be verified by the TEM.

(2)   Au/InP

To further verify the interpretation regarding tip effects on smoother surfaces, Au/InP samples were imaged. Fig. 4-20 shows TEM images of Au/InP. The Au film is very uniform with a thickness ranging from 50-57nm. The gold film is polycrystalline, with twins clearly visible from the bright field image. The grain boundaries between preferentially oriented crystals may be obscured in bright field images, resulting in apparent larger grains [123]. In order to reduce this effect, the grain sizes were measured from the dark field images, taken from the 220 reflection of Au in the SAD pattern. The grain size was determined to be 12-50nm.

Again, three tips were used for STM imaging. Electropolished tips were unable to produce noise free images in this case. Both mechanically cut Pt-Ir tips and ion milled W tips produced STM images (Fig. 4-21), with no apparent difference for the two tips. The Au grains show a typical hillock structure and the grain size is 8-25nm. The peak-to-peak roughness is 3-10nm, while the maximum height variation is around 16nm. The grain size obtained from the STM image is consistently a little smaller than that obtained from the dark field TEM images. The larger grains, despite being single grains, may have multiple "mounds" on the surface which are imaged by the STM as apparent grain boundaries. Therefore, for the ⸴   ˙ surfaces, the tip radius effects are much less significant, and STM images can be interpreted by considering that the images are produced by the very end atoms of the tips.

(3)   Image Artifacts

Another important result related to tip geometry is an artifact caused by the tip itself, which is visible in the STM images. The grains appear to be elongated in one direction. This is due to an asymmetric tip, the apex of which can be approximately estimated by an ellipsoid. In the direction of the smaller semi-axis, the resolution may be higher, but in the other perpendicular direction the hills are stretched and smoothed, owing to the convolution of the tip with the surface features. The effect can be seen in

the image, shown in Fig. 4-22, which is taken by an ion milled W tip on a Au/InP sample annealed at 320°C for 18h.

4.3.2 Tip Electronic States

As has been noted during the above study, Pt-Ir tips cannot produce images of Au/Si(100) samples seven days after deposition. Significant Au diffusion into Si has taken place. The electropolished W tips, which have several nm of oxide on the very end of the tip, cannot produce images of Au/InP samples. Only ion milled W tips can produce images of Au/InP samples which have been annealed at 320°C for 18h. Pt-Ir tips can only produce images of samples annealed below 320°C (These results will be discussed further in subsequent sections). These results indicate that not only the electronic states of the tip, but also the electronic states of sample, play important roles in STM imaging, although experimental determination of these electronic states is very difficult as has been mentioned in the review part.

The experimental relationships among STM images, the tip type and samples are summarized in Table 4-4. This table indicates tip geometry effects on both smoother and rougher surfaces, and influences of electronic states of both the tip and the sample on the STM image quality.

4.3.3 Thin Film Topography

The microstructures of Au/InP contacts and the reactions during annealing have been systematically studied using TEM, especially cross section images and SAD patterns [128, 129]. Surface morphological changes during annealing have not been

71

studied as extensively, although limited characterization has been done through TEM of plan view samples [129]. To our knowledge, there has been no STM study of this system. Thus this study is focused on the surface topography changes after annealing at various temperatures and times, using both STM and TEM.

The advantage of the STM is obvious: (1) high resolution on the nanometer scale even under ambient atmosphere; (2) sample preparation is trivial and nondamaging. On the other hand, TEM has some complimentary capabilities: (1) ability to identify the crystallographic structure of specific regions by using electron diffraction and dark-field techniques; (2) interpretation of TEM images is well understood; (3) microanalysis of small regions using energy dispersive x-ray (EDX) analysis .

Fig. 4-20 shows TEM images of a gold film on InP. The plan view images (both bright field and dark field images) and SAD pattern remain unchanged up to 320°C and 18h annealing. The film retains its gold color. All these indicate that there is no phase change. The grain size, determined from dark field images, is 12-50nm.

On the other hand, the STM images remain unchanged after annealing up to 275°C for 4h, with a typical hillock structure, as shown in Fig. 4-23. The gold grain size is 8-25nm, with a typical peak-to-peak roughness of 3-10nm. The STM images of samples annealed at 275°C for 18h shows some porous regions, a slightly larger grain size of 10-30nm and a larger peak-to-peak roughness of 7-20nm (Fig. 4-24a). The other regions remain unchanged. STM images from the 320°C/18h sample show occational small holes with the other areas retaining the hillock structure (Fig. 4-24b). The occasional porous surface image observed can be explained as a result of Au grain

72

coalescence during annealing. On the other hand, TEM images cannot distinguish the holes, since holes in the surface layer might be obscured by underlying grains.

STM images of Au/InP samples annealed below 320°C or at 320°C for less than 18h were obtained by both ion milled W tips and mechanically cut Pt-Ir tips, with similar results. For samples annealed at temperatures higher than 320°C or at 320°C for 18h and 65h, cut Pt-Ir tips were unable to produce STM images, while ion milled W tips still produced similar quality STM images.

Upon annealing at 320°C for 65h, phase transformations occur and the film locally changes from a gold color to pink. Annealing at 360°C and 400°C for 1h gives similar results. At 450°C and 1h, the entire film turns to pink. The TEM images from the gold area and the pink area are shown in Fig. 4-25. Indexing of the CBED pattern taken from Fig. 4-25b indicates that the phase is Au_3In (Fig. 4-25d), which is consistent with previous TEM study [129]. Surprisingly, TEM images taken from the gold area (Fig. 4-25a) shows similar Au_3In grains as those shown in Fig. 4-25b, meaning that only the very top layer of Au remains as the Au-In solid solution while the region below has already transformed to Au_3In. The grain size of Au_3In can vary significantly, ranging from 100nm to 600nm, and remains upon annealing to 450°C (Fig. 4-26).

STM results verify this interpretation. Fig. 4-27a and b are STM images taken from the gold area of the 320°C/65h sample and the 360°C/1h sample, showing similar hillock structures with much larger and more numerous holes, illustrating the existence of gold at the sample surface. An STM image of the 450°C/1h sample is shown in Fig. 4-28. Au_3In grain boundaries are clearly seen with a similar grain size to those in the TEM images. The mounded structure within a single Au_3In grain was found in both STM and TEM images and is an evidence of the existence of Au (even not completely transformed upon annealing at 450°C).

73

These observations can be explained in terms of the diffusion mechanism in the Au/InP system during annealing. According to previous study [130], during low temperature annealing, In out diffuses into the Au metallization layer forming a Au-In solid solution. The In content increases during annealing until it reaches the solid solubility limit. At higher temperature annealing, the out-diffusion of In causes the saturated solid solution to transform to Au_3In via the kickout mechanism [130, 131]. Indium atoms displace Au atoms and become substitutional in the Au lattice while the "kicked out" Au atoms take interstitial positions. This kickout process results in a highly localized phase change, being active only at the grain boundaries between Au_3In and the saturated Au-In solid solution, resulting in a different phase transformation rate at different locations.

4.4   Tip Deformation

As mentioned previously, tip deformation can occur during STM imaging. Here, the tip deformation after scanning under different conditions is examined using TEM. An ion milled W tip, after scanning 10 images of a Au/Si(100) sample, seven days after deposition, is shown in Fig. 4-29a. The tip is bent without crashing into sample. Garnaes et al [82] have attributed tip bending to the presence of an oxide layer on the surface. However, we have not observed bending in electropolished W tips, only in ion milled tips, where the oxide layer has been removed. The electropolished tips do flatten severely after crashing into a sample (Fig. 4-29b), but are too thick to bend. Ion milled tips bend severely after sample crashing (Fig. 4-29c). On the other hand, ion milled tips do not bend after multiple scans (more than 20 images) on smoother as deposited Au/InP samples. A small amount of deformation at the very end of the tip occurs, similar to that shown in Fig. 4-14. In the conventional view of STM, the tip-sample separation is assumed to be sufficiently large to allow only weak coupling between their electronic

states. In this case, the tunneling can be described by the transfer Hamiltonian approach, and the tunneling current is exponentially dependent on the separation. As the tip-sample distance decreases, the potential barrier is lowered and even collapses, which causes significant rearrangement of the electronic structures of the sample and tip, inducing an attractive (bonding) forces. In the case of rougher surfaces, the feedback electronics is unable to keep up with sudden topographic changes, so the distance between the tip and the sample decreases momentarily. If this force exceeds the the yield strengh of the tip, irreversible tip deformation occurs. Thus tip bending is not related to surface oxide in this case, but is due to the small tip radius, the rough topography of the sample surfaces, and the response of the feedback electronics. Moreover, electropolished tips last much longer than ion milled tips for rougher surfaces, such as Au/Si(100) and more significantly gold gratings. A possible explanation for this is that the tip radius of the ion milled tips is too small to withstand prolonged scanning without bending under rougher surface conditions.

Table 4-1. Relationship among the immersion depth d of W wire, the initial current I1 and the end current I2 just before drop-off.

	d (mm)	I1 (mA)	I2 (mA)
2M NaOH, 11V	1	30	20
2M NaOH, 11V	2	40 - 50	30
2M NaOH, 11V	3	60 -70	40
3M NaOH, 9V	1	50 - 60	30
3M NaOH, 9V	1.5	70 - 80	40
3M NaOH, 9V	2	100 - 110	50
3M NaOH, 9V	3	120 - 160	80 - 90

Table 4-2. Summary of electropolishing results.

Solution concentration	voltage	total time	immersion depth	results
2M NaOH	11V	12 - 14 min	1 mm	tips sharp
2M NaOH	11V	12 - 14 min	2 mm	tips sharp
2M NaOH	11V	12 - 14 min	3 mm	half of the tips bent
3M NaOH	9V	7 - 8 min	1 mm	tips a little broadened
3M NaOH	9V	7 - 8 min	1.5 mm	tips sharp
3M NaOH	9V	7 - 8 min	2 mm	tips sharp
3M NaOH	9V	7 - 8 min	3 mm	half of the tips bent

Table 4-3.   Comparison of grain size and peak-to-peak roughness of Au/Si(100) samples, seven days after deposition using various imaging techniques.

	grain size (nm)	peak-to-peak roughness (nm)	tip radius (nm)	tip cone angle (°)
TEM	20 - 50	---	---	---
STM (ion milled tip)	40 - 90	25	20	23
STM (electro-polished tip)	90 - 160	22	200	35
AFM(EBD tip)	30 - 90	23	20	10

Table 4-4.   The relationship among STM images, tips and samples.

	Au/Si(100) same day after deposition	Au/Si(100) seven days after deposition	Au/InP as deposited & annealed up to 320°C 4h	Au/InP annealed at 320°C 18h or higher or longer
mechanically cut Pt-Ir tips	images with little tip geometry effects	-----	images with little tip geometry effects	-----
electropolished W tips	images with a little noise	images with significant tip geometry effects	-----	-----
ion milled W tips	images with little tip geometry effects	images with tip geometry effects	images with little tip geometry effects	images with tip geometry effects

78
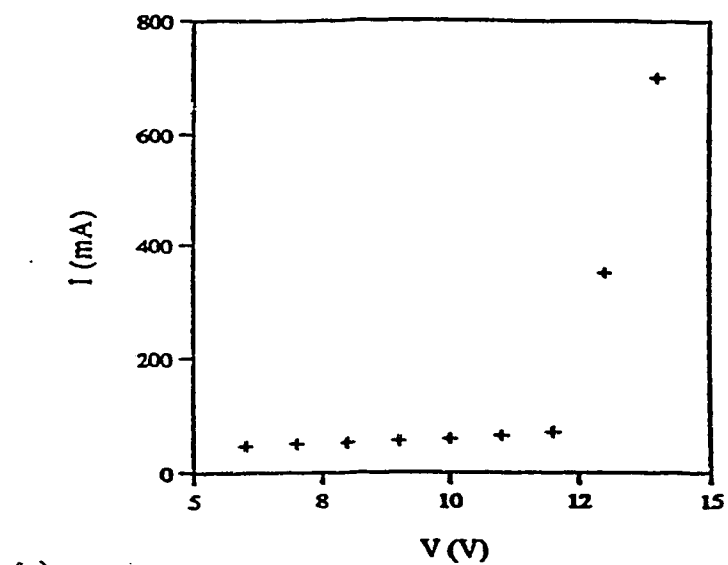
(a)
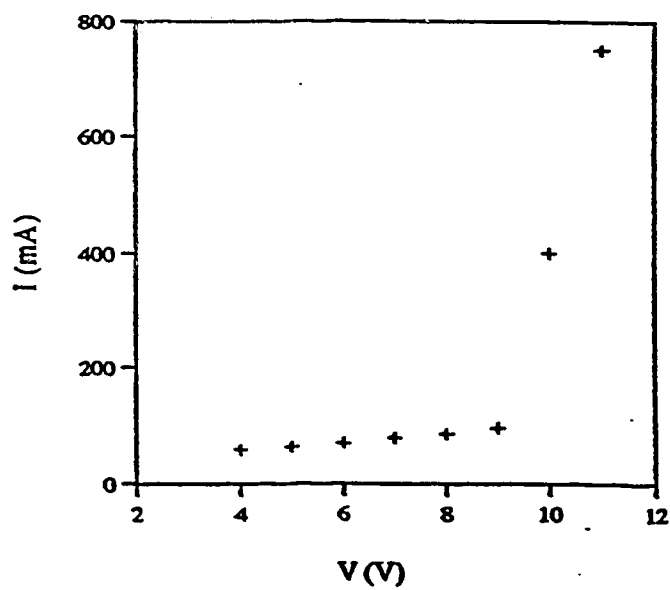
(b)

Fig. 4-1   Current (I) vs voltage (V) curves for electrochemical processing of W wire
with an immersion depth of 2 mm.   (a) 2M NaOH solution;   (b) 3M NaOH
solution.
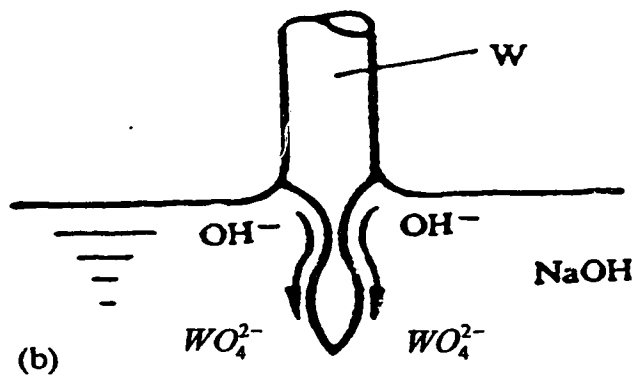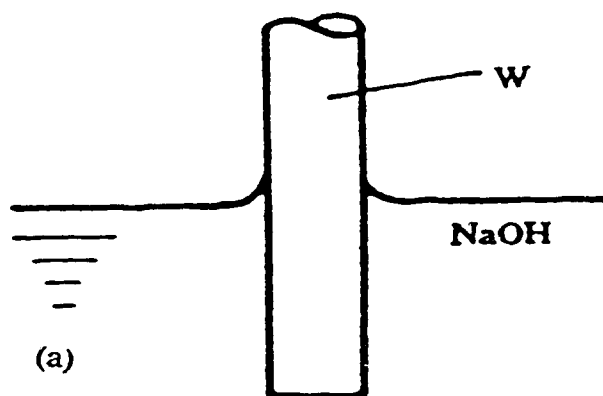
Fig. 4-2 Schematic diagram showing the shape of the solution-air-W interfaces [60].
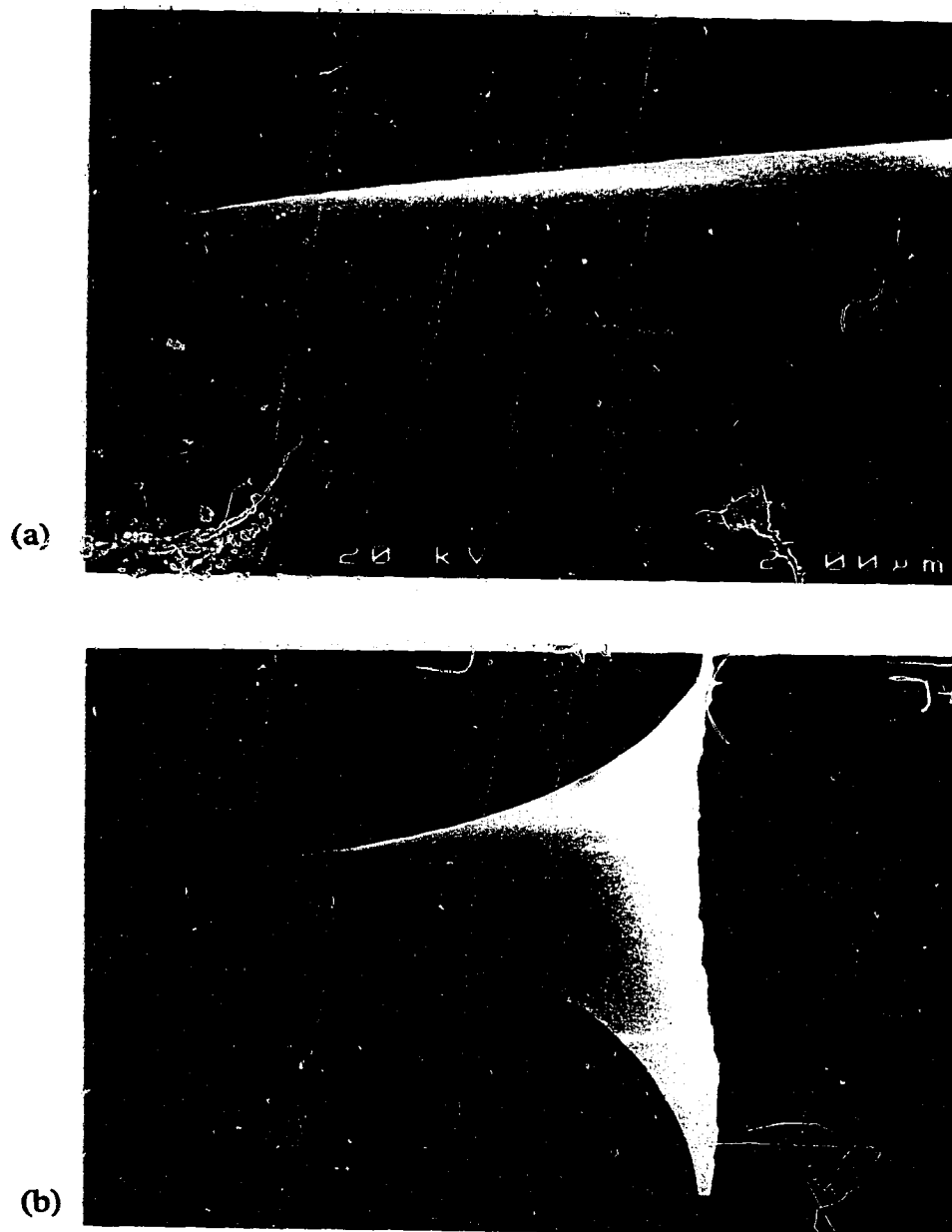
Fig. 4-3   SEM SE images of electropolished W tips.   (a) high magnification image
showing the radius of the tip; (b) low magnification showing the shape of the
tip.

81
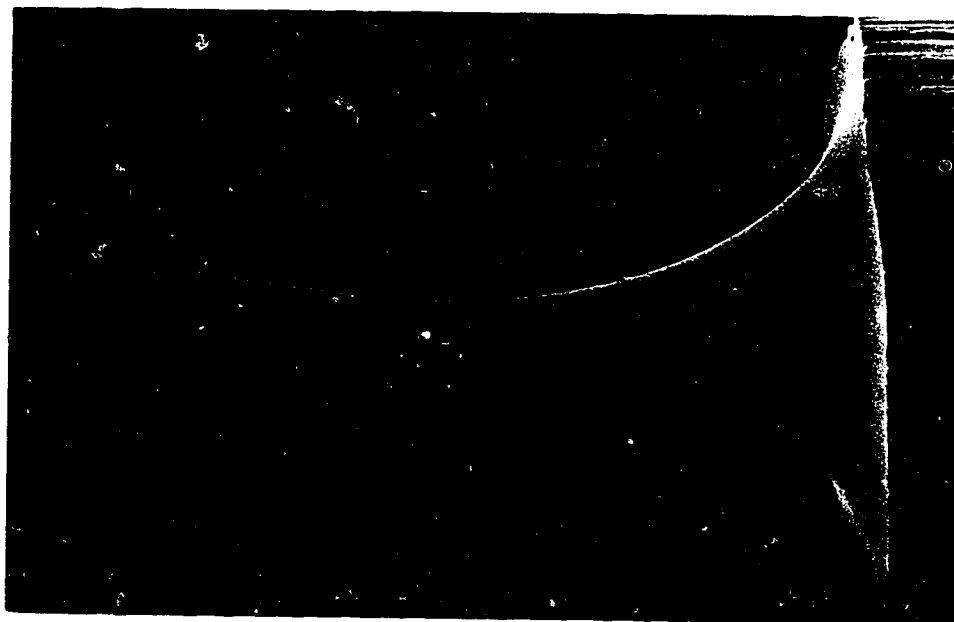
Fig. 4-4   SEM SE image of W tip showing double necked regions. This is due to
changing surface tension effects during processing.

82

Fig. 4-5   SEM SE image of a W tip, showing the blunting effects of delay to cutoff.
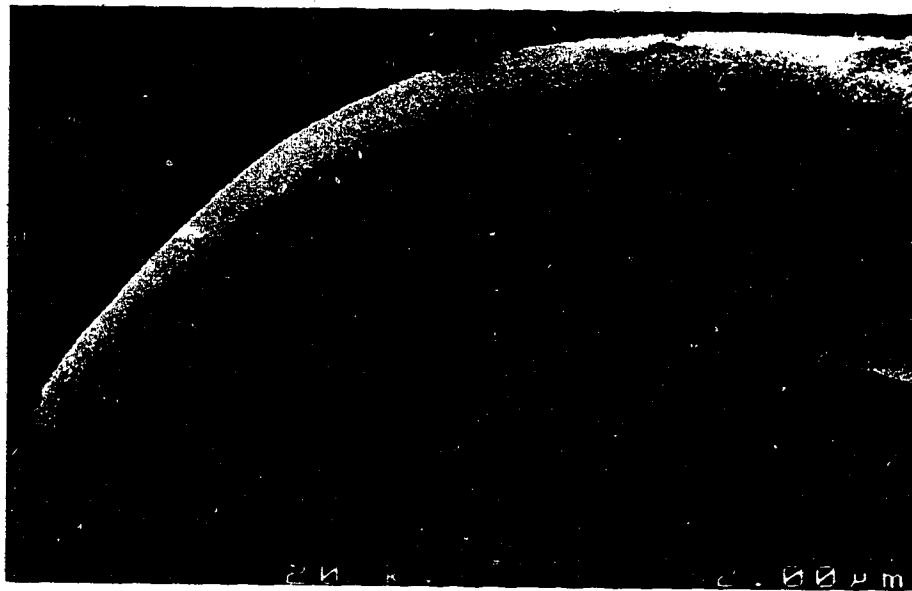
Fig. 4-6   SEM SE image of W tip processed with a 3 mm immersion depth.

83

(a)

(b)

(c)

500nm
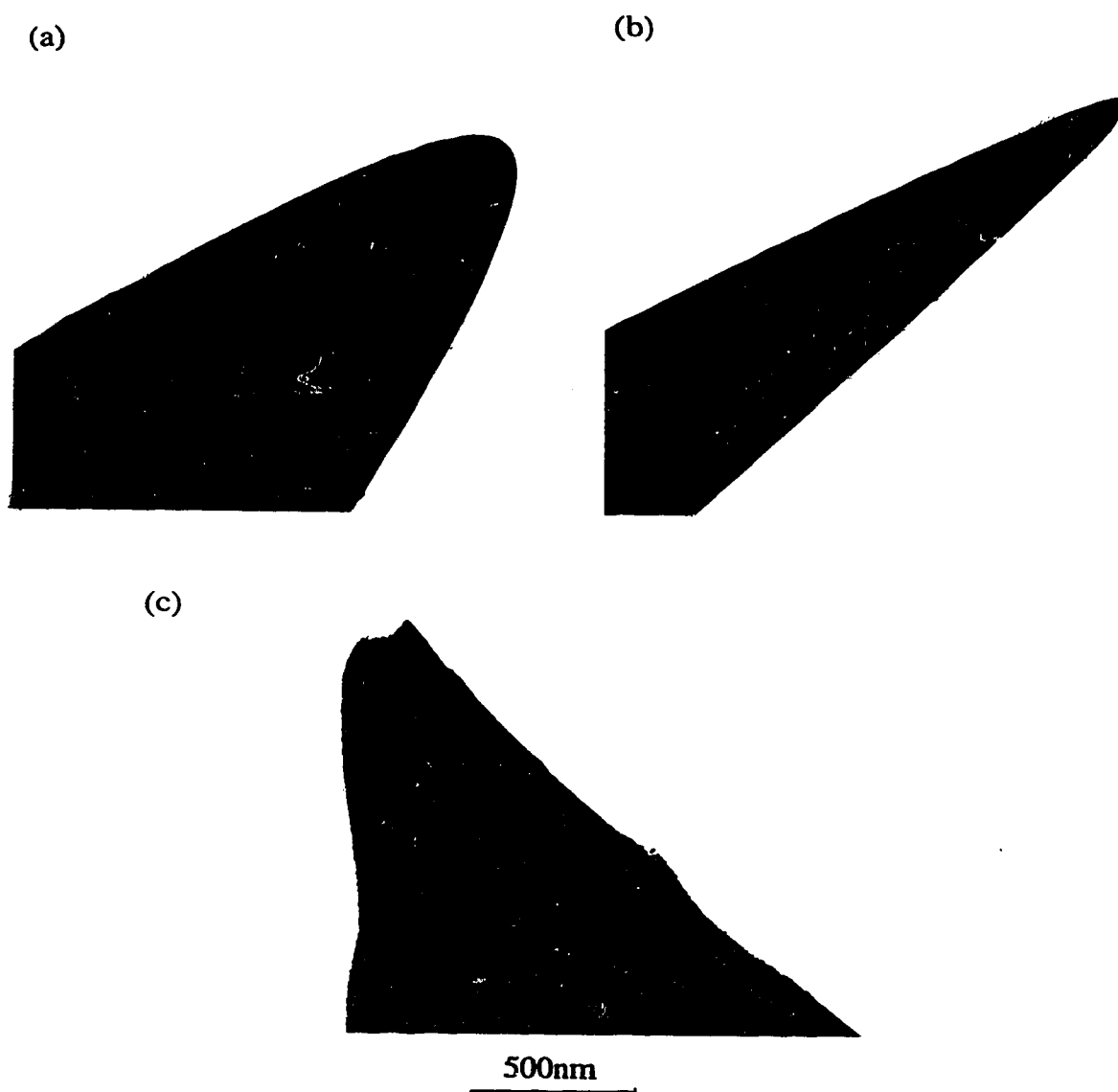
Fig. 4-7   TEM images of W tips prepared by a combination of electropolishing and ion milling. (a) Tip after electropolishing and prior to ion milling; (b) after ion milling for 40 min; (c) after ion milling for 3 hr.

84

600nm

400nm

200nm

100nm
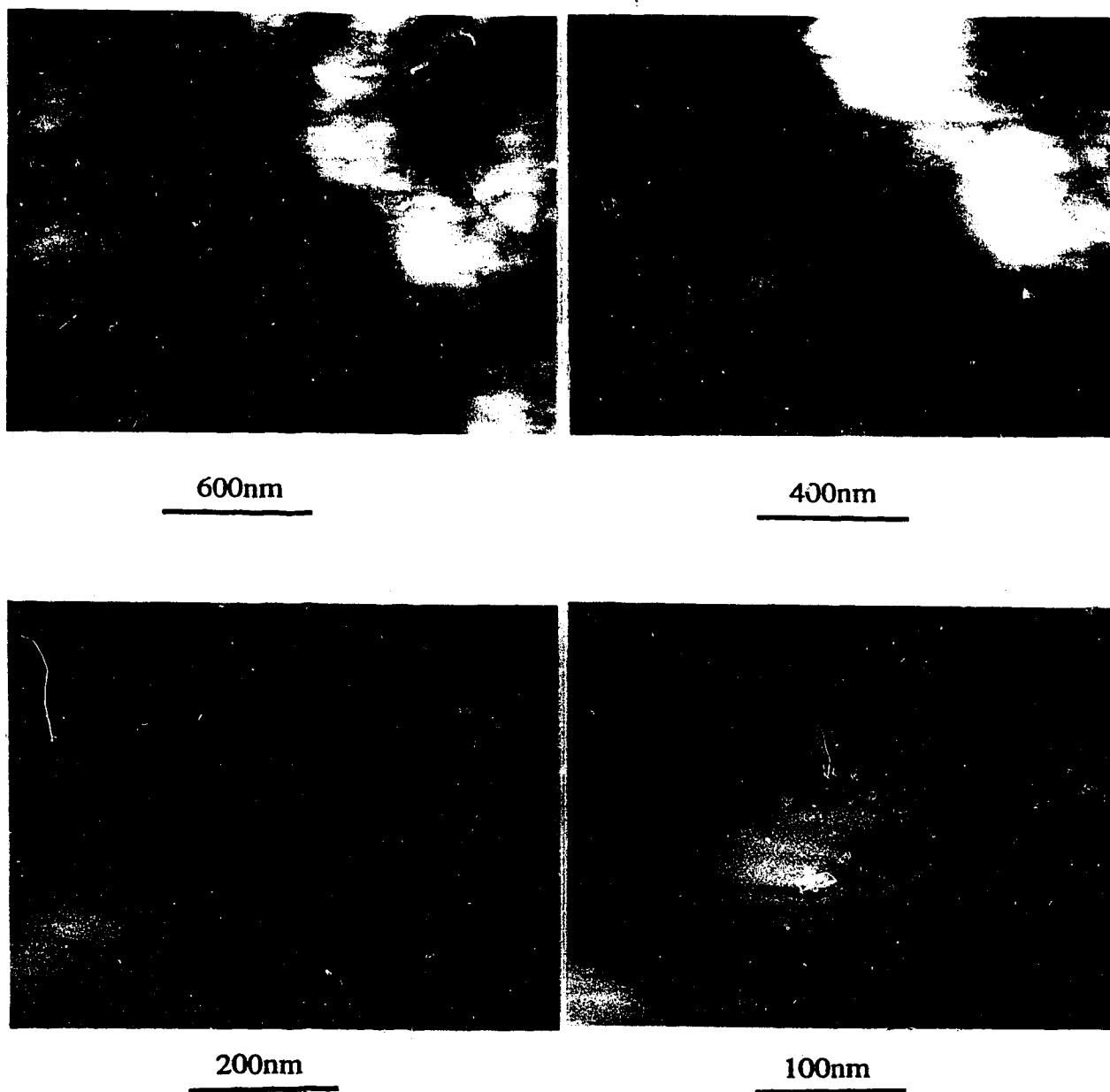
Fig. 4-8   STM images of Au/InP annealed at 400°C for 1h.

85

(a)

(b)

1.0μm
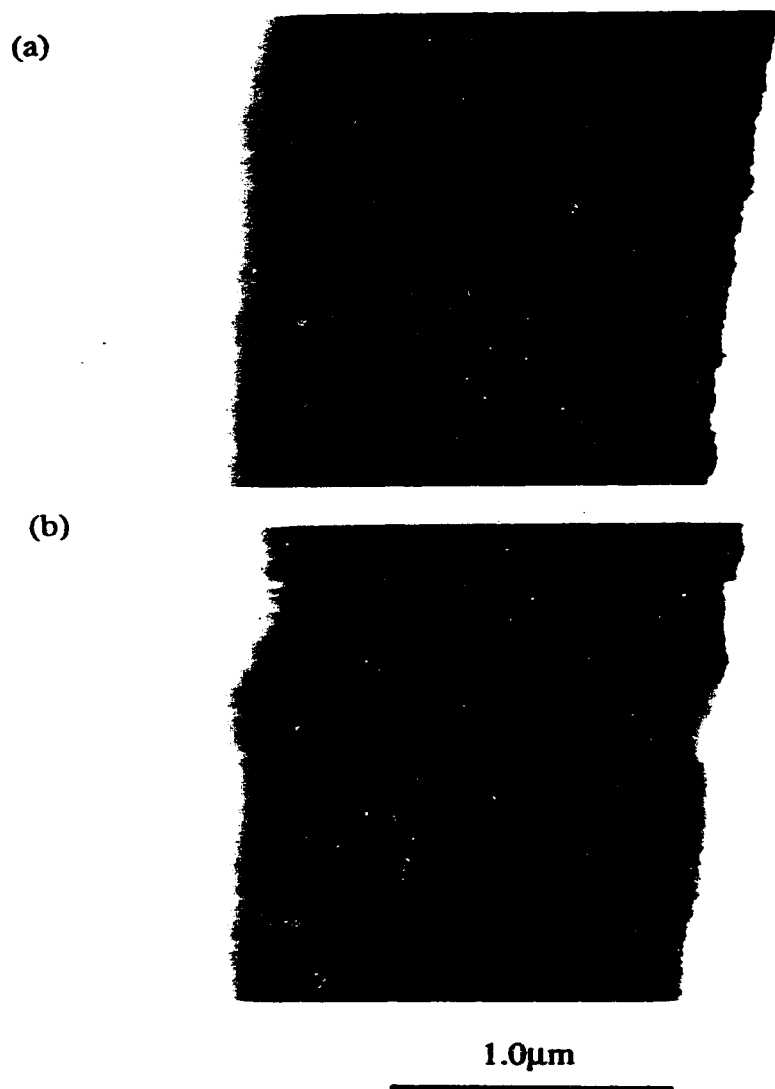
Fig. 4-9   STM images of the gold grating structure scanning from left to right with a
scan delay of 10mS/sample by an ion milled tip. (a) the first image; (b) the
sixth image.

(a)

(b)
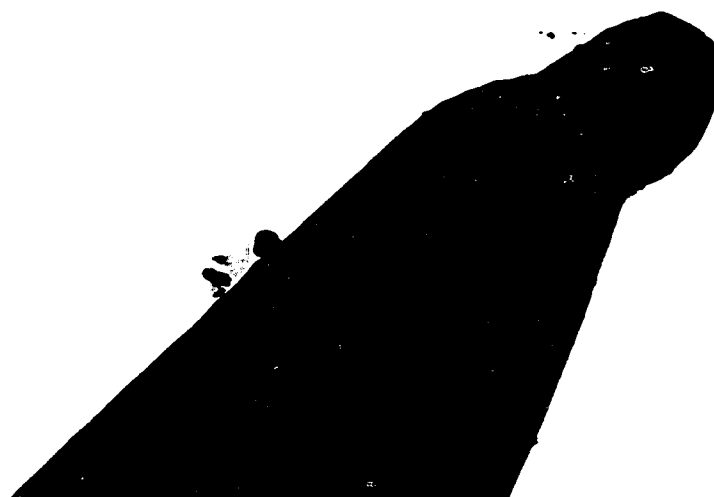
500nm

Fig. 4-10   TEM images of W tips after scanning the gold grating. (a) ion milled tip; (b)
electropolished tip.

(a)

Height (Angstroms)

6704.0

6041.2

5178.4

4315.6

3452.8

2590.1

1727.3

864.5

1.7

0.0   1451.1   6906.3   10359.4   13812.5   17265.6

Distance (Angstroms)

(b)

Height (Angstroms)

6704.0

5178.4

4315.6

3452.8

2590.1

1727.3

864.5

1.7

0.0   1421.9   6814.0   10765.6   13807.5   17104.4

Distance (Angstroms)
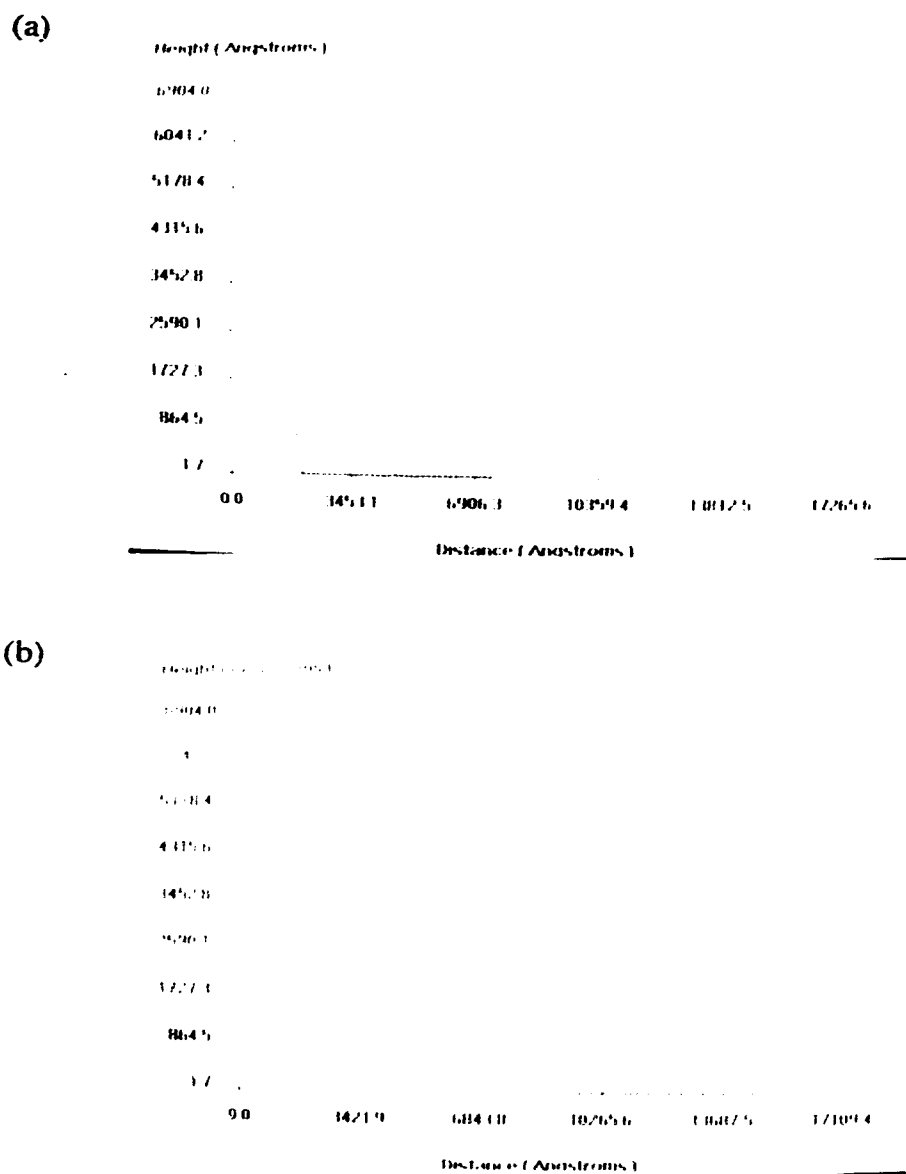
Fig. 4-11   STM line scans of gold grating with scan delay of 5 ms. (a) scan from right to left; (b) scan from left to right.

88

(a)

(b)
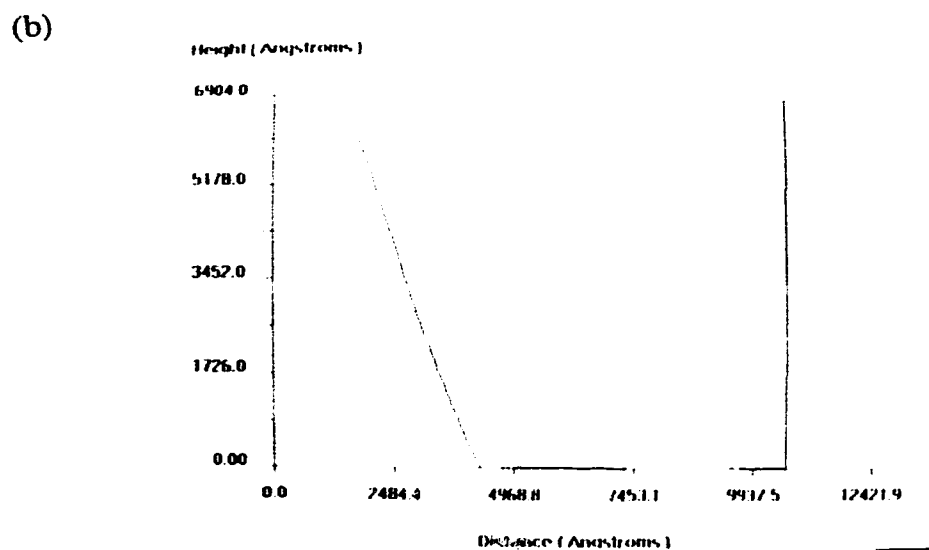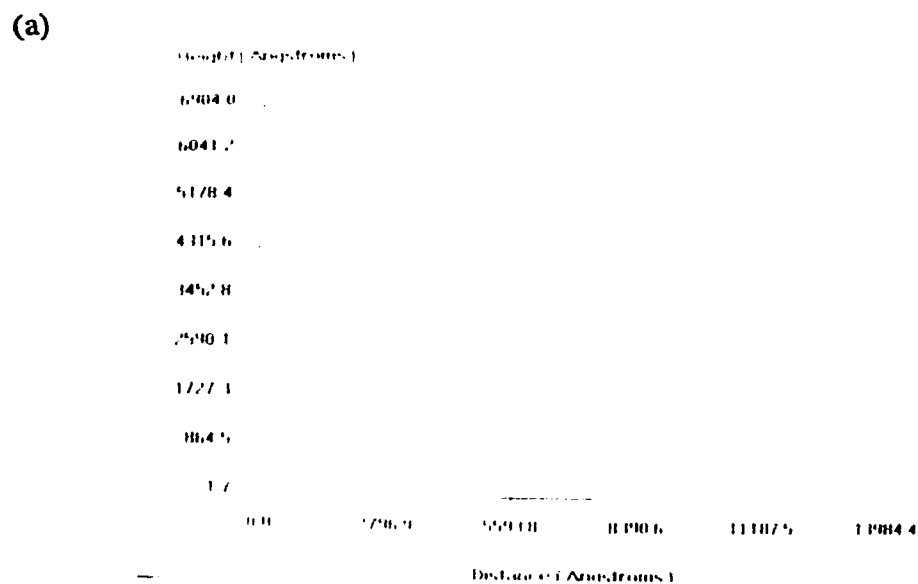
Fig. 4-12   STM line scans of gold grating with scan delay of 10 ms. (a) scan from right to left; (b) scan from left to right.

89

(a)

200nm

(b)

Si

Au

glue

200nm
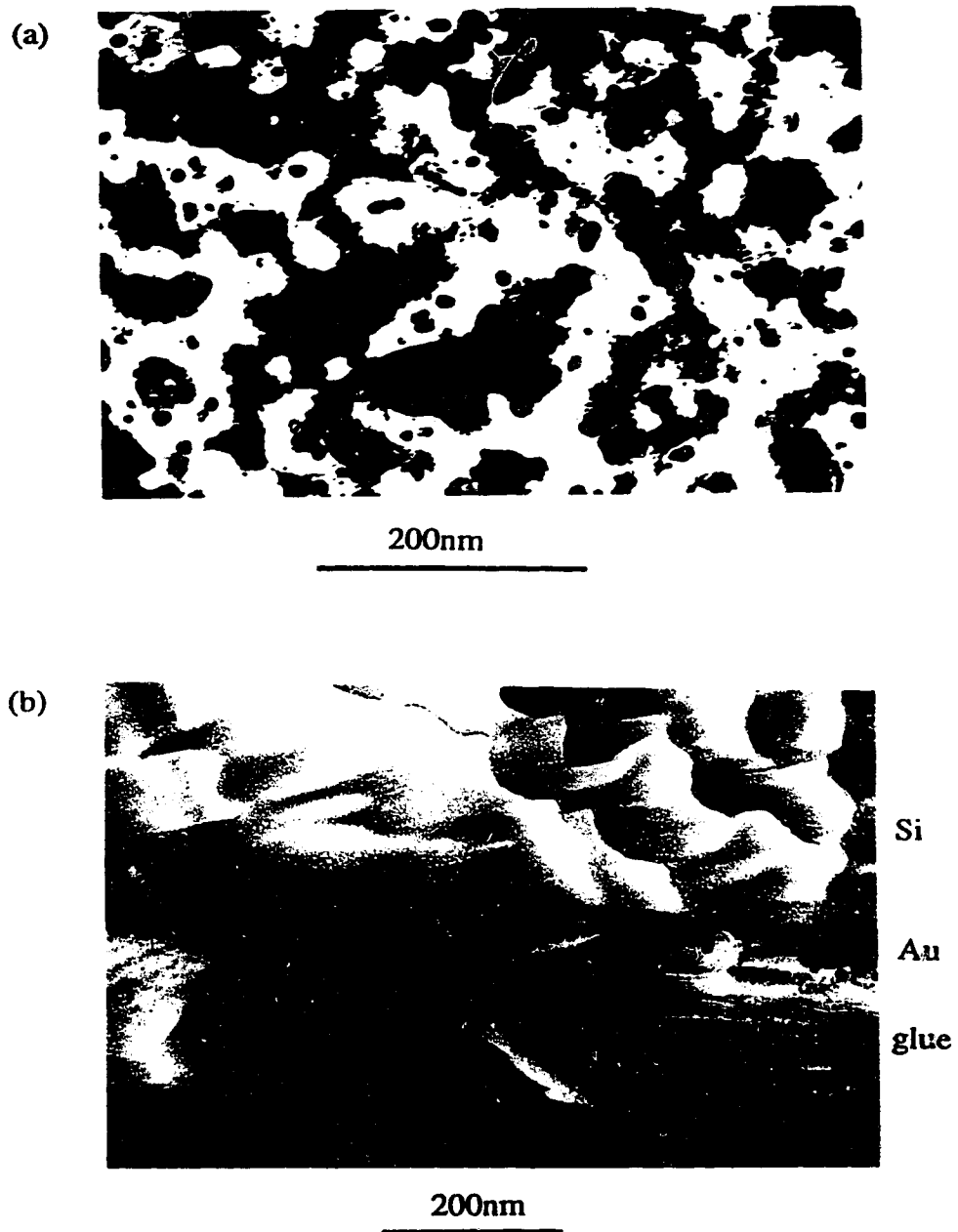
Fig. 4-13   TEM bright field images of Au film on <100> oriented Si. (a) plan view
image; (b) cross section image.

(a)
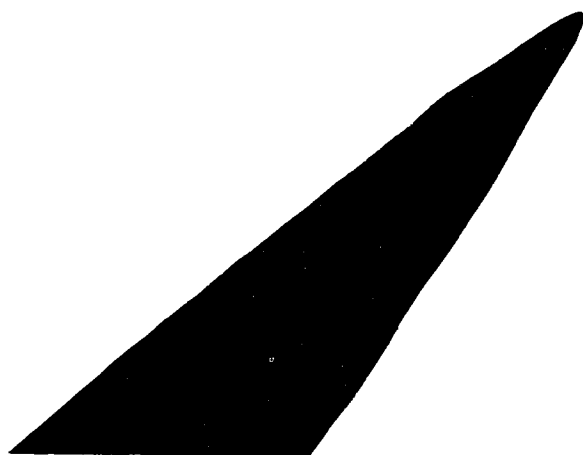
(b)
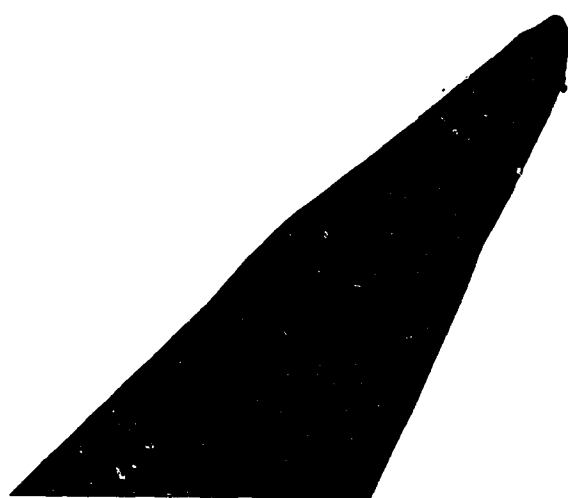
500nm

Fig. 4-14   TEM images of an ion milled tip (a) before and (b) after STM imaging of Au
films.

(a)
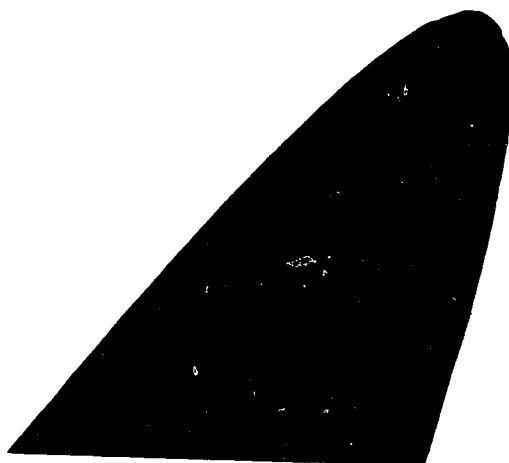
(b)

500nm

Fig. 4-15　TEM images of electropolished W tips (a) before and (b) after STM imaging of Au films.

(a)

(b)

100nm
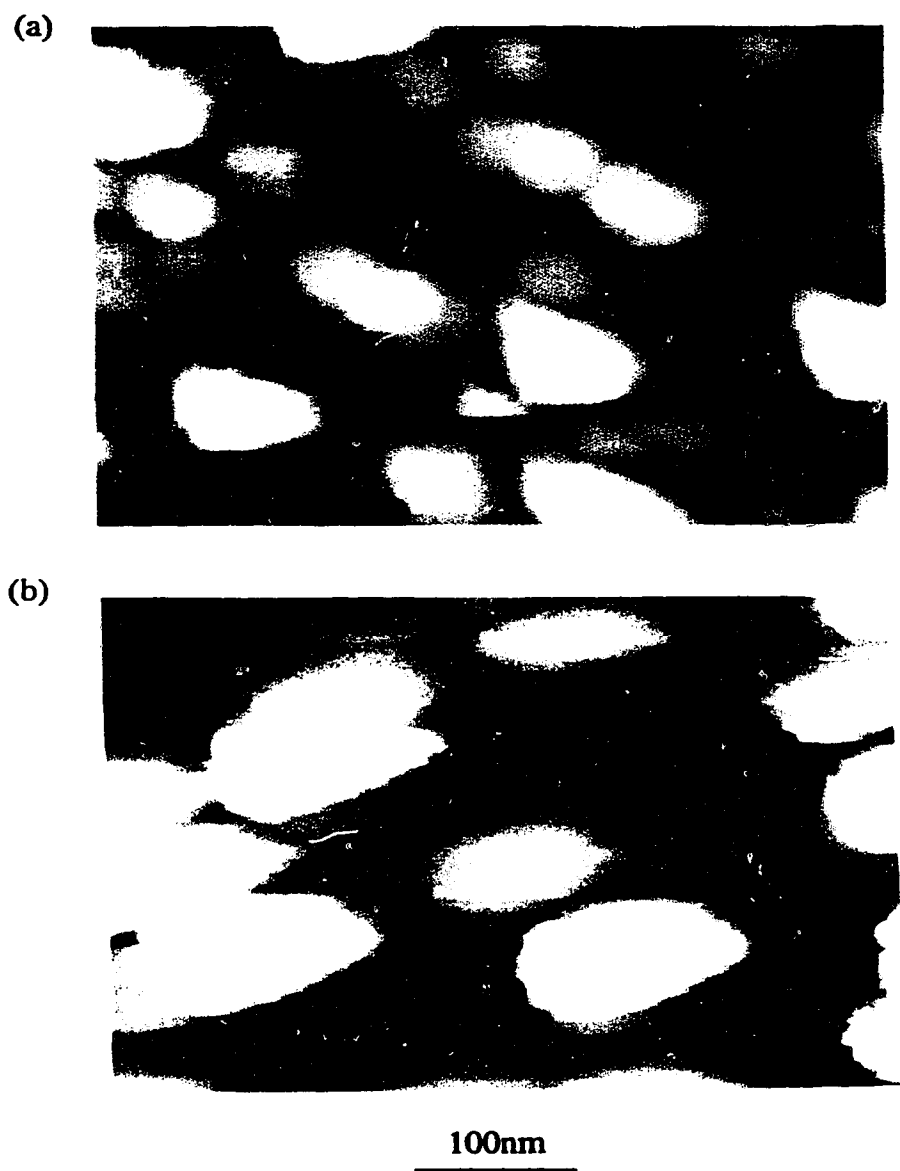
Fig. 4-16   STM images of Au films on <100> Si. (a) Image scanned with ion milled tip
in Fig. 4-14. (b) Image scanned with electropolished tip in Fig. 4-15.

93

500nm
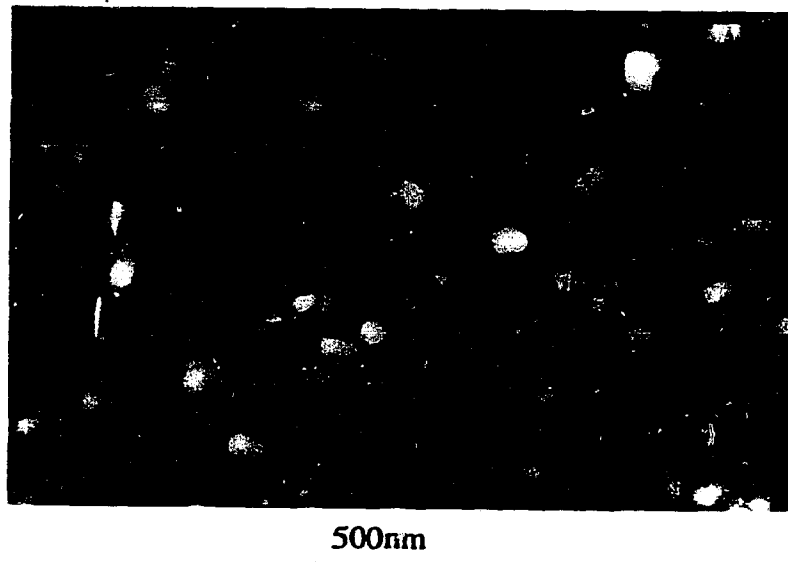
Fig. 4-17   AFM image of Au film on <100> Si.
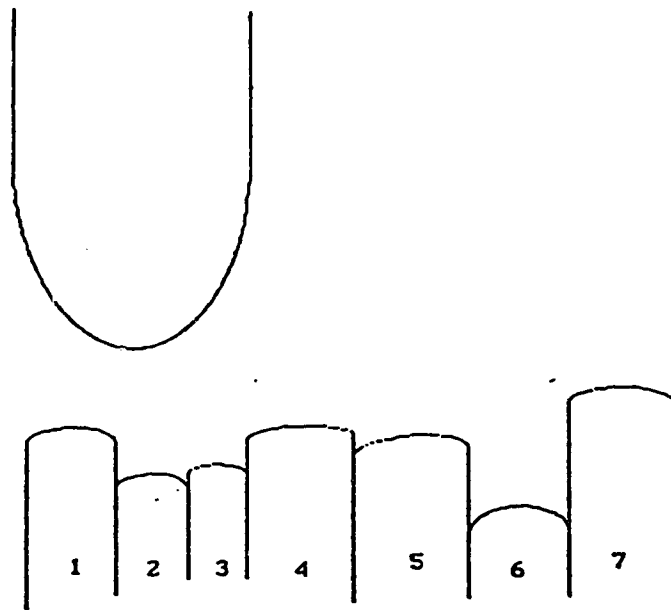
Fig. 4-18   Schematic diagram showing the effect of a broad tip on imaging of
polycrystalline films with a grain size smaller than the tip radius.

50nm
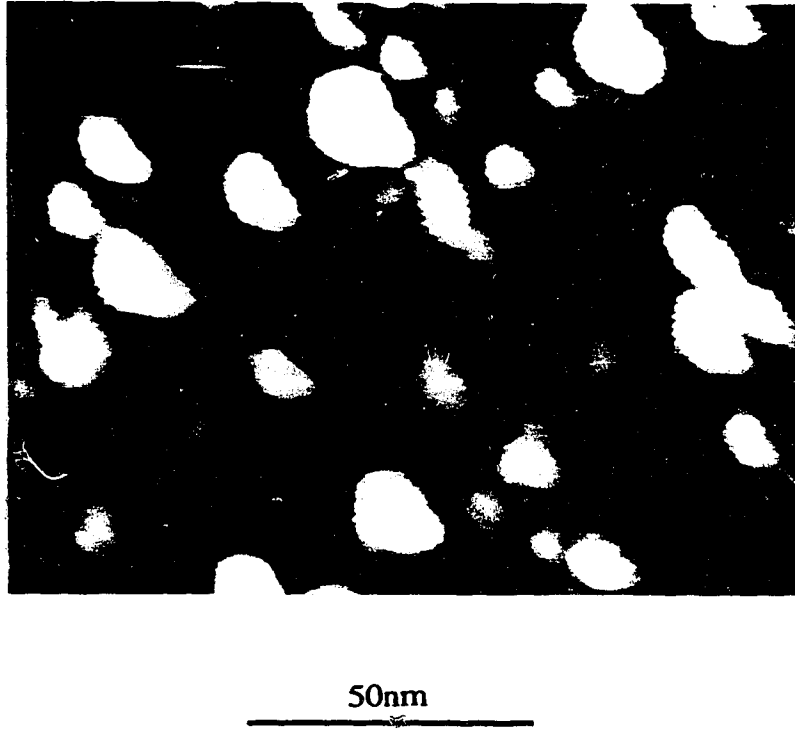
Fig. 4-19 STM image of Au on <100> Si same day after deposition scanned by Pt-Ir tip.
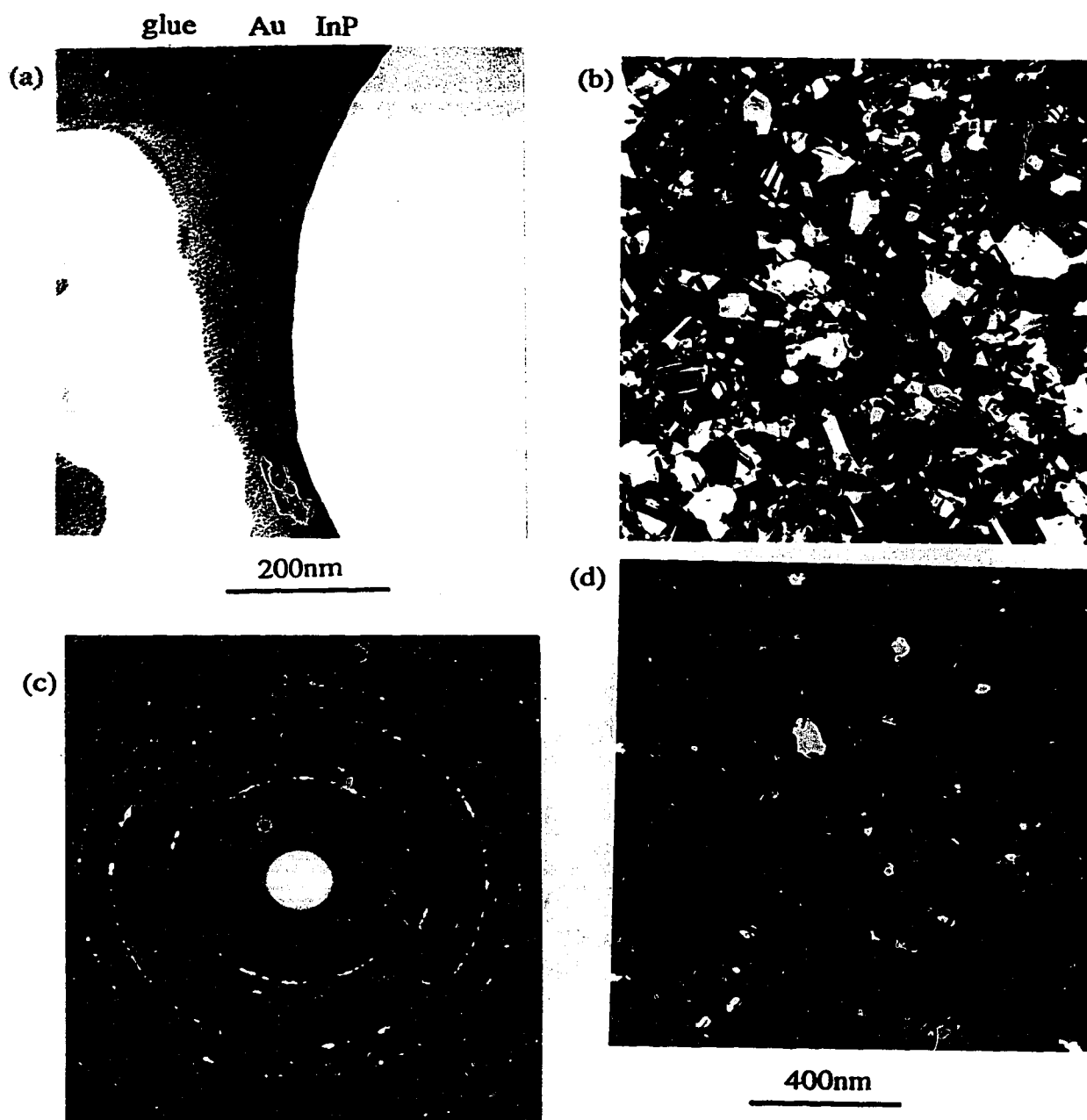
Fig. 4-20   TEM images of Au on InP as deposited sample. (a) cross section image; (b) plan view bright field image; (c) SAD pattern taken from (b); (d) dark field image taken from 220 reflection.

96

(a)

50nm

(b)
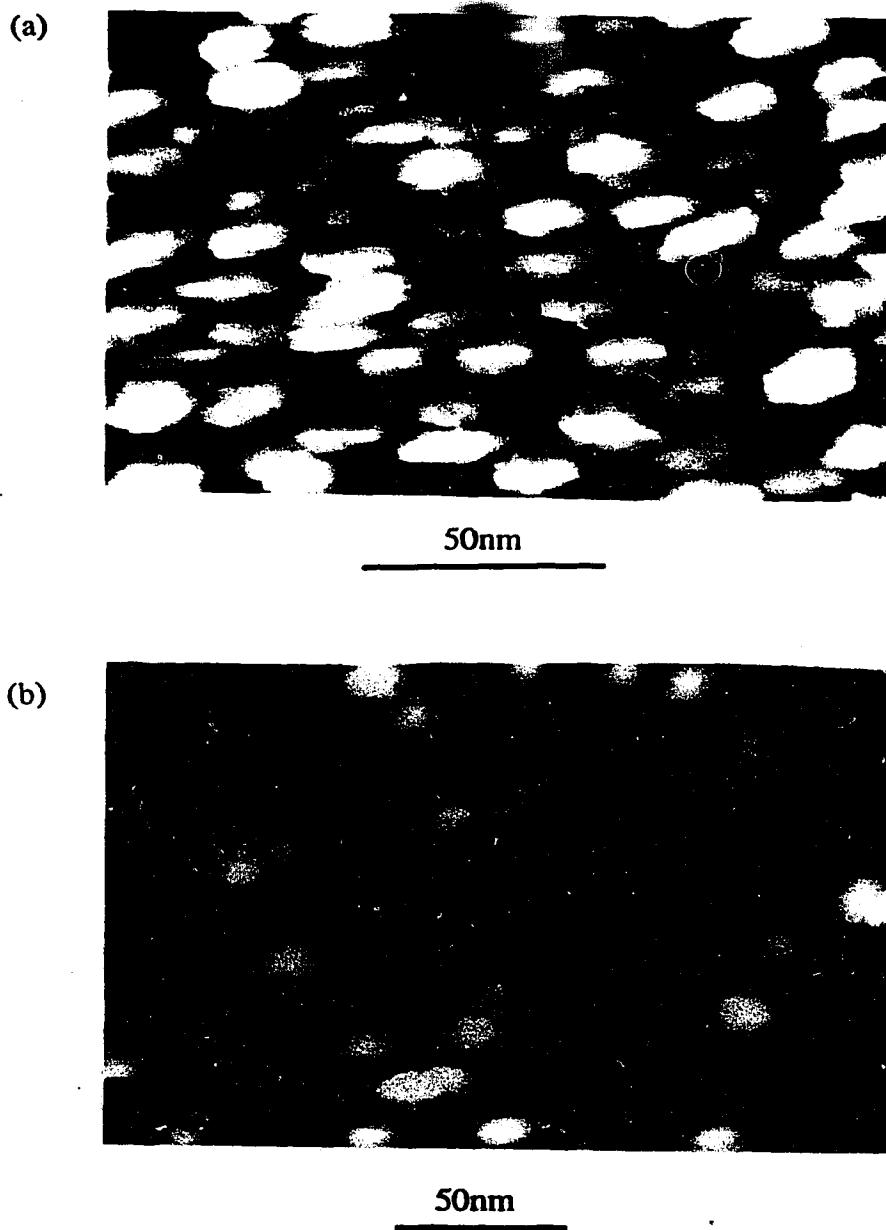
50nm

Fig. 4-21   STM image of Au on InP as deposited sample. (a) taken with ion milled tip;
(b) taken with Pt-Ir tip.

100nm

Fig. 4-22   STM image of Au on InP sample annealed at 320°C for 18h, showing tip artifact.

(a)

50nm

(b)
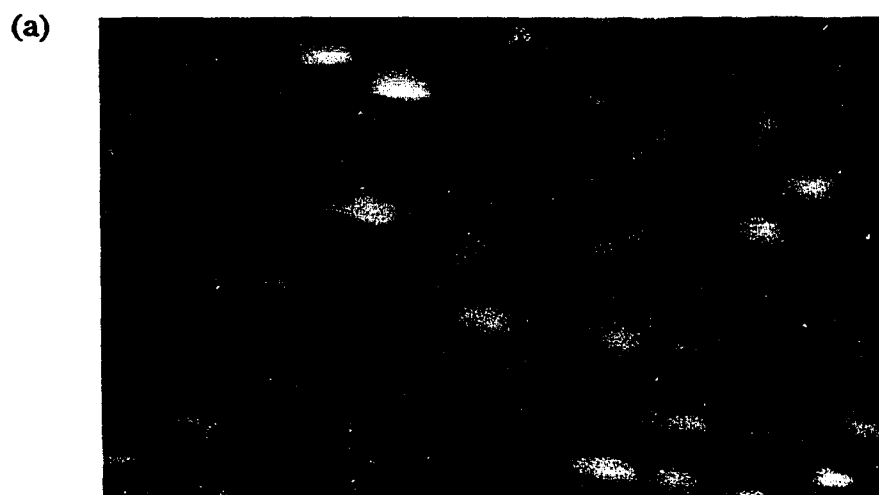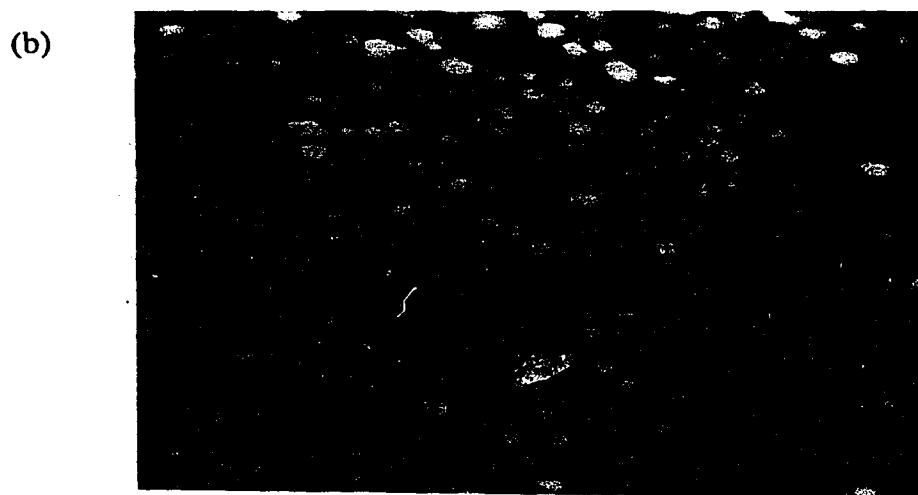
100nm

Fig. 4-23   STM images of Au on InP sample annealed at 175°C for 18h. (a) high
magnification; (b) low magnification.

99

(a)

100nm

(b)

200nm
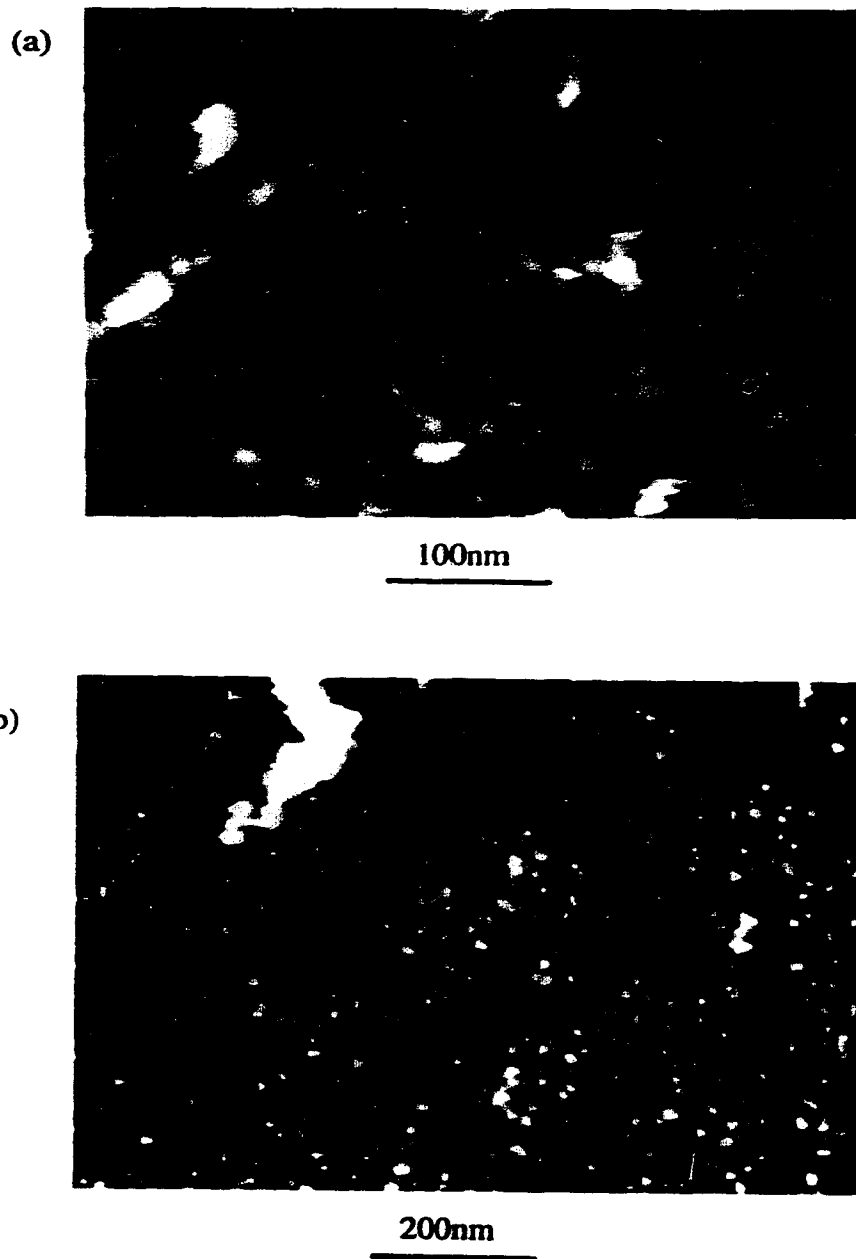
Fig. 4-24   STM images of Au on InP sample annealed at (a) 275°C for 18h; (b) 320°C
for 18h.

100

(a)

400nm

(b)

600nm

(c)
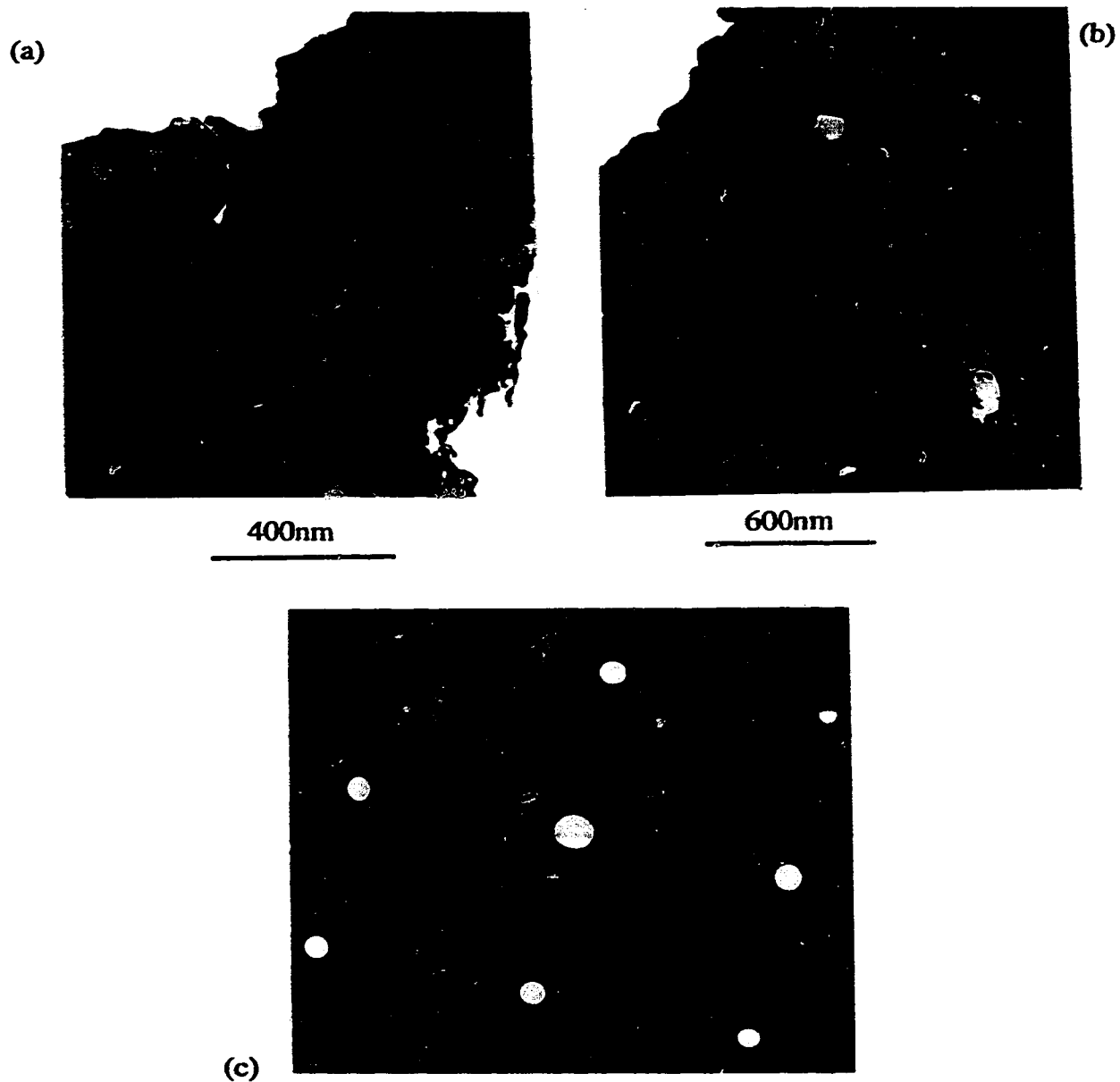
Fig. 4-25   TEM images of Au on InP samples annealed at 320°C for 65h. (a) taken from
the gold area; (b) taken from the pink area; (c) CBED pattern taken from (b);

101

$(1\underline{1}6)$

$(2\overline{2}4)$

$(\overline{1}32)$

(012)

$(1\overline{1}2)$

$(\overline{1}20)$

$(3\overline{5}2)$

$(3\overline{5}2)$

$(1\overline{2}0)$

$(\overline{1}1\overline{2})$

$(0\overline{1}2)$

$(\overline{2}2\overline{4})$

$(1\overline{3}2)$

$(\overline{1}\overline{1}6)$
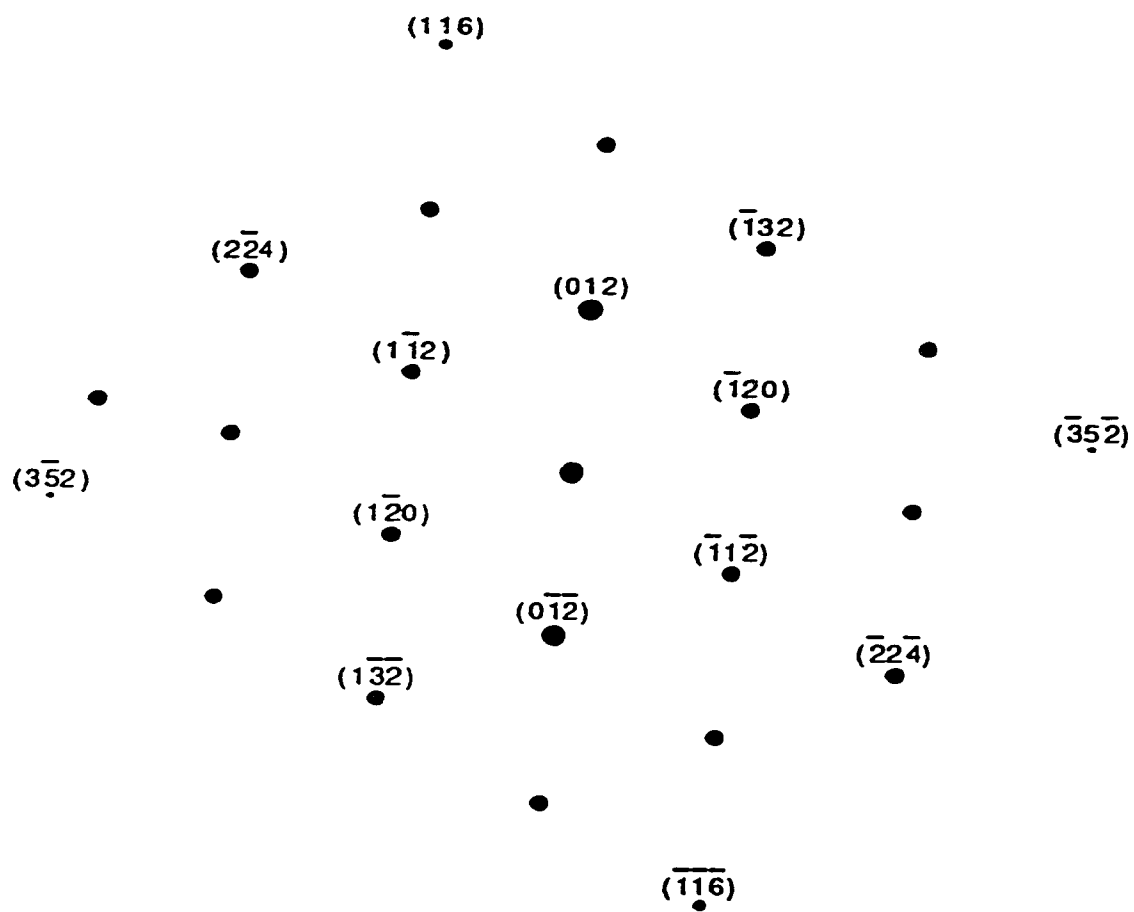
Au$_3$In

zone axis = $[42\overline{1}]$

Fig. 4-25   (d) indexed CBED pattern.

102
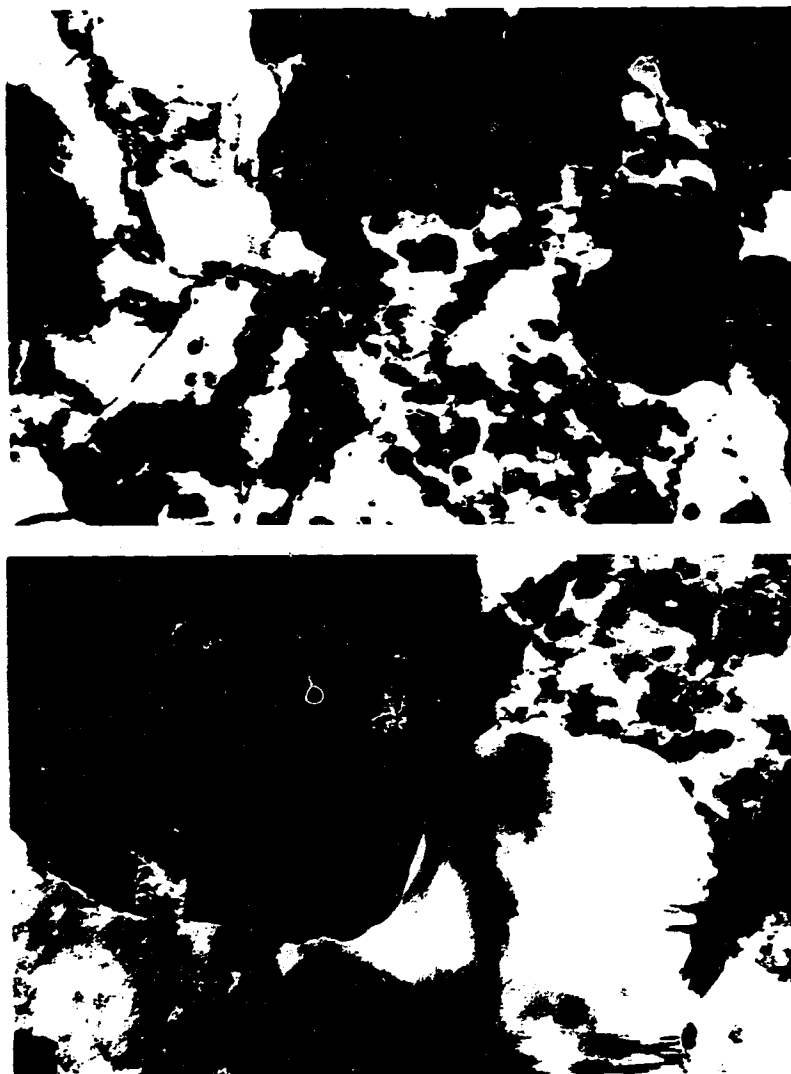
200nm

Fig. 4-26 TEM images of 450°C 1h sample taken at different locations.

103

100nm

Fig. 4-28   STM image taken from 450°C 1h sample.

105

(a)

(b)   (c)

500nm
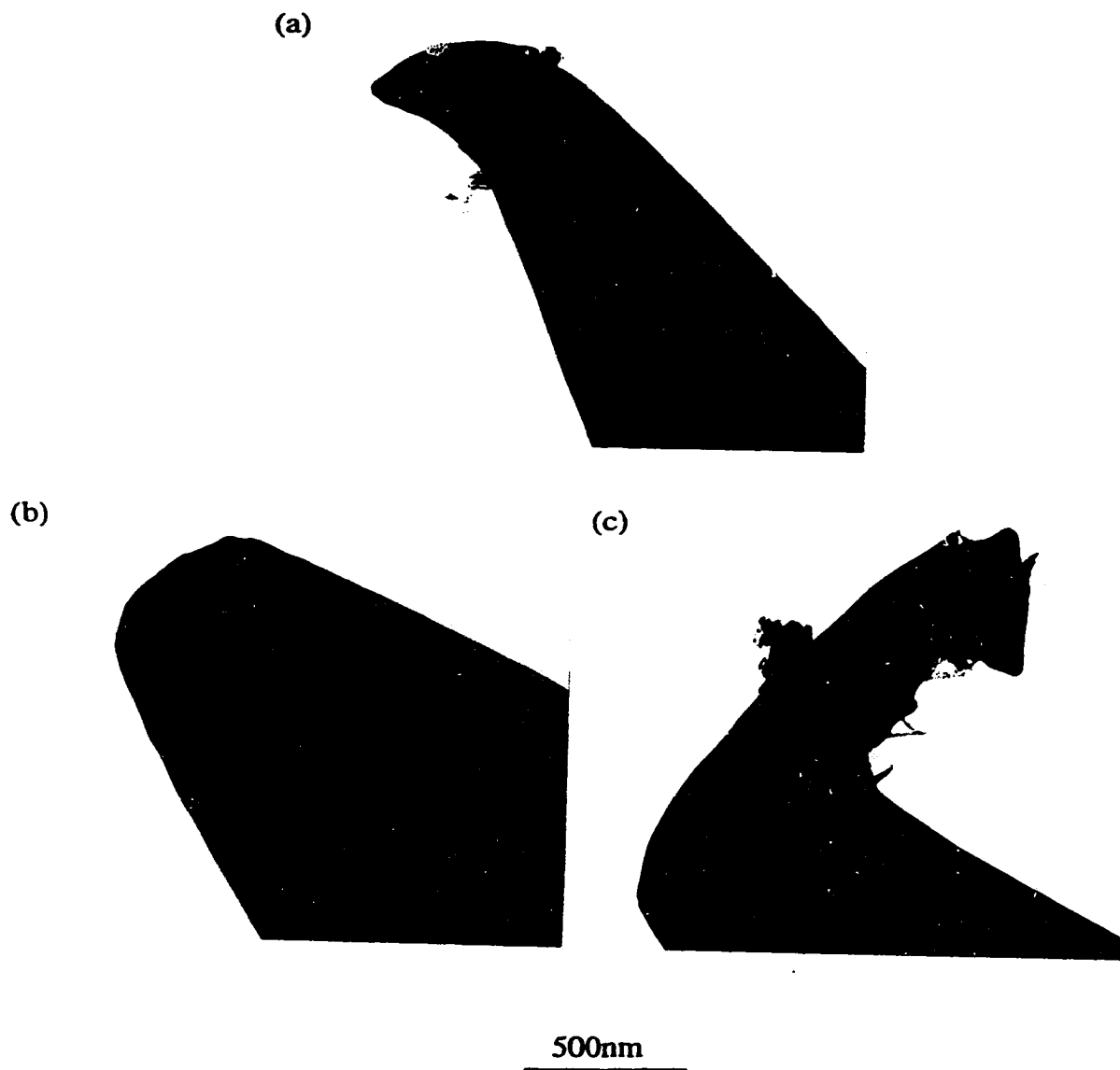
Fig. 4-29   TEM images of STM tips. (a) Ion milled W tip after scanning 10 images on
Au/Si(100) sample; (b) Electropolished W tip after crashing into sample;
(c) Ion milled W tip after crashing into sample.

106

CHAPTER 5. CONCLUSIONS AND RECOMMENDATIONS

5.1 Conclusions

In this research, two types of W tips have been fabricated. These two types of W tips, as well as the mechanically cut Pt-Ir tips were used for STM imaging on Au/Si (100) and Au/InP samples. The roles of both geometry and electronic states of the STM tips in imaging have been investigated. A number of conclusions can be made based on the experimental results.

1. By carefully controlling the parameters, dc downward electrochemical polishing can produce initial tips with radii on the order of 200-250 nm. Subsequent ion milling can substantially reduce the tip radius to ≈ 20 nm.

2. Apparent grain sizes appear to agree with theoretical calculations of finite-size tip distortion done by Keller [101] for the rougher surface Au/Si(100) samples, which were imaged seven days after deposition. Single atom tunneling can be used to interpret the smoother surfaces found in the as deposited Au/InP samples, and Au/Si(100) samples right after deposition.

3. In STM studies, the true surface topography is constantly distorted by the tip geometry (both the shape and the sharpness); this is referred to as tip artifacts. Artifacts include double images (caused by double tips), inaccurate topographic images (caused by blunt tips), and discontinuous images (caused by multiple tips). Here, another type of image artifact is reported due to the asymmetrical geometry of the tips, i.e., directional images.

107

4. The resolution of STM images is believed to be determined by the electronic states of both the tip and the sample, instead of only the electronic states of the tip.

5. Tip bending during STM imaging is due to both the sharpness of the tip and the roughness of the sample surface. Tip bending is more pronounced for higher aspect ratio tips.

6. In the study of the topography of Au on InP substrates, the Au grain size remains virtually unchanged while the film becomes porous due to coalescence during low temperature annealing (without phase change).

7. During higher temperature annealing of Au/InP samples (with phase change), localized phase transformation of the Au-In solid solution to Au_3In is determined by utilizing both TEM and STM.

5.2 Recommendations

Further investigations, using electropolished and ion milled W tips, on different samples, such as Pd/InP and Pt/InP, which are the other two inert metals suitable for STM study in air, are recommended. As is the case with Au, Pd and Pt are two important components in ohmic contacts to InP, and their topographic changes during annealing deserve a complete study.

PART 2

BALLISTIC ELECTRON EMISSION MICROSCOPY

CHAPTER 6. LITERATURE REVIEW

Traditionally, the schottky barrier measurement method relies on electrical probes, such as current-voltage or capacitance-voltage measurements, or on optical methods such as photoemission [132-134], which only yield spatially averaged results. However, the metal-semiconductor interface usually exhibits lateral heterogeneity due to microscopic defects, thus it is desirable to characterize the interface properties, such as interface barrier height, interface carrier transport and interface band structure, with high resolution.

BEEM, on the other hand, since its initial demonstration by Kaiser and Bell [13, 14], has been used to study the spacial variation of the Schottky barrier height with nanometer resolution, and direct imaging of subsurface interface.

6.1   Metal-Semiconductor Contacts

Generally, when a metal and a semiconductor are brought together, there exists an energy barrier for carriers (electrons or holes) in the metal layer to penetrate into the semiconductor due to the difference in the work functions between the metal and the semiconductor. The contacts can be divided into two types: Schottky barriers and ohmic contacts depending on their current-voltage characteristics. Theoretically, the Schottky barrier forms in the case where the semiconductor is n-type and the work function of the semiconductor is less than that of the metal, or the semiconductor is p-type and the work function of the semiconductor is larger than that of the metal (Fig 6-1a and d [130]). On the other hand, an ohmic contact forms when a metal and an n-type semiconductor, with the work function of the semiconductor larger than that of the metal, are joined or a metal and a p-type semiconductor, with the work function of the semiconductor less than that of the metal, are joined (Fig. 6-1b and c [130]). The potential barrier of the ohmic contact is almost nonexistent, so that the carriers can freely pass in either direction.

6.2   Ballistic Electron Spectroscopy

BEEM is a new technique, based on the STM, for study the electronic structure of metal-semiconductor interfaces (Fig. 6-2 [135]). As a negative tip-base bias voltage is applied, electrons tunnel from the tip to the sample as hot carriers. Provided that the thickness of the metal layer is less than the mean free path of the electron in that metal, many electrons travel ballistically across the metal layer toward the interface. For tunneling voltages less than the interface Schottky barrier height, none of the electrons reaching the interface will have an energy equal to or greater than the barrier height, so there will be no collector current. If the voltage is increased to a value larger than the barrier height, electrons which satisfy the total energy and momentum parallel to the interface can cross the interface into the semiconductor, and are measured as a BEEM current. Moreover, an n-type semiconductor is needed for the collection of the electrons. The location of the threshold in the spectrum is then defined as the interface Schottky barrier height (Fig. 6-3 [136]).

There exist four possible steps for electron transport from a tip via the metal to a semiconductor (Fig. 6-4[137]): tunneling from tip to metal, transport through the metal film with elastic and inelastic scattering, transmission across or reflection at the interface, and the impact ionization in the depletion layer of the semiconductor.

(1)   Tunneling from tip to metal

The electron injected into the metal by tunneling is treated by using a planar tunneling formalism [136, 138]. This description provides simple analytic expressions for the electron tunneling distribution.

According to the WKB (Wentzel-Kramers-Brillouin) approximation [136, 139], the tunneling probability $D(E_x)$ is

$$D(E_x) = \exp(-2 \int k_x dx) \tag{6-1}$$

Using a common approximation [136, 138],

$$D(E_x) \approx \exp\left[\frac{\sqrt{8m}}{\hbar} s\sqrt{E_F + \phi - E_x}\right]$$

(6-2)

where ϕ = V_b − eV/2 for a square barrier, V_b is the Schottky barrier, V is the bias voltage, m is the electron mass, s is the tip-to-sample distance, E_F is the Fermi energy, E_x and k_x are the energy and momentum component perpendicular to the interface, $\hbar$ is Planck's constant divided by 2π.

(2)   Electron transport through the metal layer

Electrons in the metal layer are treated as quasi-free electrons interacting with the crystal potential by elastic and inelastic scattering[140].

The ballistic mean free path λ_B is given as:

$1/\lambda_B = 1/\lambda_\sigma + 1/\lambda_e$

(6-3)

where λ_e is the mean free path of inelastic scattering accounting for electron-electron interaction which is energy dependent:

$\lambda_e \propto 1/(E - E_F)^2$

(6-4)

λ_σ is the mean free path of elastic scattering including electron-impurity scattering or quasielastic electron-phonon scattering, where the energy loss is not significant and is independent of the energy in the range of 1 and 6 eV.

λ_σ = constant

(6-5)

(3)   Transmission across the interface

As an electron reaches the interface of a barrier, conservation laws of total energy and momentum parallel to the interface have to be satisfied for the electron to be transmitted across the interface. In the case where the electron is incident at the interface at non-zero angles, as shown in Fig. 6-5 [136], conservation of momentum parallel to the interface (k_{tM} = k_{tS}) demands that $\vec{k}$ changes across the interface. If the angle of incidence is greater than some "critical angle" [141], the conservation law for k_t cannot be

satisfied, and the electron is reflected back at the interface. This critical angle can be expressed according to an isotropic free-electron approximation in the metal layer [136]:

$$\sin^2\theta_c = \frac{m_t}{m} \cdot \frac{eV - eV_b}{E_F + eV}$$

(6-6)

where m is the free-electron mass, m_t is the component of the effective mass in the semiconductor parallel to the interface, V is the bias voltage, V_b is the Schottky barrier of the interface, and θ_c is the critical angle.

The assumption that all electrons incident at the interface within the critical angle are collected is not suitable for an abrupt interface where quantum mechanical reflection occurs. For normally incident electrons, the transmission probability T(E, $\vec{k}$) [142] is

$$T(E, \vec{k}) = \frac{4k_{xM}k_{xS}}{\left(k_{xM} + k_{xS}\right)^2}$$

(6-7)

where k_{xM}, k_{xS} are the momentum components perpendicular to the interface in the metal layer and semiconductor layer, respectively.

(4)   Impact ionization in the semiconductor

Electrons entering the semiconductor may excite electron-hole pairs if their energy is sufficiently high (especially for high bias voltage BEEM). If the excitation takes place within the depletion zone, the e-h pair is separated, and contributes to the BEEM current.

By neglecting any variation in kinetic energy due to the electric field in the depletion zone, the mean-free path λ_{ii} for impact ionization is [143]:

$$\lambda_{ii} \propto \frac{\sqrt{E - E_F - eV_b}}{\left(E - E_F - eV_b - E_{th}\right)^2}$$

(6-8)

where E_{th} is the ionization threshold, which is on the order of the energy gap of the semiconductor. The probability for excitation of a secondary electron is approximated by [143]:

$$P_{ii} \propto 1 - \exp[-W / \lambda_{ii}(E)]$$

(6-9)

where W is the depletion width.

A Monte Carlo simulation [137, 144] utilizes this four-step model to trace the electron transport from the tip to the semiconductor. Eq. 6-2 is used to determine the tunneling distribution. In the metal film, Eqs. 6-3, 6-4, and 6-5 are used for calculating the inelastic and elastic scattering. At the interface, Eqs. 6-6 and 6-7 are used to determine whether the electron will cross the interface. Eqs. (6-8), (6-9) are used to decide if an additional electron contributing to the BEEM current is created by impact ionization.

For specific interfaces, simplified models can be derived from the four-step model.

6.2.1 Power Law

For BEEM measurement with low bias voltage, especially near the Schottky barrier height, impact ionization can be neglected. So the general expression for the BEEM current [145] is

$$I_c \propto \int_{-\infty}^{\infty} \int_{0}^{4\pi} F(E,V,T) \cdot D(E,V,\vec{u}) \cdot \exp[-d(\vec{u})/\lambda_B(E)] \cdot T(E,\vec{k}) \cdot d\Omega \cdot dE \qquad (6\text{-}10)$$

where $F(E, V, T)$ is the Fermi function of the tip electrons at temperature T, $d(\vec{u})$ is the electron path length through the metal film, $\vec{u}$ is the direction of the electron path length through the metal film, and $d\Omega$ is the solid-angle segment with direction $\vec{u}$.

At the interface, the energy and momentum parallel to the interface are conserved [145],

$$k_{xM} = \sqrt{2m(E - E_M^o)/\hbar^2 - k_t^2} \qquad (6\text{-}11)$$

$$k_{xS} = \sqrt{2m_S(E - E_S^o)/\hbar^2 - k_t^2} \qquad (6\text{-}12)$$

where m_S is the effective mass in the semiconductor, E_M^o and E_S^o are the conduction band minima in the metal and semiconductor, respectively, where $E_S^o = V_b$. Only electrons with $k_t \leq (2m_s (E - V_b))^{1/2}/\hbar$ can across the interface [145].

For an equal angular distribution of ballistic electrons in the metal, $d(\vec{u}) = d$, and $D(E,V, \vec{u})$ $d\Omega \propto D(E)$ k_t dk_t. $\lambda_B(E)$ and $D(E)$ can be considered as constants in the region of the threshold. Thus the collector current is simplified as:

$$I_c \propto \int_0^\infty F(E,V,T) \int_0^{\sqrt{2m_S(E-V_b)/\hbar^2}} T(E,k_t) \cdot k_t \cdot dk_t \cdot dE \qquad (6\text{-}13)$$

(1)   Square Law

If all electrons incident on the interface within critical angle are collected, that means transmission probability $T(E, k_t) = 1$, so the collector current is

$$I_c \propto \int_{V_b}^\infty F(E,V,T) \int_0^{\sqrt{2m_S(E-V_b)/\hbar^2}} k_t \cdot dk_t \cdot dE. \qquad (6\text{-}14)$$

For temperature T = 0K, $I_c \propto (V - V_b)^2$ [14].

(2).   5/2 - power Law

For the case of an abrupt interface, quantum mechanical reflection has to be considered, thus transmission probability $T(E,k_t)$ is not equal to 1. Close to the threshold $(E = eV_b)$, we have k_{xM} much larger than k_{xS},

$$T(E,k_t) \propto k_{xS} = \sqrt{2m_S(E-V_b)/\hbar^2 - k_t^2} \qquad (6\text{-}15)$$

$$I_c \propto \int_{V_b}^\infty F(E-V,T) \int_0^{\sqrt{2m_S(E-V_b)/\hbar^2}} \sqrt{2m_S(E-V_b)/\hbar^2 - k_t^2} \cdot k_t \cdot dk_t \cdot dE \qquad (6\text{-}16)$$

For temperature T = 0K, $I_c \propto (V - V_b)^{5/2}$ [145-147].

6.2.2   Kinematic Theory

For transmission through atomically abrupt and coherent interfaces (those with a common interface lattice for both materials, such as a reacted interface), it is possible to calculate the BEEM spectra. The assumptions, such as free electron and effective mass

115

approximations are no longer suitable. However, the impact ionization can still be neglected, so the collector current is equal to the integral of the electron distribution incident on the interface times the probability that an electron in each state will be transmitted across the interface. BEEM measurements on the coherent interface are sensitive to the details of the band structures of both the substrates and the overlayers. If there is no state in the substrate with the same E and $\bar{k}$ as in the overlayer, the transmission probability T will be zero. These kinematic constraints depend only upon the band structures of the two materials and the Schottky barrier height of the interface, determining which states might possibly contribute to electron transmission across the interface [148, 149]. Thus the interface transmission probability is calculated for each individual system.

6.3   Ballistic Hole Spectroscopy

The differences between ballistic electron spectroscopy and ballistic hole spectroscopy are that a p-type semiconductor is necessary as a collector to probe the valence band structure in ballistic hole spectroscopy, and the tip is positively biased. The tunneling process can be treated in terms of electron tunneling from the base to the tip, creating a ballistic hole distribution at the metal base. Since the tunneling is strictly by electrons, the energy and angular distribution of the ballistic holes at the metal layer are thus peaked towards the base Fermi level (Fig. 6-6 [150]). This peaking of the hole distribution toward the base Fermi level results in an asymmetry between the ballistic electron and hole spectroscopies. In ballistic electron spectroscopy, the portion of the electron distribution collected as BEEM current is toward the higher energies, where the distribution is maximum. In the case of holes, the least energetic holes are collected at the tail of the distribution.

Despite these differences, the behavior of the spectra threshold is the same as for ballistic electron spectrocopy. As a positive voltage is applied to the tip, ballistic holes

are created at the metal layer. Collector current is zero until the voltage exceeds the barrier height.

Utilizing both ballistic electron and ballistic hole spectroscopy, a complete description of the interface of both conduction band and valence band Schottky barrier heights can be obtained.

6.4   Instrumentation

The main idea of BEEM is to utilize the STM. BEEM employs an STM tip to inject ballistic electrons into a sample. In general, the sample consists of two layers with an interface of interest. BEEM operates as a three-electrode system, with electrical contact to each layer of the sample surface (Fig. 6-2). The metal base layer serves as a biasing electrode, and the semiconductor functions as a collector of the ballistic electron or hole current.

Because of the small collector currents being measured, it is necessary to use a high gain, low noise current preamplifier which has an inherent input noise of $100 \text{nV/Hz}_z^{1/2}$ across a metal-semiconductor diode resistance R_o. R_o has to be large enough for an adequate signal to noise ratio [136]. In the thermionic emission approximation [151], the diode resistance R_o at zero bias is expressed as

$$R_o = \frac{k}{eA^*Ta} \exp(eV_b/kT) \tag{6-17}$$

where A^* is the Richardson constant, k is Boltzmann's constant, a is the diode junction area, V_b is the Schottky barrier height and T is the absolute temperature. The impedance can be increased by either reducing the interface area or lowering the temperature. The dependence of the lowest measurable barrier height on temperature is plotted in Fig. 6-7 [136] for the diode area $a = 0.1 \text{ cm}^2$. At room temperature, a Schottky barrier height of at least 0.75 eV is necessary for measurable collector current.

117

For this reason, the metal layer is always fabricated as a two-lobed pattern, with one lobe used as the contact and the other used as the tunnel area (Fig. 6-8 [136]).

According to eq. 6-17, lowering the temperature is more effective in increasing R_O than reducing the diode area. Operation at low temperature has been accomplished by direct immersion of the STM head in liquid nitrigen (77K), with the entire BEEM apparatus enclosed in a nitrogen-purged glove box [152]. The glove box also serves to shield the apparatus from light since photocurrents generated by normal laboratory lighting can be orders of magnitude larger than currents collected from tunneling electrons.

6.5   Application

BEEM measurement of Schottky barrier height and interfacial phenomena is a very new technique. Most of the applications have been to the stable interfaces, such as Au/Si, Au/GaAs, silicide/Si and metal/GaP.

6.5.1   Au/Si and Au/GaAs

(1)   BEEM Spectroscopy

The simpe application of BEEM is to the Au /n-type Si(100) interface [13, 14]. Au/Si is known to provide high quality interfaces and reproducible barrier heights. The I_c - V spectra yields Schottky barrier heights ranging from 0.75 eV to 0.82 eV from many individual samples. The agreement of the experimental spectra and the square law theory verifies the assumptions made in the theoretical part.

In contrast to the Au/n-type Si (100) interface, the Au/n-type GaAs (100) interface is considerably more complex [13, 14]. GaAs has a direct conduction band minimum at the zone center and two high indirect minima at the L and X points of the Brillouin zone, while Si has only a single conduction band minimum along the [100] direction. As a result, Au/GaAs spectra display multiple thresholds of 0.89, 1.18 and

118

1.36 eV. The first threshold value is the Schottky barrier energy for Au/GaAs [153]. The difference between the upper thresholds and the lower one, 0.29 eV and 0.47 eV, count for the separation between the direct minimum and the satellite minima at the L and X points, respectively[154]. These thresholds are therefore assigned to ballistic electron injection into the Γ, L and X minima, respectively. The multiple threshold can be seen more clearly in the derivative spectra dI_c/dV vs V, in which they appear as steps. The data can also be drawn as $I_c^{1/2}$ - V [135, 155]. Several distinct gradients can be seen, which again indicate the presence of multiple barrier thresholds, and give thresholds of 0.82, 1.08 and 1.23 eV.

A variation in Schottky barrier height over the range of 0.8 to 1.0 eV is also observed at different locations on many Au/GaAs sample [136]. This wide range of barrier heights reflects interface heterogeneity, which can be seen more visibly in the BEEM imaging technique.

(2) BEEM Imaging

BEEM imaging is accomplished while scanning the STM tip over the surface of the sample at an applied tip voltage in excess of the SB height. The collector current is measured as the tip position, resulting in a collector current image of the interface.

BEEM imaging of Au/Si (100) interfaces shows a high degree of homogeneity for the interface electronic properties [136, 156]. BEEM current is very uniform across the scan area.

Unlike the Au/Si (100) system, a large spatial variation in BEEM current is observed on the Au/Si (111) interface prepared by an HF substrate cleaning procedure, while there is no BEEM current detected for the same system prepared by a UHV cleaned Si surface [157]. BEEM measurement of an HF cleaned interface shows that the BEEM current reaches a maximum and then drops to a lower value after the bias voltage is swept up to 3-4eV. This process is irreversible, and the subsequent BEEM image shows a dark hole where the tip was located. The BEEM current is thus believed to depend strongly on

interdiffusion of the Au and Si at the interface. The HF treated sample has a barrier preventing interdiffusion. The ballistic electron current at higher bias can penetrate this barrier layer and enhance the interdiffusion of Au and Si at the interface (Fig. 6-9 [158]). The Schottky barrier, on the other hand, does not show any dependence on the interface layer.

In order to determine the relationship between the topographic image and the BEEM image, Lee et al. [159] ran an experiment on a gold surface with a large step, however, the corresponding BEEM image shows no dependence on the relative gradient of the Au surface with respect to the Si interface. The observed contrast of the BEEM image is believed to be due to inelastic scattering at the interface by defects formed during the sample preparation.

The BEEM image of a Au/GaAs (100) interface shows an extreme level of heterogeneity [156, 160]. The dramatic spatial variation in the ballistic electron current is too great to be explained by thickness variation. BEEM images of the Au/GaAs (100) interfaces prepared without air exposure on melt-grown and MBE-grown substrates exhibit the same heterogeneous structure [156]. These observations indicate that the Au/GaAs (100) interface defect structure is not simply the result of substrate surface contamination, such as oxide, and substrate bulk properties.

The local interfacial band structure variation may result from variations in interfacial strain [154] or diffusion-induced nonstoichiometry [153]. GaAs is known to dissociate at the Au/GaAs interface, because Ga is soluble in Au and tends to migrate to the Au surface, while As is insoluble and remains at the interface in the form of islands [161, 162]. The dark areas of the BEEM image are believed to result from the inelastic scattering of ballistic electrons at the interfacial islands of As, and the interfacial heterogeneity is due to the diffusion-induced nonstoichoimetry in the form of As-rich precipitates at the interface [160].

Further studies have been carried out at the Au/GaAs(100) interface by interdepositing a thin AlAs layer as a diffusion barrier [160]. The homogeneous BEEM image of the Au/AlAs/GaAs heterostructure further supports the diffusion mechanism.

Moreover, photoemission measurements also indicate that the amount of Ga on the Au surface of the Au/AlAs/GaAs is greatly decreased [163].

6.5.2 Metal/GaP

Metal dependence on Schottky barrier height for n-type GaP(110) interfaces has been studied by several groups [137, 145-147], with various film thickness. The 5/2 power law was reported to fit the BEEM spectra. 1.2nm thickness Au and Mg layers show smaller Schottky barriers than 5nm films, demonstrating that the Schottky barrier formation process has not been completed when the overlayer metallizes, which is consistent with photoemission studies [164].

The decreasing of I_c with increasing V above 3eV in the 5nm Mg films can be explained by energy dependent inelastic scattering; the higher the bias voltage, the more the inelastic scattering, and the lower the collector current. For Au and thin Mg films, where the inelastic scattering probability is lower, the energy losses are much less, and a second threshold for the BEEM current at a bias voltage of 4eV is observed, due to to the onset of impact ionization [137].

In addition, the ratio of I_c/ I_t is on the order of 10^{-2} for the noble metals with film thickness of 12-20nm, while it is on the order of 10^{-4} for a 3.3nm thick Ni film in the study of various metals (Au, Ag, Cu, Mg, Ni) on GaP(110) carried out by Prietsch and Ludeke [145]. The Ni 3d excitations, which reduce the mean free path of the ballistic electrons inside the Ni film, are believed to be responsible for the extremely low BEEM current.

Contrary to Au/Si (111) and Au/GaAs interfaces, an exact spatial dependence of the low collector current in the BEEM image to the surface topography was observed for the metal/GaP interfaces, especially for the Mg/GaP system [137, 146]. The principle contrast of BEEM images of these systems is thus due to the topographic surface features of the metal overlayer.

121

6.5.3 Silicides/Si

Disilicide-Si interfaces such as $CoSi_2/Si$ and $NiSi_2/Si$ are ideal metal-semiconductor systems for BEEM study because of their atomically abrupt and structurally perfect interfaces resulting from the matched lattice [165-167]. Calculations of $CoSi_2$ band structure indicate an energy gap (1.4 eV above E_F) in the $CoSi_2$ at the energy and parallel momentum k_t corresponding to the conduction band minimum in Si(111) [168]. According to the energy and parallel momentum conservation law, there will not be any ballistic electron transmission across the $CoSi_2$ / Si(111) interface for some energy range above the Schottky barrier.

Stiles and Hamann [148] have performed such a transport kinematic calculation of the $CoSi_2$ and Si band structure. Fig. 6-10 shows the distribution of states in both materials in terms of their energy and parallel momentum k_t in the interface Brillouin zone. At an energy just above the Schottky barrier height, there are no available states in the $CoSi_2$ having the same phase space as in the Si conduction band minimum, so that all of the electrons incident on the interface from the $CoSi_2$ cannot transmit across the interface. As the energy increases, the available states of both materials increases. At about 0.2 eV above the threshold, there are states in both materials.

Kaiser et al [169] have studied the $CoSi_2$/n-type Si interface with low temperature BEEM and yielded a Schottky barrier height of 0.85 eV. Photoresponse and other measurements at 77K yielded a spatially averaged threshold value of 0.67eV [170, 171]. The shift in transmission threshold from the Schottky barrier value of 0.67 eV to 0.85 eV of BEEM measurement is in good agreement with the theoretical calculations.

$NiSi_2$, on the other hand, has two distinct orientations possible on Si(111): type A, which is in perfect registry with the underlying Si lattice and type B, which is rotated $180°$ about the (111) direction. Schottky barriers of type A and type B are 0.65 and 0.79 eV, respectively [172]. These two orientations can be easily detected by the BEEM imaging technique, where the contrast in the BEEM image of the mixed epitaxy of type A

and type B sample is evident due to the shift in Schottky barrier of type A and B NiSi$_2$ grains [173].

that the material involved has been removed because of copyright restrictions

Fig. 6-1   Band diagram of the Schottky barrier at a metal-semiconductor interface
            [130].

124

that the material involved has been removed because of copyright restrictions

Fig. 6-2   A schematic circuit diagram of BEEM [135].

125

Fig. 6-3   Energy diagram for BEEM of a metal-semiconductor Schottky barrier system
with (a) applied tunneling voltage of zero; (b) applied tunneling voltage in
excess of the barrier height. (c) Corresponding theoretical BEEM spectrum
[136].

that the material involved has been removed because of copyright restrictions

Fig. 6-4   Schematic diagram of electron transport from the tip to semiconductor in

a typical BEEM experiment [137]. The shadowed area represents the energy

distribution of the tunneling electron. The transport processes are shown by

the numbers. (1) ballistic electron transport; (2) inelastic scattering; (3) elastic

scattering; (4) reflection at interface; (5) impact ionization within the depletion

layer in the semiconductor.

that the material involved has been removed because of copyright restrictions

Fig. 6-5   Schematic diagram of an electron incident on a potential step with an initial

energy in excess of the step height [136].

that the material involved has been removed because of copyright restrictions

Fig. 6-6   Energy diagram of (a) ballistic electron and (b) ballistic hole spectroscopies
[150].

Fig. 6-7   Minimum measurable Schottky barrier height versus temperature calculated from Eq. (6-17) for n-Si (100). The criterion for measurement by BEEM is R_o = 100kΩ. For the calculation, $A^* = 252A/K^2cm^2$ and the diode area is 0.1 cm^2 [136].

Fig. 6-8   BEEM sample mounting scheme [136].

130

that the material involved has been removed because of copyright restrictions

Fig. 6-9   Schematic drawing of the Au/Si interface model [158]. (a) shows the scattering by the impurity layer at Au/Si interface; (b) depicts the strong scattering in the intermixed Au-Si layer; (c) shows the results of the high bias voltage modification.

131

that the material involved has been removed because of copyright restrictions

Fig. 6-10   Phase space for electron transmission through a CoSi$_2$/Si (111) interface
[148]. An open circle represents a state at that energy in the CoSi$_2$, and a plus
sign represents a state in Si, a closed circle represents that there is a state in
both.

132

CHAPTER 7. EXPERIMENTAL METHODS[3]

7.1   Instrument Modification

Although there have been many BEEM studies of various combinations of metals and semiconductors, as reviewed in the literature section, details of the instrument modification are still lacking. In this project, we present an economical method for modifying a conventional STM for BEEM measurement.

7.1.1   Original STM Preamplifier

The STM employed here is a Burleigh STM operated in ambient atmosphere and at room temperature. The original head circuit of the STM uses a simple circuit arrangement which converts the tunneling current to a voltage to be used by feedback electronics. A bias voltage was applied to the STM tip relative to the sample. Approach and control circuitry then bring the tip to within the tunneling distance of the sample surface. The tunneling current flows through the sample to a virtual ground connection, which is the sample mounting stage. The sample mounting stage is connected to the tunneling current measuring preamplifier, providing a return path for the tunneling current. The tip bias voltage lead and the tunneling preamplifier are separated (Fig. 7-1). The tunneling current preamplifier first converts tunneling current into a voltage (-22.1mV/nA), which is then amplified to a level of 100mV/nA by an inverting amplifier, and finally returned to the feedback electronics by a buffer amplifier (Fig. 7-2). The bias voltage circuitry utilizes a differential amplifier with a gain of 1, and a buffer amplifier to bias the voltage at the tip (Fig. 7-3).

7.1.2   Modified STM and BEEM Preamplifier

To detect the BEEM signal, the tunneling current return path has to be separated from the return path of the ballistic electrons. A new sample mounting platform was fabricated (Fig. 7-4), based on a design given in Ref 136. In this modified form, the STM tip protrudes through the aperture of a quartz mounting plate with three indium spots. The sample is held in place by a spring ohmic contact to the backside of the sample. The tunneling current return path is provided by contacting one of the three indium spots to the metal layer. This indium spot is connected to a real wired ground, which acts as a reference input for both the STM and BEEM amplifiers. Tunneling current measurement is performed using a new circuit, which also simultaneously biases the STM tip (Fig. 7-5). The feedback amplifier used to bias the tip also serves as a current-to-voltage converter and converts tunneling current to a voltage at a level of -10mV/nA, so that the voltage at V1 (Fig. 7-5) will be (V−10) mV/nA (where V is the bias voltage). To eliminate any dependence of the tunneling current on V, a differential amplifier was used to subtract the bias voltage from V1 and simultaneously amplify the signal to a level of −100mV/nA. The ballistic electron current flows from the backside of the semiconductor to a new, more sensitive, virtually grounded measuring preamplifier (Fig. 7-6). The BEEM amplifier is similar to the STM amplifier, in that it first converts the BEEM current to a voltage at a level of −100mV/pA, then uses two stages of amplification with a total gain of −1000 to amplify the voltage to a level of 100mV/pA. The selection of the BEEM amplifier is very important because of the extremely small current to be measured.

7.1.3   Low Pass Filter

The current amplifier has an inherent input noise of $100nV/(Hz)^{1/2}$ across a diode impedance of about $100k\Omega$, so that a noise current of picoamps will be produced, which is on the order of the signal to be measured. This magnitude of the noise necessitates a low pass filter, with an extremely low cutoff frequency, to filter the noise out of the BEEM signal. TLC27 series operational amplifiers were used to create a 4-pole filter (Fig. 7-7). With this filter, a cutoff frequency of 0.16Hz is selected, so that 60Hz noise

134

can be filtered down to about −200dB. The excellent DC characteristics of this filter also make it well suited for this type of post-processing work, since the filter amplifier has very little noise, offset and drift relative to the BEEM amplifier. Alternative outputs were also designed- filtered direct output and filtered output with offset adjustment. The offset adjustment part was done using a summing amplifier to subtract an offset signal from the filtered signal.

7.2   Data Acquisition and Software

7.2.1   Bias Voltage Manual Control Board

A manual control board is designed to accurately change the bias voltage, schematically shown in Fig. 7-8. If the main switch is set "there", the bias voltage can be either changed by the Burleigh bias voltage button or changed by the DAC of the BEEM parameter control form. If the main switch is set "here", the bias voltage can be changed by the manual control board, and two different values of voltage (V1 and V2) can be set, thus voltage can jump from V1 to V2.

7.2.2   Data Acquisition

A data acquisition and control system was designed to perform the data collection. A MetraByte DAS 1602 A/D data acquisition card was plugged into an ISA standard PC expansion slot. The board contains analog and digital IO hardware.

7.2.3   Visual Basic Software

BEEM control software was written in Visual basic. Window-based Visual Basic software has many built-in advantages over DOS systems. It simplifies the program; the graphical user interface is easily created by dragging and dropping the desired elements,

135

such as command buttons onto the forms which will serve as the application interface. The code (program) used for actual performance of specific tasks is then attached to the interface elements. The attachment of the code to the command button was done via the setup of the control forms, which are listed in Appendix 1. The Visual Basic program consistently scans for interrupts generated by the user, such as pressing a command button, and executes the code associated with that particular button. Fig. 7-9 is the main BEEM control form (Form1). An additional parameter control form is shown in Fig. 7-10 (Form2). The color, size, caption, etc. of the forms can be determined by changing the setup of the form texts, which are listed in Appendix 2.

The Visual Basic program written for BEEM performance is very simple. The command dialog will open the data file before reading the data. The software reads all the parameters from the different channels. The following code is used to read the tip bias voltage.

```
daserr = K_ADRead ( DevHandle, 0, 2, MyCnt)

If daserr <> 0 Then

        MsgBox "K_ADRead Error" + Hex$ (daserr), 16, "DAS-1600 Error"
        End

End If

MyCnt = GetVal12 (MyCnt)

trvolt = (((MyCnt - 2048#) x span1) / 4096#) x 1000#

Label7.Caption = Cstr (brvolt)
```

The windows application programming interface (API) calls K_ADRead to read data MyCnt from channel 0 with gain 2. The next API calls GetVal2 to read the counts. According to the Gain, counts are converted to millvolts. Finally, the caption is labelled into the Visual Basic picture box in the main form. Details of the Visual Basic programs for BEEM measurement are listed in Appendix 3.

In order for Visual Basic to recognize any of the calls to window API, each API function or subroutine must be "Declared" in an appropriate Visual Basic code mode.

For example, to use the API function K_ADRead, the following declaration must appear in the projects code module.

Declare Function K_ADRead Lib "DASSHELL.DLL" (ByVal hDev As Long,

ByVal nChan As Integer, ByVal nGain As Integer, pData As Integer) As Integer

In this declaration, the location of the function is specified (Windows DASSHELL.DLL library), as are the function fields (ByVal hDev, ByVal nChan, ByVal nGain, pData) and their type (Integer), and also the type returned by the function (Integer). A complete listing of the Windows API declarations for Visual Basic is given in Appendix 4.

7.3   Thin Film Deposition

Film deposition was done at AMC by means of electron beam evaporation. All the films were deposited as a two-lobed pattern via a shadowing mask described in Chapter 3. The diode area is designed to be $0.05cm^2$. Thus the theoretical lowest measurable Schottky barrier is 0.70eV at room temperature.

The deposition procedure of Au on n-type <100> oriented Si substrates was described in Chapter 3. In order to examine substrate cleaning procedure effects, a similar deposition was also done with Si substrates cleaned by a weak HNO_3 solution (H_2O: HNO_3:HF = 450:5:1) for 30s, rinsed by deionised water, and blown dry with dry nitrogen.

Deposition of nickel and gold on Fe doped <100> InP was done similar to gold on Si. InP was cleaned by the standard procedure described in Chapter 3, and covered by the shadowing mask. The metal film thickness was also required to be around 10nm, and the deposition process was monitored by the quartz thickness monitor, calibrated prior to the deposition. The deposition rate was 0.2nm/s, and the base pressure during the deposition was 2×10^{-7} torr.

7.4   Thin Film Characterization

137

Metal-semiconductor interfaces were characterized by both the TEM and the BEEM.

7.4.1 TEM

Cross section TEM specimens were made to check the film thickness, interface uniformity and oxidation of the substrate.

7.4.2 BEEM measurement

BEEM measurements were done by sweeping the voltage while the holding tunneling current constant under feedback control at a single location. To further improve the signal to noise ratio, 10 to 15 BEEM spectra (sweeping the voltage upward and downward) were averaged at each surface location.
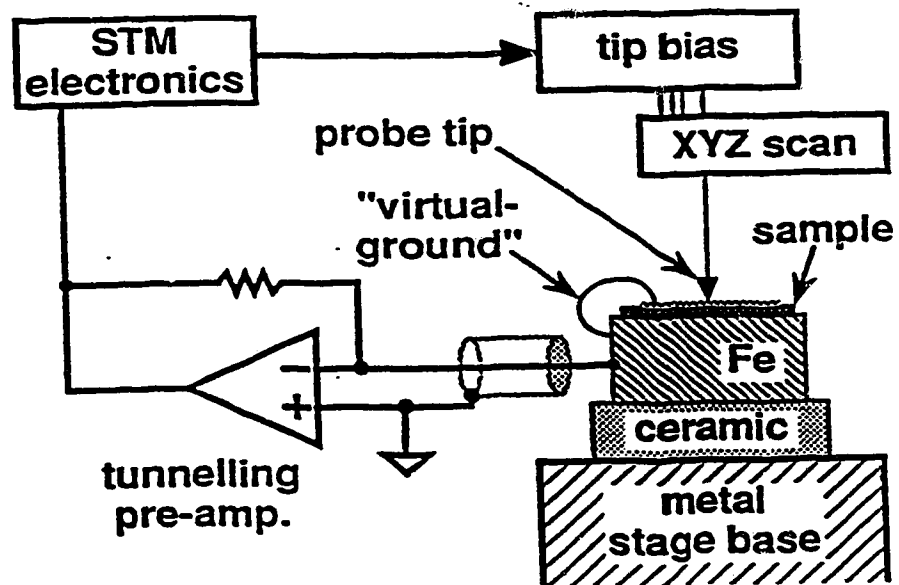
Fig. 7-1   Block diagram of the original STM.
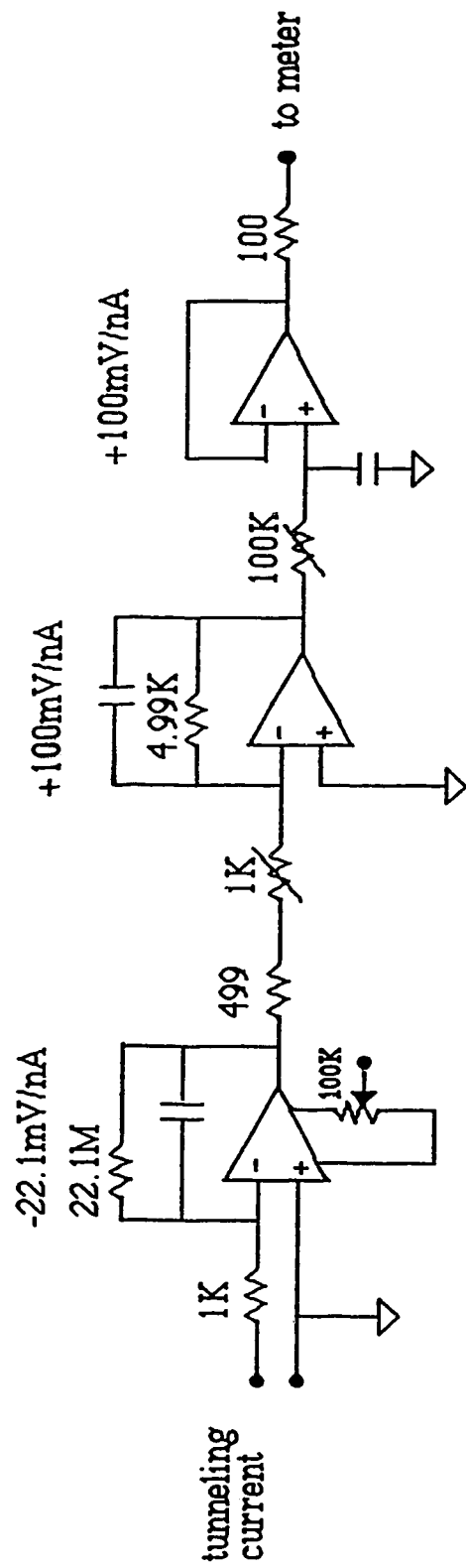
Fig. 7-2   Original Burleigh STM tunneling current preamplifier circuitry.

140
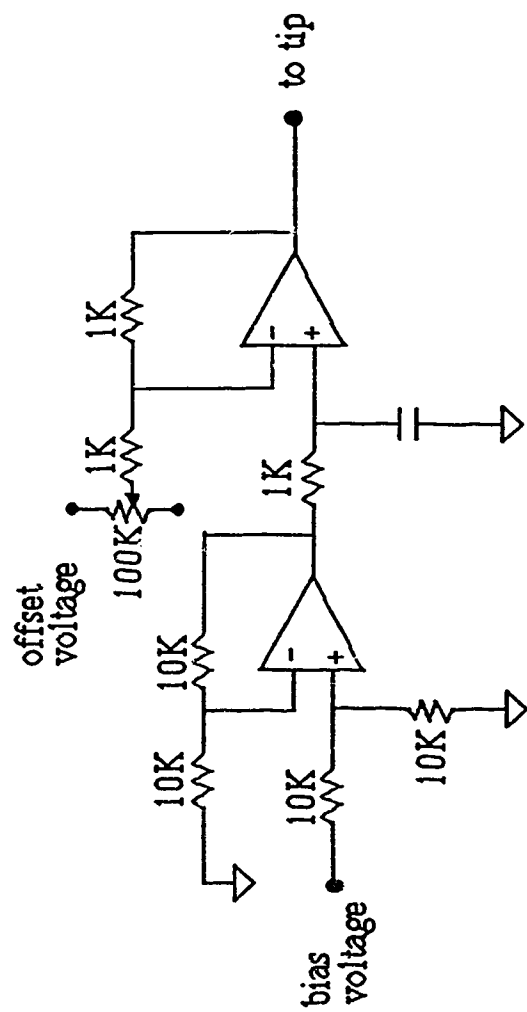
Fig. 7-3   Original Burleigh STM bias voltage circuitry.

141
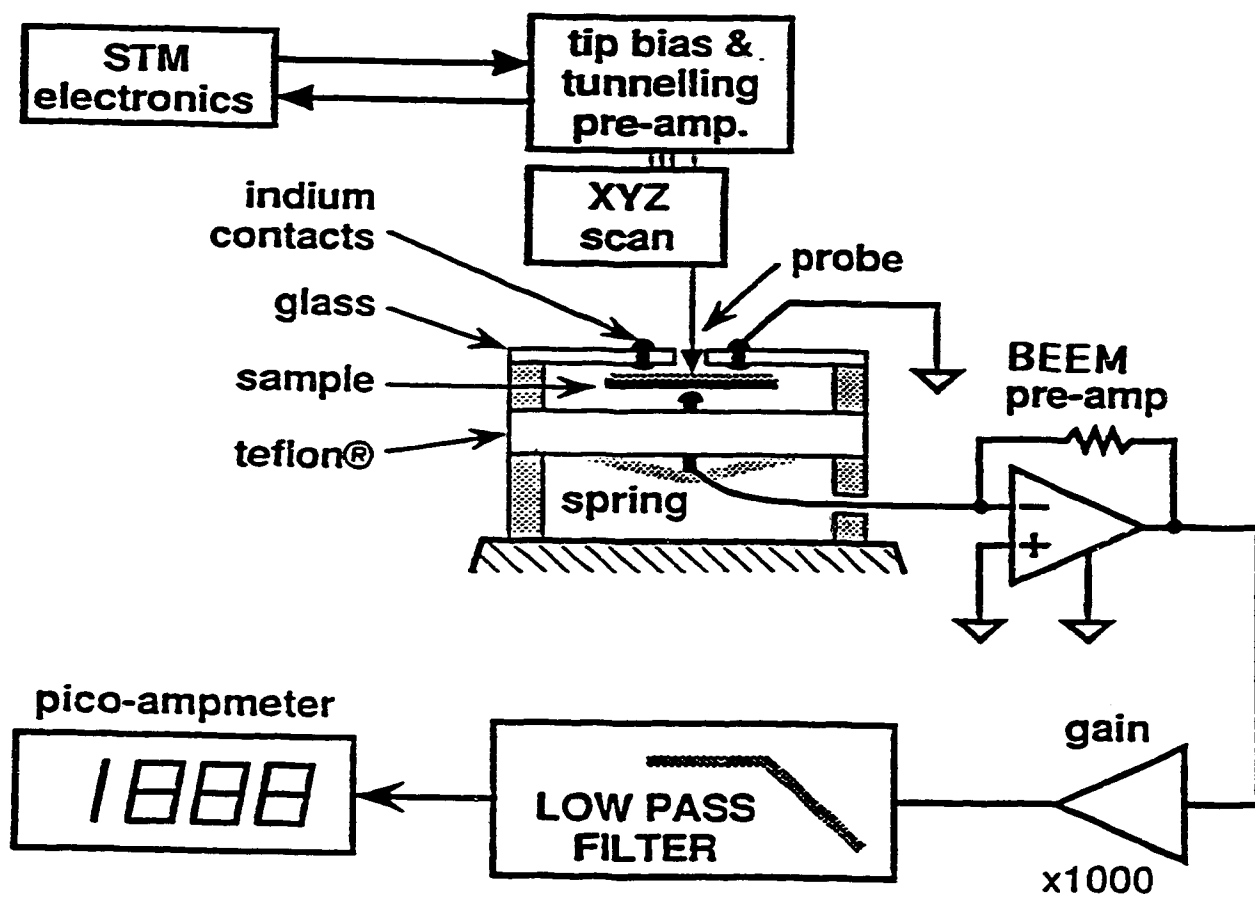
Fig. 7-4   Block diagram of the modified STM and BEEM.
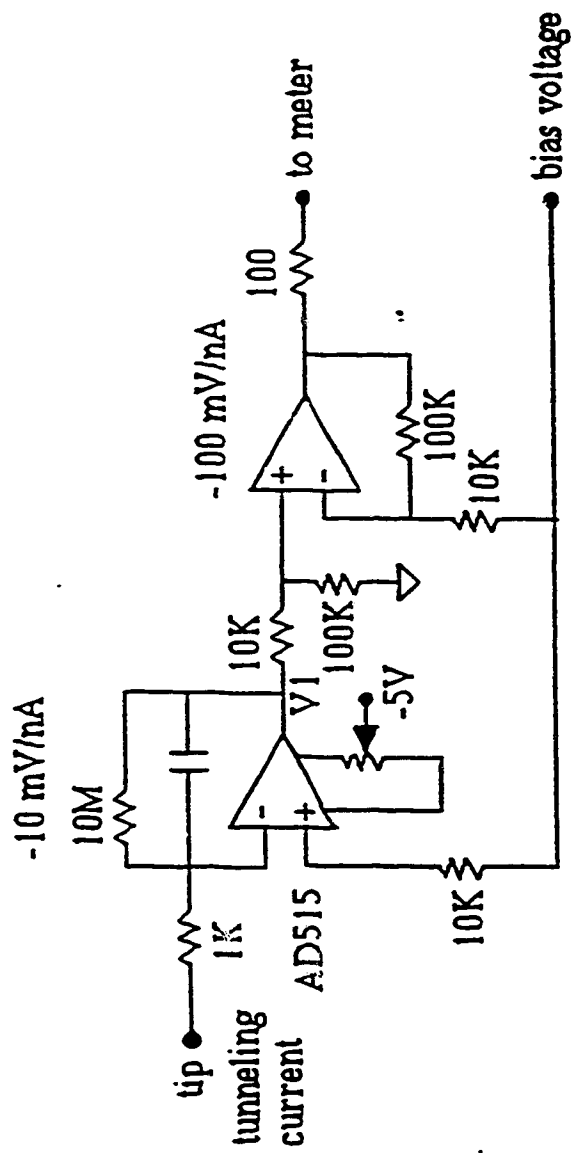
Fig. 7-5   Modified STM bias voltage and tunneling current preamplifier circuitry.

143
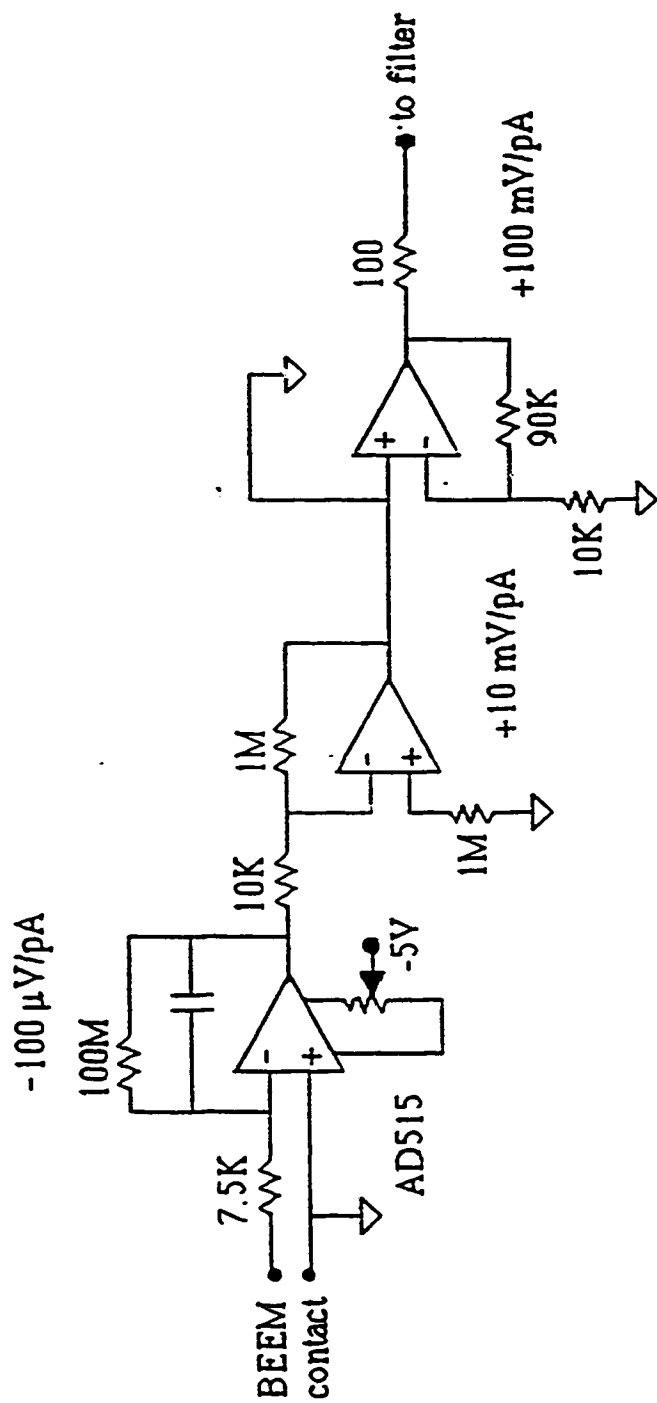
Fig. 7-6   BEEM preamplifier circuitry.

144
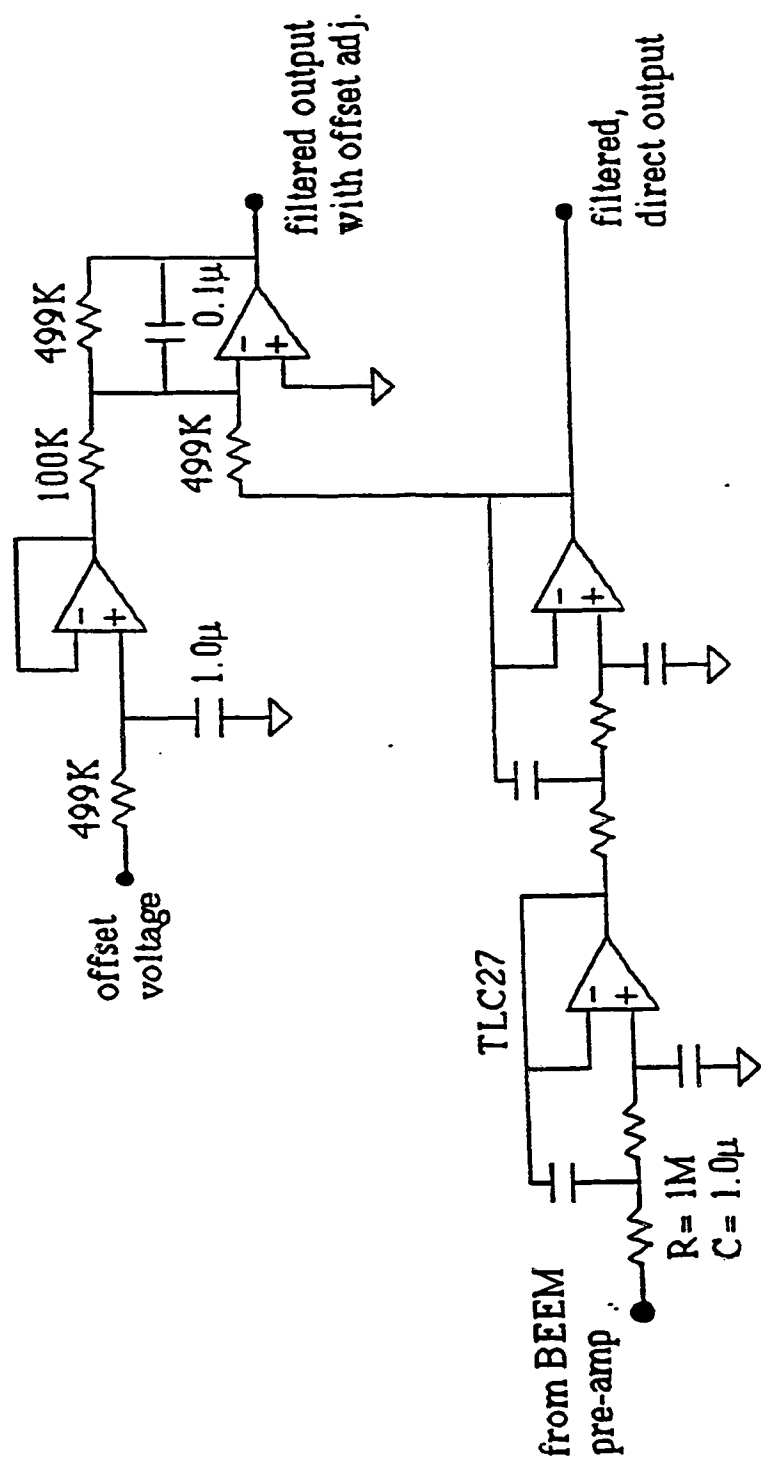
Fig. 7-7   Low-pass filter circuitry.

145

Burleigh V   DAC   Man. 1   Man.2

there   here

tip
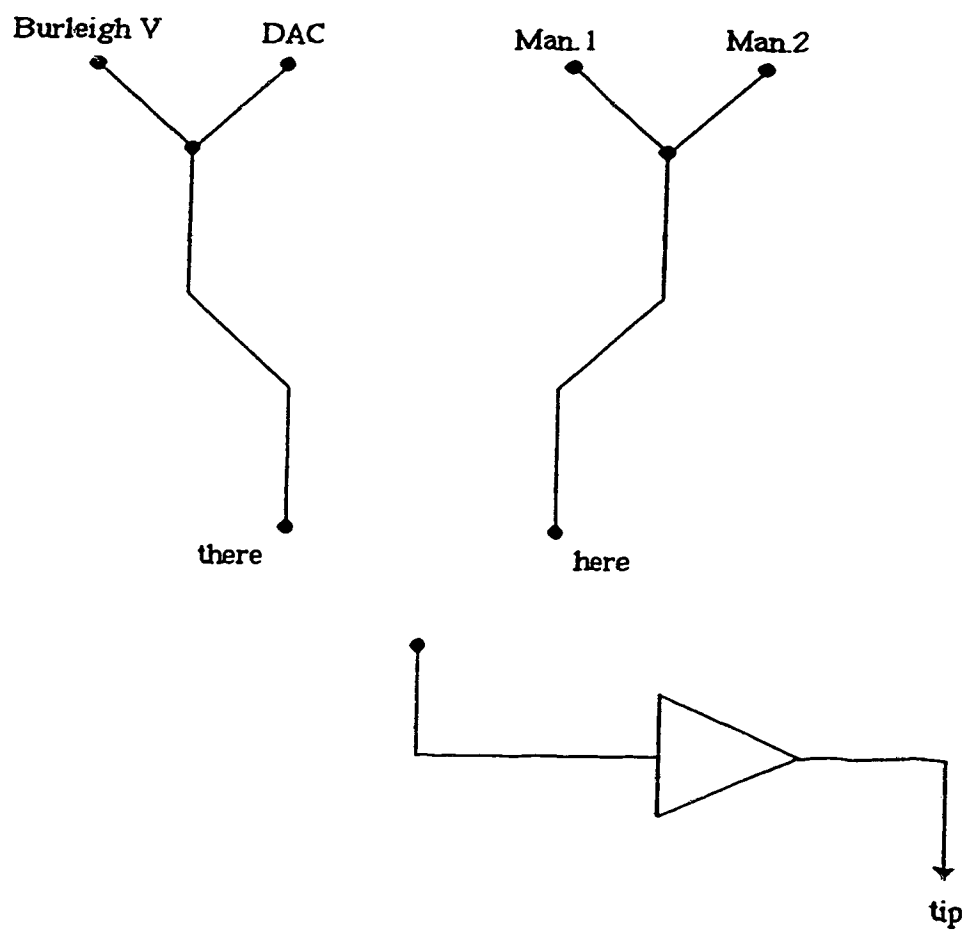
Fig. 7-8   Schematic diagram of the manual control board.

146
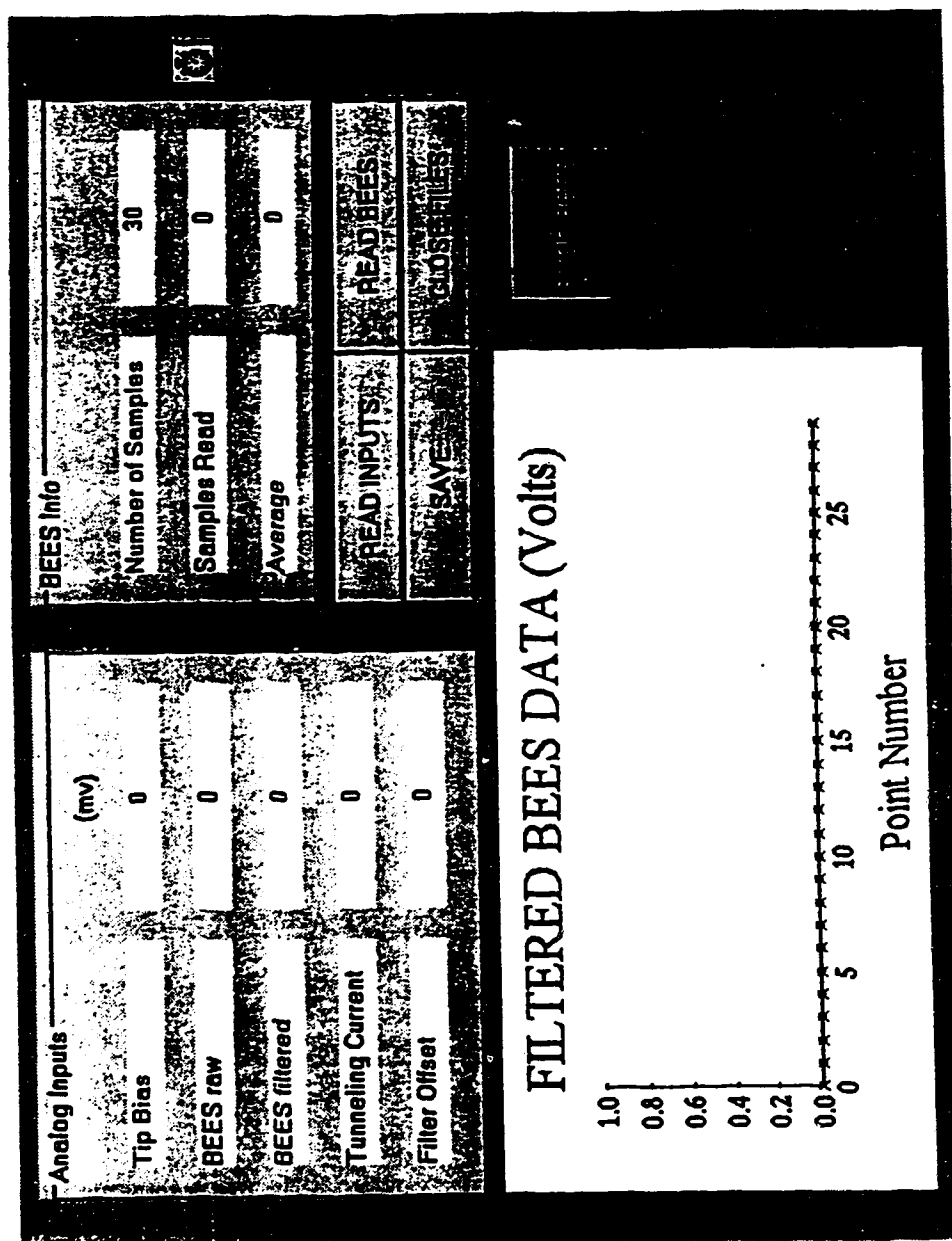
Fig. 7-9   Diagram of the BEEM measurement control form.

147

Fig. 7-10 Diagram of the parameter control form.

148

CHAPTER 8. RESULTS AND DISCUSSION[4]

8.1   Instrument

A problem was discovered when the modified STM/BEEM system was tested. Using a typical reference tunneling current of 1nA would cause the approach to fail repeatedly. This is because the original design was impervious to the capacitively coupled noise current of the piezoelectric element, since the tunneling current measurement preamplifier was located some distance from the piezoelement. In the modified form, the tunneling current measuring lead is the same as the tip-bias lead and it runs through the inside of the hollow piezo-element. The piezoelement operates at a high voltage level and the voltage applied to it can change very rapidly as tip approaches. Since the tunneling current measuring lead runs in very close proximity to the piezoelement internal electrodes, it is likely to pick up capacitively coupled charge when the voltage applied to the piezoelement changes very suddenly. It was discovered that if the reference current was increased to about 30 nA then the induced pulse of the tunneling current would be insufficient to cause the approach circuit to abort the approach. Once tunneling was established at a higher current, it could be easily reduced to any operating level.

Testing of the new circuitry for basic tunneling and image collection proved it to be reliable, although a few of the control parameters, particularly the scan delay, had to be readjusted to optimize the quality of the image.

It has also been found that it takes at least an hour to stabilize the BEEM signal after the sample has been put into the head. The observed drifting of the BEEM signal for this duration is likely due to thermoelectric potential between the various components which make up the STM head and the sample itself. Since the sensitivity of the BEEM preamplifier is so high, it would take only a small amount of thermoelectric potential to induce a substantial amount of current error into the system.

Another important thing for this modification is that the STM head has to be kept in absolute darkness since even slightest amount of the light would produce a photo-current which is orders of magnitude larger than the BEEM current [136]. The shielding of the light is accomplished by a black lid covering the STM head.

8.2   Application

8.2.1   Au/Si(100)

Au/Si(100) was selected to test the BEEM system because of its well known high quality and reproducible barrier height.

In order to investigate the effect of gold diffusion into silicon, the BEEM spectra of samples right after deposition and three days after deposition were compared. The BEEM spectra of the Au/n-type Si(100) right after deposition were similar at all locations of the sample. A typical spectrum is shown in Fig. 8-1. The Schottky barrier derived from it is $0.80 \pm 0.02eV$, which is in good agreement with the previous BEEM results of $0.86-0.92eV$ [13, 14] and conventional spatially averaged current-voltage results (e.g., $0.85eV$ [153]). From Fig. 8-1b, the BEEM signal variation due to both the drift and the noise is shown (this is same spectrum as in Fig 8-1a), and this is the main reason that the BEEM spectra are averaged from 10-15 single measurements. The number of measurements is based on both the measurement time and the reduction of the noise level. This BEEM signal variation at a single location became worse for the sample three days after deposition, illustrating that diffusion degrades the quality of the interface and thus increases the noise level of the signal. The Au/n-type Si(100) system right after deposition was thus used for BEEM instrument calibration for later measurements.

For the sample three days after deposition, the BEEM current varies from location to location, despite the same bias voltage and tunneling current. The noise level of the BEEM signal increased significantly (Fig. 8-2). However, there is no significant change in the Schottky barrier height. The spacial variation of the BEEM current for the samples

three days after deposition is believed to be due to the inelastic scattering of ballistic electrons at the Au-Si interdiffusion layer formed at the interface. This can be further verified by the fact that there is no BEEM signal observed for the sample seven days after deposition, in which a significant interdiffusion layer was formed, resulting in much stronger inelastic scattering effect of the ballistic electrons (Fig. 8-3a). This is similar to previous results on the Au/n-type Si (111) system with a UHV cleaned interface [157, 158]. The only difference might be the interdiffusion rate. In our substrate cleaning procedure (buffer HF solution, described in Chapter 3), it took seven days to result in complete disappearance of BEEM signal. However, it has not been mentioned whether there was any time lag between BEEM measurement and the sample preparation for Au/Si (111) system, with substrate preheated at 830°C in UHV, when no BEEM signal was detected [157, 158].

BEEM measurement on Au/n-type Si (100) with the substrate cleaned by a weak HNO$_3$ solution was also carried out to observe interface oxidation effects. TEM images of both interfaces are displayed in Fig. 8-4. Evidently the gold film peeled off during the cross section specimen preparation for the weak HNO$_3$ (H$_2$O: HNO$_3$:HF = 450:5:1) cleaned sample, indicating the existence of an oxide layer at the interface which is also visible in Fig. 8-4b. There is no BEEM signal observed when the bias voltage is swept up. This is due to the significant inelastic scattering of the ballistic electrons at the interface oxide layer. A BEEM current occurred suddenly after holding the bias voltage at 1.5eV at a single location for a period of time. This process is irreversible, and the subsequent spectrum taken at the same point is similar to Fig. 8-1. According to Hallen and Fernandez's [157, 158] subsurface interface modification, the BEEM current reached a maximum and dropped to a lower value as the bias voltage was swept up to 3-4eV for Au/Si (111) with an HF treated interface, where a monolayer of C, O and F was detected at the interface by X-ray photoemission spectroscopy (XPS). (Presumably H was also present, but cannot be detected by XPS). Similar modification was also observed for a Cl-doped interface. However, there were no modifications observed at UHV preheated and O-doped interfaces. A model was developed, shown in Fig. 6-9, to explain these

phenomena [158]. The monolayer impurities at the interfaces of HF-treated sample (C, O, F, H) and Cl-doped sample were believed to act as barriers which passivate the Au-Si interdiffusion, where an increasing BEEM current with increasing bias voltage is observed. However, the energy input by the tip at 3-4eV enhances diffusion, resulting in a local region similar to a UHV cleaned interface, and a sudden drop of BEEM current occurred [158]. In our experiment, there is no current drop observed after the sudden occurrence of the BEEM current as the bias voltage is swept up to and held at 1.5eV. We believe that the subsurface modification under 1.5eV bias voltage results in the penetration of the oxide layer (electron interaction with the oxide layer) at this location, to form a cleaner interface (similar to buffered HF) without significant formation of a Au-Si interdiffusion layer (Fig. 8-3b). Moving the tip to other locations requires additional time to observe the sudden occurrence of the BEEM current. The length of the time ranges from 3min to 10min, depending on the condition of the interface, presumably due to inhomogeneities in the interface oxide layer.

8.2.2 Ni/InP

The calibrated BEEM instrument was used to measure the Schottky barrier height of the Ni/InP (Fe doped) interface. A TEM image shows that the Ni-InP interface region is amorphous, free of oxide, and very uniform with a thickness of 16nm (Fig. 8-5a). However, no BEEM signal was observed.

According to Hokelek et al. [174], the Schottky barrier of the Ni/p-type InP, from the current-voltage measurements, is 0.897eV. Although various degrees of intermixing of In and P with Ni were detected in their experiments using Auger Electron Spectroscopy (AES) depth composition profiling technique, the actual extent of this apparent intermixing was unable to be determined due to the electron beam induced effects associated with the AES technique [174]. Later results of both Ivey et al. [175] and Sands et al. [176] showed that Ni reacted with InP during deposition, and an amorphous ternary phase Ni-In-P was reported between Ni and InP. In this experiment, because of such a thin

layer, the entire Ni layer reacted with InP and formed an amorphous ternary layer (Fig. 8-5a). The reasons that there is no BEEM current detected are not clear at this time, but could be due to any of the following:

(1) The ballistic hole has a shorter mean free path than a ballistic electron;

(2) As has been reported on Ni/n-type GaP interfaces [145], the mean free path of ballistic electron in the Ni film is reduced significantly compared to the other metal. This could also be applied to a ballistic hole;

(3) Similar to the weak HNO₃ treated Au/Si interface (oxide layer), inelastic scattering might strongly take place in the amorphous Ni-In-P tenary phase;

(4) The Schottky barrier between the Ni-In-P amorphous layer and InP (Fe) may be lower than 0.70eV;

(1), (2) and (3) will mean that virtually no electrons have energy higher than the Schottky barrier height when they reach the interface. In these cases, a thinner film can be used to reduce the scattering. (4) will result in a the Schottky barrier less than the measurable value of the instrument at room temperature. Thus, the BEEM signal cannot be separated from the background noise. In this case, a suitable p-type InP substrate is needed for further experiment.

8.2.3   Au/InP

In order to simplify the problem, a gold thin film was fabricated on the same InP substrate. A TEM image of Au-InP interface shows a uniform gold layer with a thickness of 16nm, without any substrate surface contamination (Fig. 8-5b). Again, no BEEM signal was observed.

According to the traditional current-voltage results, the Schottky barrier for Au/p-type InP is 0.794eV [174], which is larger than the detectable value. However, the InP substrate used in this experiment is Fe-doped, and semi-insulating (Fe is a deep level acceptor). This may result in a Schottky barrier at the Au/ InP (Fe) interface lower than

153

0.70eV. To further carry on BEEM measurements of the Au/InP interface, a suitable p-type InP wafer is needed.
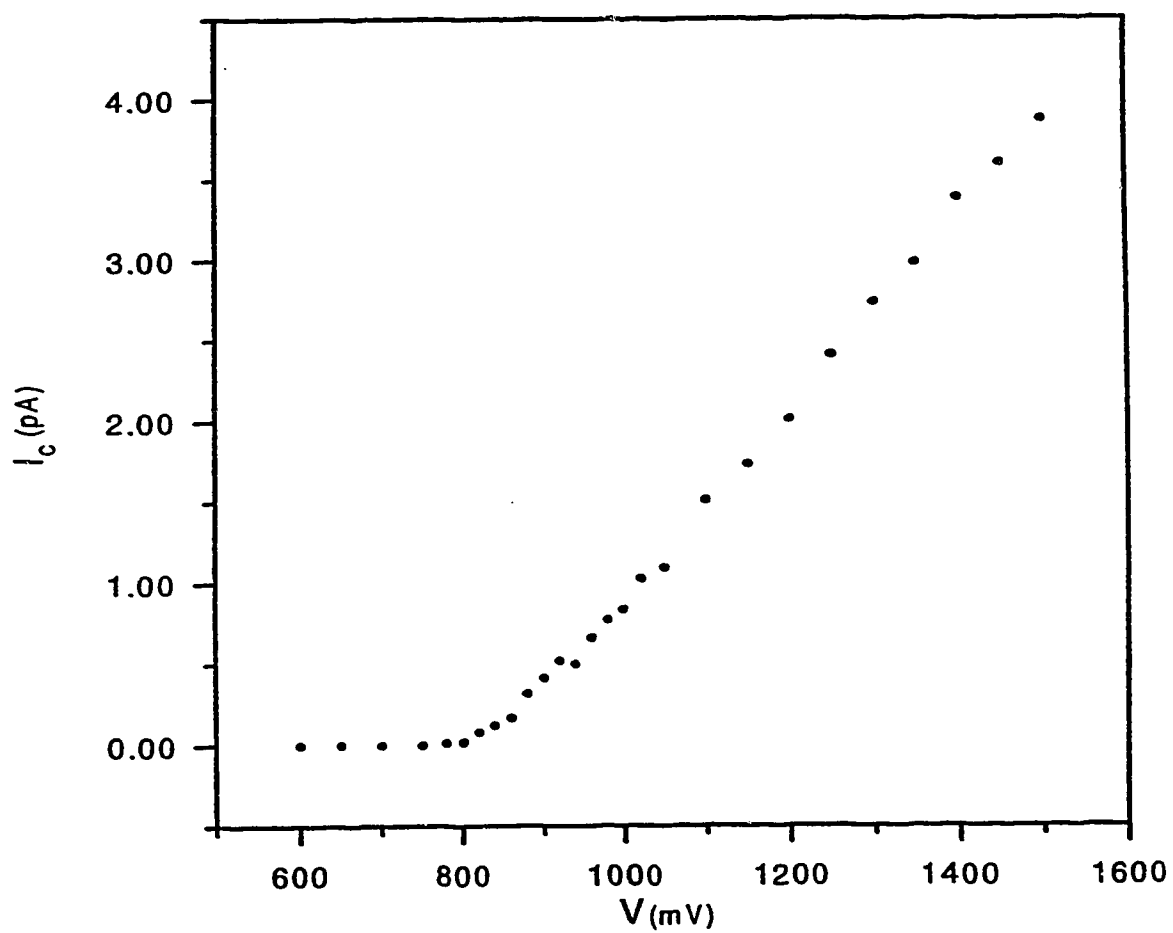
Fig. 8-1 (a) BEEM spectrum of collector current (I_C) vs tunnel voltage (V) for Au/n-type Si (100) right after deposition. A constant tunneling current of 1.5nA was used.

155
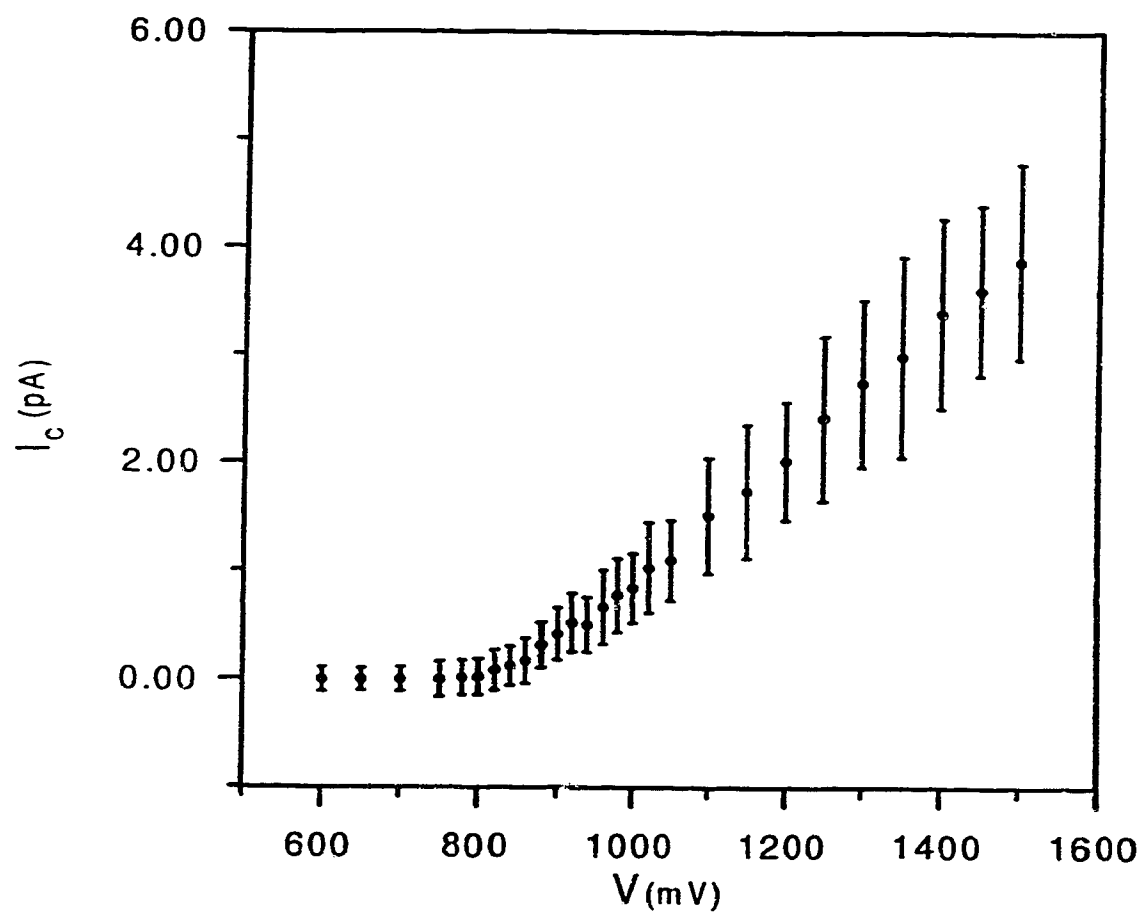
Fig. 8-1   (b) same as (a), showing the BEEM signal variation at a single location.

156
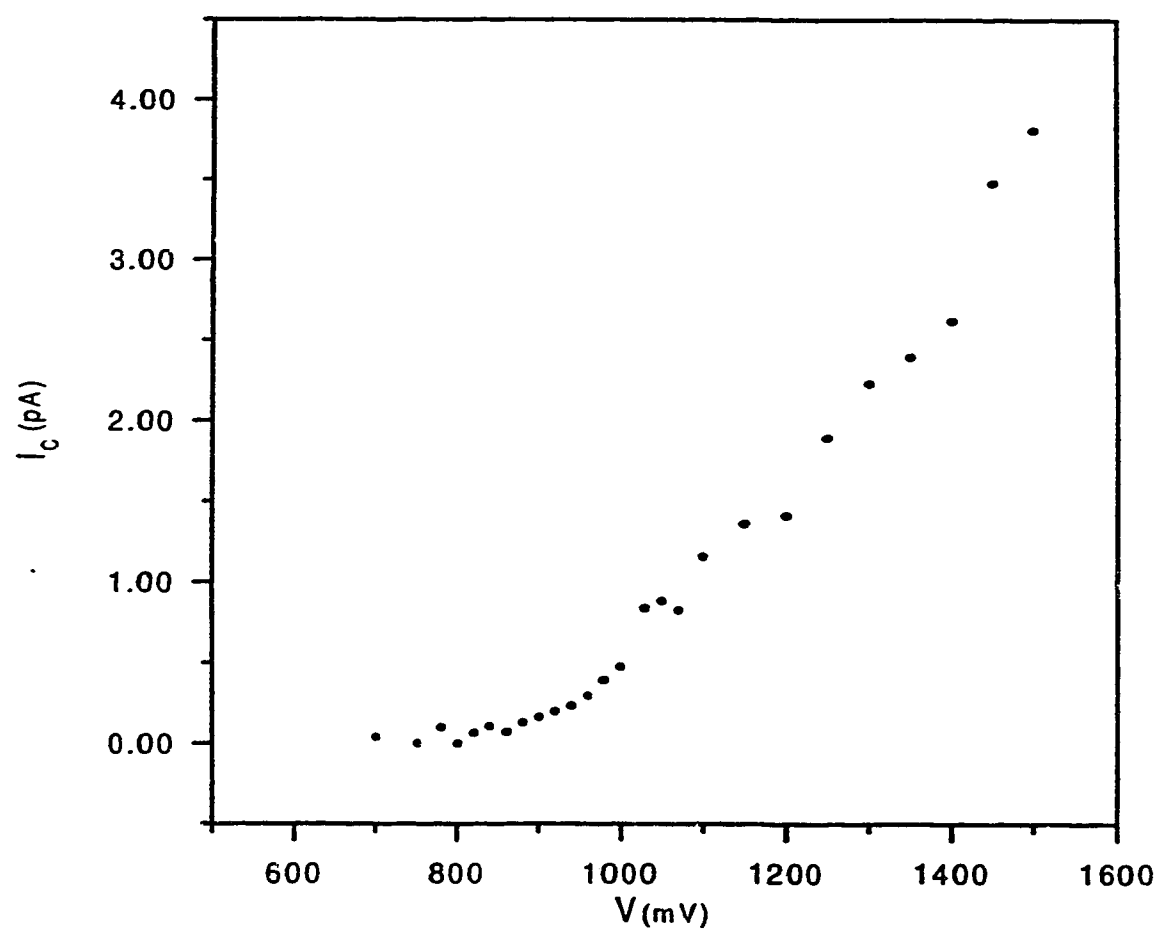
Fig. 8-2 BEEM spectrum of I_C-V for Au/n-type Si (100) three days after deposition. A tunneling current of 2nA was used.
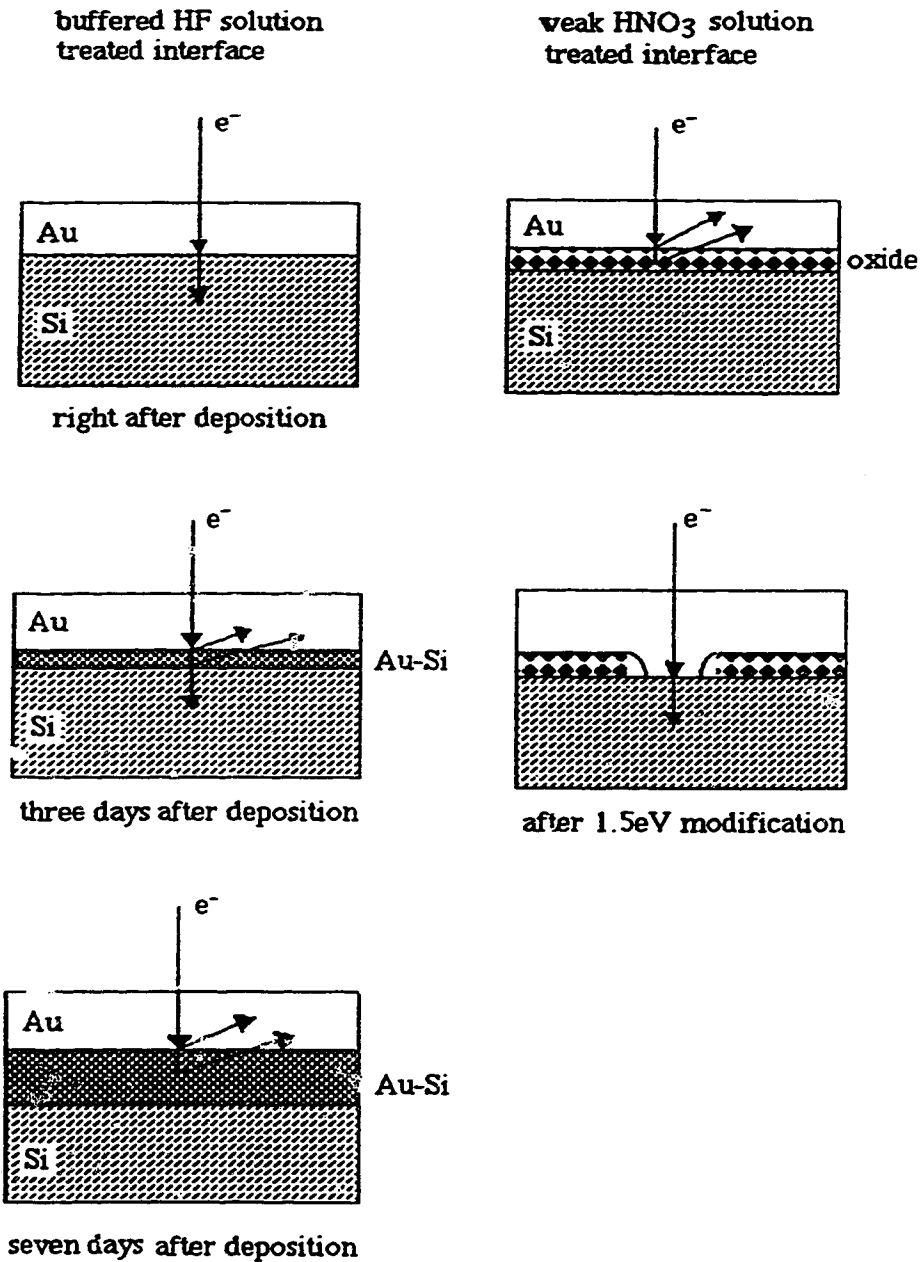
Fig. 8-3   Schematic drawing of the Au/Si (100) interface models. (a) the buffered HF solution treated interfaces before and after the formation of Au-Si intermix layer; (b) the weak HNO₃ solution treated interfaces before and after 1.5eV modification.

(a)

Si

Au

glue

(b)

Si

oxide
Au

glue

200nm
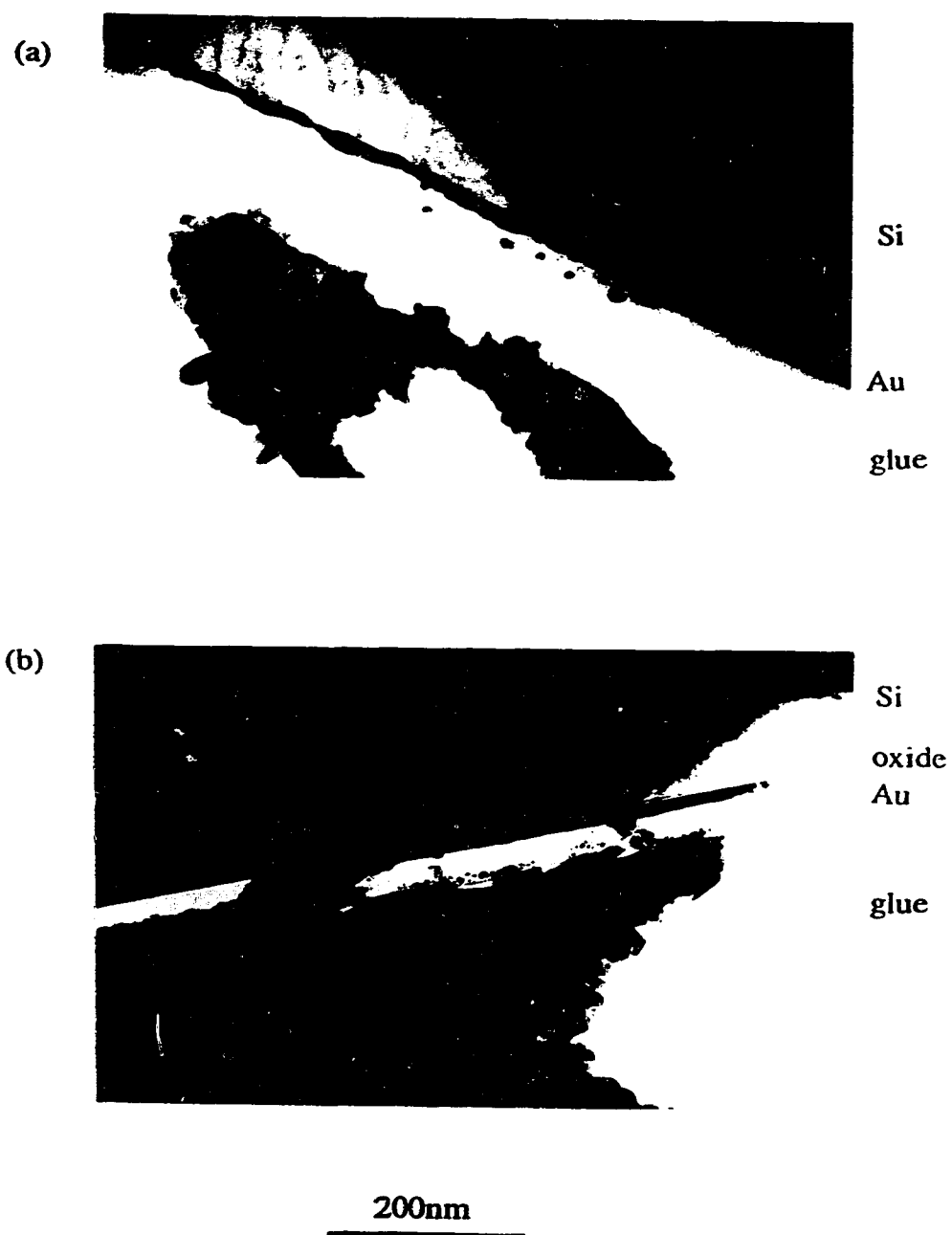
Fig. 8-4   TEM images of Au/Si(100) samples. (a) Si substrate cleaned by 10 : 1 buffered hydrofluoric acid solution; (b) Si substrate cleaned by weak HNO$_3$ solution.

159

(a)

InP

Ni - In - P

glue

(b)

InP

glue   Au

200nm
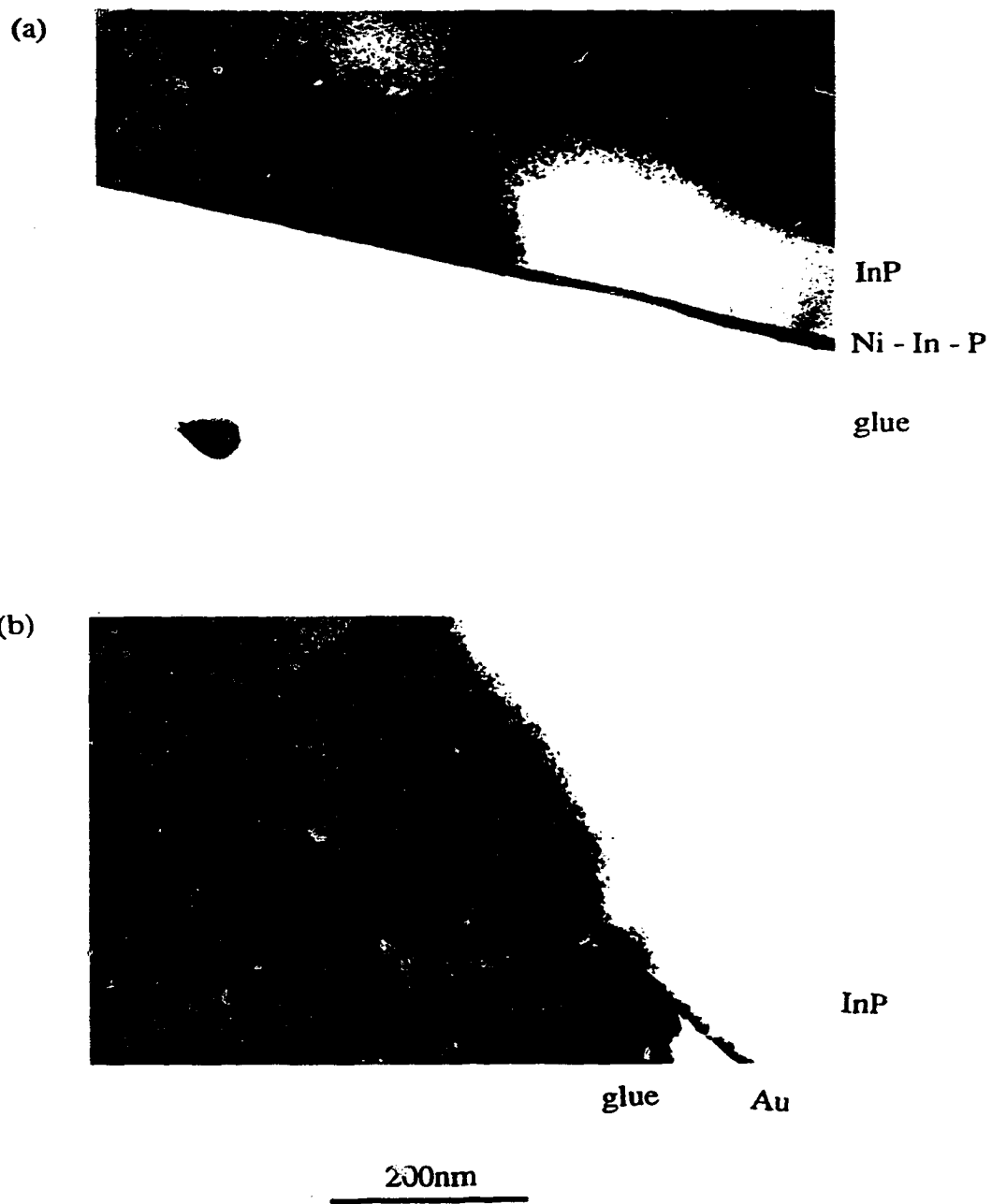
Fig. 8-5   TEM images of (a) Ni/InP (Fe); and (b) Au/InP (Fe).

160

CHAPTER 9. CONCLUSIONS AND RECOMMENDATIONS

9.1 Conclusions

In this project, the instrument modification of STM to BEEM has been carried out. The roles of the interfacial layers of Au/Si (100) interfaces have been investigated. Initial BEEM measurements on metal/InP systems have been attempted. Several conclusions can be made according to the experimental results.

1. The instrument modification has proven to be successful.

2. The formation of an Au-Si intermixed layer causes significant scattering of the ballistic electrons and is responsible for the disappearance of the BEEM current for the samples aged for seven days at room temperature.

3. A bias voltage of 1.5eV altered the oxide layer at the Au/Si (100) interface resulting in an interface similar to that cleaned by buffered HF solution.

9.2 Recommendations

BEEM measurements on metal/InP systems need to be continued and p-type InP wafers are needed as are thinner metal layers. The former is to ensure that the barrier height is higher than the instrument measurable height of 0.70eV. The latter is to minimize the scattering of ballistic holes in the metal layer. Liquid nitrogen cooling of the BEEM apparatus would allow measurement of lower barrier heights.

For the Ni/InP system, because of the reaction taking place at the interface, conventional I-V measurements of the barrier height between the Ni-In-P ternary phase and InP would be useful to check whether the barrier height is larger than 0.70eV.

In order to accurately determine the Schottky barrier height from the BEEM spectra, theoretical BEEM spectra can be calculated to fit the experiment data by writing a program to simulate the metal/InP interfaces. Because the power laws were derived for

161

T = 0K, they are valid only near the threshold. However, when fitting a spectrum, the Fermi function must be integrated over the energy variable. There are two ways to do this:

(1) Use the j_c deviation equations in Ref. 147, and then integrate them (use InP parameters instead of GaP parameters provided in reference). This has to be done numerically.

(2) Higher order approximations of the j_c equations, which are also explained in Ref. 147 can be included in the calculation instead of the integration.

The latter becomes more inaccurate over a broad energy range. Details of the theoretical calculation of the BEEM spectrum are provided in Ref. 147.

References

1. G. Binnig, H. Rohrer, Ch. Gerber and E. Weibel, Appl. Phys. Lett., 40, 178 (1982)

2. G. Binnig, H. Rohrer, Ch. Gerber and E. Weibel, Phys. Rev. Lett., 49, 57 (1982)

3. S. Park, J. Nogami, and C. F. Quate, Phys. Rev., B36, 2863 (1987)

4. J. P. Pelz and R. H. Koch, Phys. Rev., B41, 1212 (1990)

5. R. Sonnenfeld and P. K. Hansma, Science, 232, 211 (1986)

6. R. Sonnenfeld, J. Schneir, B. Drake, P. K. Hansma and D. E. Aspnes, Appl. Phys. Lett., 50, 1742 (1987)

7. D. P. E. Smith and G. Binnig, Rev. Sci. Instrum., 57, 2630 (1986)

8. P. J. M. van Bentum, L. E. C. van de Leemput, R. T. M. Smokers and H. van Kempen, J. Microsc., 152, 11 (1988)

9. A. P. Fein, J. R. Kirtley and R. M. Feenstra, Rev. Sci. Instrum., 58, 1806 (1987)

10. H. K. Wickramasinghe, Scanning Tunneling Microscopy, Eds. J. A. Stroscio and W. J. Kaiser, Acad. Press, CA (1993), pg177

11. G. Binnig, C. F. Quate, and Ch. Gerber, Phys. Rev. Lett., 56, 930 (1986)

12. T. R. Albrecht and C. F. Quate, J. Vac. Sci. and Tech., A6, 271 (1988)

13. W. J. Kaiser and L. D. Bell, Phys. Rev. Lett., 60, 1406 (1988)

14. L. D. Bell and W. J. Kaiser, Phys. Rev. Lett., 61, 2368 (1988)

15. G. Binnig, H. Rohrer, Physica, 127B, 37 (1984)

16. R. J. Dwayne Miller, H. A. Mizes, and A. Samsaver, Burleigh Instructional STM Workbook, Burleigh Instruments, Inc., NY, 1992

17. D. A. Park, Introduction to the Quantum Theory, NY, 1974
    S. Gasiorowicz, Quantum Physics, NY, 1974

18. J. Tersoff and N. D. Lang, Scanning Tunneling Microscopy, Eds. J. A. Stroscio and W. J. Kaiser, Acad. Press, CA (1993), pg1

19. C. J. Chen, Introduction to Scanning Tunneling Microscopy, 1993

20. D. A. Bonnell, Scanning Tunneling Microscopy and Spectroscopy, Eds. D. A. Bonnell, VCH Publishers, NY (1993), pg7

21. M. Okano, K. Kajimura, S. Wakiyama, F. Sakai, W. Mizutani,, and M. Ono, J. Vac. Sci. Technol., A5, 3313 (1987)

22. S. Park and R. C. Barrett, Scanning Tunneling Microscopy, Eds. J. A. Stroscio and W. J. Kaiser, Acad. Press, CA (1993), pg31

23. S. Park and C. F. Quate, Rev. Sci. Instrum., 58, 2010 (1987)

24. G. Binnig and H. Rohrer, Helv. Phys. Acta, 55, 726 (1982)

25. G. Binnig and H. Rohrer, Sci. Am., 253, 50 (1985)

26. Ch. Gerber, G. Binnig, H. Fuchs, O. Marti and H. Rohrer, Rev. Sci. Instrum., 57, 221 (1986)

27. G. Binnig and H. Rohrer, IBM J. Res. Develop. 30, 355 (1986)

28. J. E. Demuth, R. J. Hamers, R. M. Tromp and M. E. Welland, J. Vac. Sci. Technol., A4, 1320 (1986)

29. H. J. Mamin, D. W. Abraham, E. Ganz, and J. Clarke, Rev. Sci. Instrum., 56, 2168 (1985)

30. K. Besocke, Surf. Sci., 181, 145 (1987)

31. W. J. Kaiser and R. C. Jaklevic, Surf. Sci., 181, 55 (1987)
    W. J. Kaiser and R. C. Jaklevic, Surf. Sci., 182, L227 (1987)

32. M. D. Pashley, K. W. Haberern and W. Friday, J. Vac. Sci. Technol., A6, 488 (1988)

33. W. J. Kaiser and R. C. Jaklevic, Rev. Sci. Instrum., 59, 537 (1988)

34. J. E. Demuth, R. J. Hamers, R. M. Tromp and M. E. Welland, IBM. J. Res. Develop., 30, 396 (1986)
    R. R. Schulz and C. Rossel, Rev. Sci. Instrum., 65, 1918 (1994)

35. J. G. H. Hermsen, H. van Kempen, B. J. Nelissen, L. L. Saethout, G. F. A. van de Walle, P. J. W. Weijs, and P. Wyder., Surf. Sci., 181, 183 (1987)

36. G. Binnig and D. P. E. Smith, Rev. Sci. Instrum., 57, 1688 (1986)

37. K. Kajimura, H. Bando, K. Endo, W. Mizutani, H. Murakami, M. Okano, S. Okayama, M. Ono, Y. Ono, H. Tokumoto, F. Sakai, K. Watanabe, and S. Wakiyama, Surf. Sci., 181, 165 (1987)

38. M. H. Jericho, D. C. Dahn and B. L. Blackford, Rev. Sci. Instrum., 58, 1349 (1987)

39. F. Besenbacher, E. Laegsgaard, K. Mortensen, U. Nielsen, and I. Stensgaard, Rev. Sci. Instrum., 59, 1035 (1988)

40. C. W. Snyder and A. L. de Lozanne, Rev. Sci. Instrum., 59, 541 (1988)

41. V. K. Adamchuk, A. V. Ermakov and S. I. Fedoseenko, Ultramicroscopy, 42-44, 1602 (1992)

42. R. G. Carr, J. Micros., 152, 379 (1988)

43. P. K. Hansma and J. Tersoff, J. Appl. Ohys., 61, R1 (1987)

44. G. Binnig, H. Rohrer, Ch. Gerber, and E. Weibel, Phys. Rev. Lett., 50, 120 (1983)

45. G. Binnig and H. Rohrer, Surf. Sci., 126, 236 (1983)

46. A. Bryant, D. P. E. Smith and C. F. Quate, Appl. Phys. Lett., 48, (1986), 832

47. M. Fotino, Rev. Sci. Instrum. 64 (1), 159 (1993)

48. W. E. Packard, Y. Liang, N. Dai, J. D. Dow, R. Nicolaides, R. C. Jaklevic, and W. J. Kaiser, J. Microsc. 152, 715 (1988)

49. A. J. Melmed, R. D. Shull, C. K. Chiang and H. A. Fowler, Science 239, 176 (1988)

50. R. M. Feenstra and A. P. Fein, Phys. Rev., B32, 1394 (1985)

51. A. J. Melmed, J. Vac. Sci. Technol. B9 (2), 601 (1991)

52. D. K. Biegelsen, F. A. Ponce, and J. C. Tramontana, and S. M. Koch, Appl. Phys. Lett. 50 (11), 696 (1987)

53. D. K. Biegelsen, F. A. Ponce, and J. C. Tramontana, Appl. phys. Lett. 54 (13), 1223 (1989)

54. A. J. Melmed, J. Chem. Phys. 38, 1444 (1963)

55. Y. Akama, E. Nishimura, A. Sakai, and H. Murakami, J. Vac. Sci. Technol. A8 (1), 429 (1990)

56. B. Hubner, H. W. P. Koops, H, Pagnia, N. Sotnik, J. Urban, and M. Weber, Ultramicroscopy 42-44, 1519 (1992)

57. E. W. Muller, Z. Physik 131, 136 (1951)

58. M. Fotino, Appl. Phys. Lett. 60 (23), 2935 (1992)

59. P. J. Bryant, H. S. Kim, Y. C. Zheng, and R. Yang, Rev. Sci. Instrum. 58 (6), 1115 (1987)

60. J. P. Ibe, P. P. Bey, Jr., S. L. Brandow, R. A. Brizzolara, N. A. Burnham, D. P. DiLella, K. P. Lee, C. R. K. Marrian, and R. J. Colton, J. Vac. Sci. Technol. A8 (4), 3570 (1990)

61. R. Nicolaides, Y. Liang, W. E. Packard, Z. W. Fu, H. A. Blackstead, K. K. Chin, J. D. Dow, J. K. Furdyna, W. M. Hu, R. C. Jaklevic, W. J. Kaiser, A.R. Pelton, M. V. Zeller, and J. Bellina, Jr., J. Vac. Sci. Technol. A6 (2), 445 (1988)

62. J. Méndez, M. Luna and A. M. Baró, Surf. Sci. 266, 294 (1992)

63. M. J. Heben, M. M. Dovek, N. S. Lewis, R. M. Penner, and C. F. Quate, J. Micros. 152 (3), 651 (1988)

64. H. Lemke, T. Göddenhenrich, H. P. Bochem, U. Hartmann, and C. Heiden, Rev. Sci. Instrum. 61 (10), 2538 (1990)

65. I. H. Musselman, P. A. Peterson, and P. E. Ressell, Precision Engineering 12 (1), 3 (1990)

66. I. H. Musselman and P. E. Russell, J. Vac. Sci. Technol. A8 (4), 3558 (1990)

67. R. Erlandsson, G. M. McClelland, C. M. Mate, and S. Chiang, J. Vac. Sci. Technol. A6, 266 (1988)

68. G. Reiss, J. Vancea, H. Wittmann, J. Zweck, and H. Hoffmann, J. Appl. Phys. 67 (3), 1156 (1990)

69. R. J. Colton, S. M. Baker, R. J. Driscoll, M. G. Youngquist, J. D. Baldeschwieler, and W. J. Kaiser, J. Vac. Sci. Technol. A6 (2), 349 (1988)

70. H. Morikawa and K. Goto, Rev. Sci. Instrum. 59 (10), 2195 (1988)

71. R. Fainchtein and P. R. Zarriello, Ultramicroscopy 42-44, 1533 (1992)

72. J. P. Song, N. H. Pryds, K. Glejbol, K. A. Morch, A. R. Thölén, and L. N. Christensen, Rev. Sci. Instrum. 64 (4), 900 (1993)

73. L. A. Nagahara, T. Thundat, and S. M. Lindsay, Rev. Sci. Instrum. 60 (10), 3128 (1989)

74. M. Gehrtz, H. Strecker, and H. Grimm, J. Vac. Sci. Technol. A6 (2), 432 (1988)

75. T. Göddenhenrich, U. Hartmann, M. Anders, and C. Heiden, J. Microsc. 152, 527 (1988)

76. T. Tiedje, J. Varon, H. Deckman, and J. Stokes, J. Vac. Sci. Technol. A6, 372 (1988)

77. A. A. Gorbunov, B. Wolf, and J. Edelmann, Rev. Sci. Instrum. 64 (8), 2393 (1993)

78. R. J. Morgan, J. Sci. Instrum. 44, 808 (1967)

79. J. E. Fasth, B. Loberg and H. Nordén, J. Sci. Instrum. 44, 1044 (1967)

80. Th. Michelv. K H. Besocke, and M. Teske, J. Microsc. 152, 77 (1988)

81. A. J. Melmi . J. Carroll, J. Vac. Sci. Technol. A2, 1388 (1984)

82. J. Garnaes, F. Kragh, K. A. Morch, and A. R. Thölén, J. Vac. Sci. Technol. A8 (1), 441 (1990)

83. A. Cricenti, E. Paparazzo, M. A. Scarselli, L. Moretto, and S. Selci, Rev. Sci. Instrum. 65 (5), 1558 (1994)

84. L. A. Hockett and S. E. Creager, Rev. Sci. Instrum. 64 (1), 263 (1993)

85. D. Keller, D. Deputy, A. Alduino and K. Luo, Ultramicroscopy, 42-44, 1481 (1992)

86. D. J. Keller and C. C. Chou, Surf. sci , 268, 333 (1992)

87. G. Rohrer, Scanning Tunneling Microscopy and Spectroscopy, Eds. D. A. Bonnell, VCH publishers, NY (1993), pg155

88. S. Chiang and R. J. Wilson, IBM J. Res. Develop 30, 515 (1986)

89. R. J. Colton, S. M. Baker, J. D. Baldeschwieler, and W. J. Kaiser, Appl. Phys. Lett. 51 (5), 305 (1987)

90. M. Yata, M. Ozaki, S. Sakata, T. Yamada, A. Kohno, and M. Aono, Jpn. J. Appl. Phys. 28 (5), L885 (1989)

91. M. J. Heben, M. M. Dovek, N. S. Lewis, R. M. Penner, and C. F. Quate, J. Microsc. 152, 651 (1988)

92. Vu Thien Binh, J. Microsc. 152, 355 (1988)

93. G. A. Fried, X. D. Wang, and K. W. Hipps, Rev. Sci. Instrum. 64 (6), 1495 (1993)

94. C. A. Lang, J. K. H. Horber, T. W. Hansch, W. M. Heckl, and H. Mohwald, J. Vac. Sci. Technol. A6, 368 (1988)

95. M. J. Heben, R. M. Penner, N. S. Lewis, M. M. Dovek, and C. F. Quate, Appl. Phys. Lett. 54 (15), 1421 (1989)

96. J. S. Villarrubia, Surf. Sci., 321, 287 (1994)

97. V. V. Efremov, P. N. Louskinovich and V. I. Nikishin, Ultramicroscopy, 42-44, 1459 (1992)

98. R. Chicon, M. Ortuno and J. Abellan, Surf. Sci. 181, 107 (1987)

99. Ph. Niedermann and O. Fischer, J. Micros. 152 (1), 93 (1988)

100. G. Reiss, F. Schneider, J. Vancea, and H. Hoffmann, Appl. Phys. Lett. 57 (9), 867 (1990)

101. D. Keller, Surf. Sci. 253, 353 (1991)

102. D. J. Keller and F. S. Franke, Surf. Sci., 294, 409 (1993)

103. A. Baratoff, Physica, B127, 143 (1984)

104. J. Wintterlin, J. Wiechers, H. Brune, T. Gritsch, H. Höfer and R. J. Belm, Phys. Rev. lett., 62, 59 (1989)

105. R. J. Belm, Scanning Tunneling Microscopy and related Methods, Eds. R. J. Belm, N. Garcia and H. Rohrer, Kluwer, Dordrecht, (1990), pg ?

106. V. Linnik, Nature, 123, 946 (1929)

107. O. Enea, M. Rafai and A. Naudon, Ultramicroscopy, 42-44, 572 (1992)

108. T. S. Lin and Y. W. Chung, Superlattices and Microstructure, 4, 709 (1988)

109. J. Vancea, G. Reiss, F. Schneider, K. Bauer and H. Hoffmann, Surf. Sci., 218, 108 (1989)

110. J. A. Derose, D. B. Lampner, S. M. Lindsay, and N. J. Tao, J. Vac. Sci. Technol., A11, 776 (1993)

111. B. Marchon, S. Ferrer, D. S. Kaufman and M. Salmeron, W. Siekhaus, Thin Solid Films, 154, 65 (1987)

112. A. Putnam, B. L. Blackford, M. H. Jericho, and M. O. Watanabe, Surf. Sci., 217, 276 (1989)

113. C. D. E. Chidsey, D. N. Loiacono, T. Sleator and S. Nakahara, Surf. Sci., 200, 45 (1988)

114. S. Buchholz, H. Fuchs, J. P. Rabe, J. Vac. Sci. Technol., B9, 857 (1991)

115. E. H. Moritz, J. Gordon II, G. Borges, and R. Sonnenfeld, Langmuir, 7, 301 (1991)

116. M. Salmeron, D. S. Kaufman, B. Marchon and S. Ferrer, Appl. Surf. Sci., 28, 279 (1987)

117. J. Hwang and M. A. dutson, J. Appl. Phys., 72, 1852 (1992)

118. T. S. Lin and Y. W. Chung, Surf. Sci., 207, 539 (1989)

119. D. Porath, Y. Goldstein, A. Grayevsky and O. Millo, Surf. Sci., 321, 81 (1994)

120. R. Laiho, T. Levola and H. Snellman, Surf. Sci., 181, 370 (1987)

121. G. Mathieu, R. Contini, J. M. Layet, P. Mathiez and S. Giorgio, J. Vac. Sci. Technol., A6, 2904 (1988)

122. A. Hammiche, R. P.Webb, and I. H. Wilson, Vacuum, 45, 569 (1994)

123. R. Bartlett, H. Jaeger, B. A. Sexton, R. P. Netterfield and P. J. Martin, Appl. Surf. Sci., 47, 187 (1991)

124. M. Phaner, G. Stremsdoerfer, Y. W. Li, J. R. Martin, C. de Villeneuve, and L. Porte, J. Electrochem. Soc., 138, 874 (1991)

125. D. G. Ivey, R. Bruce and G. R. Piercy, J. Elctron. Mat., 17, 373 (1988)

126. D. G. Ivey and G. R. Piercy, J. Elect. Microsc. Tech., 8, 233 (1988)

127. Ping Jian, Interfacial Structures And Electrical Properties In Pd-Based Metallization to N-Type InP, 1993

128 B. Pecz, R. Verese gyhazy, G. Radoczi, A. Barna, I. Mojzes, O. Geszti, and Gy. Vincze, J. Appl. Phys., 70, 332 (1991)

129. A. Piotrowska, P. Auvray, A. Guivarc'h, G. Pelous, and P. Henoc, J. Appl. Phys., 52, 5112 (1981)

130. N. S. Fatemi and V. G. Weizer, J. Appl. Phys., 65, 2111 (1989)

131. D. G. Ivey and P. Jian, Can. Metallurgical Quarterly, 34, 85 (1995)

132. W. G. Spitzer, C. R. Crowell, and M. M. Atalla, Phys. Rev. Lett., 8, 57 (1962)

133. C. R. Crowell, W. G. Spitzer, and H. G. While, Appl. Phys. Lett., 1, 3 (1962)

134. M. P. Seah and W. A. Dench, Surf. Interface Anal., 1, 2 (1979)

135. A. E. Fowell, R. H. Williams, B. E. Richardson, A. A. Cafolla, D. I. Westwood, and D. A. Woolf, J. Vac. Sci. Technol., B9, 581 (1991)

136. L. D. Bell, W. J. Kaiser, M. H. Hecht, and L. C. Davis, Scanning Tunneling Microscopy, Eds. J. A. Stroscio and W. J. Kaiser, Acad. Press, CA (1993), pg307

137. A. Bauer, M. T. Cuberes, M. Prietsch, and G. Kaindl, J. Vac. Sci. Technol., B11, 1584 (1993)

138. J. G. Simmons, J. Appl. Phys., 34, 1793 (1963)

139. D. Bohm, Quantum Theory, Prentice-Hall, Englewood Cliffs, 1966

140. C. R. Crowell and S.M. Sze, Physics of the Thin Films, 4, 325 (1967)

141. C. R. Crowell and S. M. Sze, Solid State Electron., 8, 673 (1965)

142. S. Gasiorowicz, Quantum Physics, John Wiley, New York, 1974

143. E. A. Eklund, P. D. Kirchner, D. K. Shuh, F. R. McFeely, and E. Cartier, Phys. Rev. lett., 68, 831 (1992)

144. L. J. Schowalter and E. Y. Lee, Phys. Rev., B43, 9308 (1991)

145. M. Prietsch and R. Ludeke, Surf. Sci., 251/252, 413(1991)

146. M. Prietsch and R. Ludeke, Phys. Rev. Lett., 66, 2511 (1991)

147. R. Ludeke, M. Prietsch, and A. Samsavar, J. Vac. Sci. Technol., B9, 2342 (1991)

148. M. D. Stiles and D. R. Hamann, J. Vac. Sci. Technol., B9, 2394 (1991)

170

149. M. D. Stiles and D. R. Hamann, Mater. Sci. and Eng., B14, 291 (1992)

150. M. H. Hecht, L. D. Bell, and W. J. Kaiser, Phys. Rev., B42, 7663 (1990)

151. S.M. Sze, Physics of Semiconductor Devices, 2nd ed., John Wiley, New York, 1981

152. M. H. Hecht, L. D. Bell, W. J. Kaiser, and L. C. Davis, Phys. Rev., B42, 7663 (1990)

153. L. J. Brillson, Surf. Sci. Rep., 2, 123 (1982)

154. J. S. Blakemore, J. Appl. Phys., 53, R123 (1982)

155. R. H. Williams, Appl. Surf. Sci., 70/71, 386 (1993)

156. M. H. Hecht, L. D. Bell, W. J. Kaiser, Appl. Surf. Sci., 41/42, 17 (1989)

157. A. Fernadez, H. D. Hallen, T. Huang, R. A. Buhrman, and J. Silcox, Appl. Phys. Lett., 57, 2826 (1990)

158. H. D. Hallen, A. Fernadez, T. Huang, R. A. Buhrman, and J. Silcox, J. Vac. Sci. Technol., B9, 585 (1991)

159. E. Y. Lee, B. R. Turner, L. J. Schowalter, and J. R. Jimenez, J. Vac. Sci. Technol., B11, 1579 (1993)

160. W. J. Kaiser, L. D. Bell, M. H. Hecht, F. J. Grunthaner, J. Vac. Sci. Technol., B7, 945 (1989)

161. P. W. Chye, I. Lindan, P. Pianetta, C. M. Garner, C. Y. Su and W. E. Spicer, Phys. Rev., B18, 5545 (1978)

162. J. L. Freeouf and J. M. Woodall, Appl. Phys. Lett., 39, 727 (1981)

163. W. J. Kaiser, L. D. Bell, M. H. Hecht, and F. J. Grunthaner, J. Vac. Sci. Technol., B7, 945 (1989)

164. R. Ludeke, A. B. Mclean, and A. Taleb-Ibrahimi, Phys. Rev., B42, 2982 (1990)

165. S. Saitch, H. Ishiwara, and S. Furukawa, Appl. Phys. Lett., 37, 203 (1980)

166. R. T. Tung, J. M. Gibson, and J. M. Poate, Phys. Rev. Lett., 50, 429 (1983)

167. E. Vlieg, A. E. M. J. Fischer, J. F. Van der Veen, B. N. Dev, and G. Materlik, Surf. Sci., 178, 36 (1986)

168. L. F. Mattheiss and D. R. Hamann, Phys. Rev., B37, 10623 (1988)

169. W. J. Kaiser, M. H. Hecht, R. W. Fathauer, L. D. Bell, E. Y. Lee, and L. C. Davis, Phys. Rev., B44, 6546 (1991)

170. J. C. Hensel, A. F. J. Levi, R. T. Tung, and J. M. Gibson, Appl. Phys. Lett., 47, 151 (1985)

171. J. Y. Duboz, P. A. Badoz, F. Arnaud d'Avitaya and E. Rosencher, Phys. Rev., B40, 10607 (1989)

172. R. T. Tung, Phys. Rev. Lett., 52, 461 (1984)

173. A. Fernandez, H. D. Hallen, T. Huang, R. A. Buhrman, and J. Silcox, J. Vac. Sci. Technol., B9, 590 (1991)

174. E. Hokelek and G. Y. Robinson, Appl. Phys. Lett., 40, 426 (1982)

174. D. G. Ivey, D. Wang and P. Jian, Experimental Methods of Phase Diagram Determination, Eds J. E. Morral, R. S. Schiffman and S. M. Merchant, The Minerals, Metals & Materials Soc. (1994), pg151

175. T. Sands, C. C. Chang, A. S. Kaplan, V. G. Keramidas, K. M. Krishnan, and J. Washburn, Appl. Phys. Lett., 50, 1346 (1987)

Appendix 1. Setup of the Control Forms

```
Function GetVal3 (Inum As Integer) As Integer
        Dim Mess As String
        AMP = Chr (38)
        CAPH = Chr (72)
        Mess = Hex$ (Inum)
        Mess = Left$ (Mess, 3)
        Mess = AMP & CAPH & Mess
        GetVal3 = Val (Mess)
End  Function


Function PutVal (Inum As Integer) As Long
        Dim Mess As String
        AMP = Chr (38)
        CAPH = Chr (72)
        ZERO = Chr (48)
        Mess = Hex$ (Inum)
        Mess = Right$ (Mess, 3)
        Mess = AMP & CAPH & ZERO & Mess & ZERO
        PutVal3 = Val (Mess)
End  Function


Sub  Bias_Change ()
     Update_Bias = 0
End  Sub


Sub  Command1_Click ()
        Dim Result
```

```
Const OFN_HIDERO = &H4&
Const OFN_EXTDIF = &H400&
' Open data file if necessary
If FileFlag1 = 0 Then
        CMDialog1.Flags = OFN_HIDERO        or OFN_EXTDIF
        CMDialog1.Action = 1
        Open CMDialog1.Filename For Append As #1
        FileFlag1 = 1
End If
    ' Open raw data file if necessary
If FileFlag2 = 0 Then
        CMDialog2.Flags = OFN_HIDERO or OFN_EXTDIF
        CMDialog2.Action = 1
        Open CMDialog2.Filename For Append As #2
        FileFlag1 = 1
End If
If Update_Bias = 0 Then
        Result = Msgbox ("Update Bias?", 36, "TIP BIAS")
        If Result = 6 Then
                Command6_Click
        End If
End If


If Update_Filter = 0 Then
        Result = Msgbox ("Update Filter?", 36, "FILTER OFFSET")
        If Result = 6 Then
                Command7_Click
        End If
End If
```

```
EnD Sub


Sub  Command2_Click ()
    HScroll1.LargeChange = 100
    HScroll1.SmallChange = 20
End  Sub


Sub  Command3_Click ()
    HScroll1.LargeChange = 10
    HScroll1.SmallChange = 1
End  Sub


Sub  Command4_Click ()
    HScroll2.LargeChange = 100
    HScroll2.SmallChange = 20
End  Sub


Sub  Command5_Click ()
    HScroll2.LargeChange = 10
    HScroll2.SmallChange = 1
End  Sub


Sub  Command6_Click ()
    ' Convert Tip Bias Voltage to counts & send
    TDataOut = SetTData + 2048
    TDataOut = TDataOut x 16
    ' Ramp to desired value (soon!)
    daserr = K_DAWrite (DevHandle, 0, TDataOut)
    If daserr <> 0 Then
```

```
        MsgBox "K_ADWrite Error" + Hex$ (daserr), 16, "DAS-1600 Error"
        End
End If
Update_Bias = 1
For I = 1 To 10000: Next I
'Get the set value
daserr = K_ADRead (DevHandle, 0, 2, MyCnt)
If daserr <> 0 Then
        MsgBox "K_ADRead Error" + Hex$ (daserr), 16, "DAS-1600 Error"
        End
End If
MyCnt = GetVal3 (MyCnt)
tbvolt = (((MyCnt - 2048#) x span4) / 4096#) x 1000#
Lable5.Caption = Cstr (tbvolt)
End  Sub


Sub  Command7_Click ()
        ' Convert Filter Offset Voltage to counts & send
        FDataOut = Int (SetFData x 0.4096) + 2048
        FDataOut = FDataOut x 16
        daserr = K_DAWrite (DevHandle, 1, FDataOut)
        If daserr <> 0 Then
                MsgBox "K_ADWrite Error" + Hex$ (daserr), 16, "DAS-1600 Error"
                End
        End If
        Update_Filter = 1
        For I = 1 To 50000: Next I
        ' Convert filter Offset to mV
        daserr = K_ADRead (DevHandle, 4, 1, MyCnt)
```

```
            If daserr <> 0 Then

                    MsgBox "K_ADRead Error" + Hex$ (daserr), 16, "DAS-1600 Error"

                    End

            End If

            MyCnt = GetVal3 (MyCnt)

            fovolt = (((MyCnt - 2048#) x span2) / 4096#) x 1000#

            Lable6.Caption = Cstr (fovolt)

End  Sub


Sub  Filter_Change ()

            Update_Filter = 0

End  Sub


Sub  Form_Load ()

            Update_Bias = 1

            update_Filter = 1

End  Sub


Sub  Scroll1_Change ()

            Bias.Caption = HScroll1.Value

            SetTData = Val (HScroll1.Value)

End  Sub


Sub  Scroll2_Change ()

            Filter.Caption = HScroll2.Value

            SetFData = Val (HScroll2.Value)

End  Sub


Sub  Scroll3_Change ()
```

```
        Lable4.Caption = HScroll3.Value
        Form1.Lable4.Caption = HScroll3.Value
        BeeCount = Val (HScroll3.Value)
End  Sub
```

.

Appendix 2. Setup of the Form Text

Begin Form Form1

BackColor	=	&H00FF8080&
Caption	=	"Ballistic Emission Acquisition"
ClientHeight	=	6288
ClientLeft	=	72
ClientTop	=	1368
ClientWidth	=	9288
ClipControls	=	0 'False
Height	=	7032
Left	=	24
LinkTopic	=	"Form1"
ScaleHeight	=	432
ScaleWidth	=	432
Top	=	672
Width	=	9384

Begin CommandButton Command5

Caption	=	"Stop BEES"
Height	=	732
Left	=	7080
TabIndex	=	24
Top	=	3360
Width	=	1212

End

Begin Timer Timer1

Enabled	=	0 'False

```
            Left          =      8760

            Top           =      1080

End

Begin GRAPH graph1

            Bachground    =      7      'Light Gray

            BottomTitle   =      "Point Number"

            GraphCaption  =      "BEES (Filtered)"

            GraphTitle    =      "FILTERED BEES DATA (Volts)"

            GraphType     =      6      'Line

            Height        =      2892

            LabelEvery    =      5

            Left          =      360

            NumPoints     =      30

            RandomData    =      0      'Off

            TabIndex      =      18

            ThickLines    =      0      'Off

            Top           =      3240

            Width         =      6372

End

Begin CommandButton Command4

            Caption       =      "CLOSE FILES"

            Height        =      492

            Left          =      6720

            TabIndex      =      21

            Top           =      2640

            Width         =      1932

End

Begin CommandButton Command3

            Caption    .  =      "SAVE"
```

```
        Height        =    492

        Left          =    4800

        TabIndex      =    20

        Top           =    2640

        Width         =    1932

End

Begin CommandButton Command2

        Caption       =    "READ BEES"

        Height        =    492

        Left          =    6720

        TabIndex      =    19

        Top           =    2160

        Width         =    1932

End

Begin Frame Frame 2

        BackColor     =    &H00C0C0C0&

        Caption       =    "BEES Info"

        ForeColor     =    &H00FFFFFF&

        Height        =    1932

        Left          =    4800

        TabIndex      =    13

        Top           =    120

        Width         =    3852

        Begin Label Label17

             Alignment     =    2 'Center

             BackColor     =    &H0080FFFF&

             Caption       =    "0"

             Height        =    252

             Left          =    2280
```

TabIndex	=	23
Top	=	1080
Width	=	1332

End

Begin Label Label16

BackColor	=	&H0080FFFF&
Caption	=	"Samples Read"
Height	=	252
Left	=	240
TabIndex	=	22
Top	=	1080
Width	=	1812

End

Begin Label Label14

Alignment	=	2 'Center
BackColor	=	&H0080FFFF&
Caption	=	"30"
Height	=	252
Left	=	2280
TabIndex	=	17
Top	=	600
Width	=	1332

End

Begin Label Label15

Alignment	=	2 'Center
BackColor	=	&H0080FFFF&
Caption	=	"0"
Height	=	252
Left	=	2280

```
        TabIndex      =    16

        Top           =    1560

        Width         =    1332

End

Begin Label Label13

        BackColor     =    &H0080FFFF&

        Caption       =    "Average"

        Height        =    252

        Left          =    240

        TabIndex      =    15

        Top           =    1560

        Width         =    1812

End

Begin Label Label12

        BackColor     =    &H0080FFFF&

        Caption       =    "Number of Samples"

        Height        =    252

        Left          =    240

        TabIndex      =    14

        Top           =    600

        Width         =    1812

    End

End

Begin CommandButton Command1

    Caption      =    "READ INPUTS"

    Height       =    492

    Left         =    4800

    TabIndex     =    12

    Top          =    2160
```

```
            Width          =   1932
End
Begin Frame Frame1
        BackColor      =   &H00C0C0C0&
        Caption        =   "Analog Inputs"
        Height         =   3012
        Left           =   360
        TabIndex       =   0
        Top            =   120
        Width          =   4092
        Begin Label Label11
            Alignment      =   2   'Center
            BackColor      =   &H00C0C0C0&
            Caption        =   " (mV) "
            Height         =   255
            Left           =   2400
            TabIndex       =   11
            Top            =   240
            Width          =   1215
        End
        Begin Label Label10
            Alignment      =   2   'Center
            BackColor      =   &H0080FFFF&
            Caption        =   "0"
            Height         =   255
            Left           =   2160
            TabIndex       =   10
            Top            =   2520
            Width          =   1695
```

End

Begin Label Label9

    Alignment   =   2   'Center

    BackColor   =   &H0080FFFF&

    Caption   =   "0"

    Height   =   255

    Left   =   2160

    TabIndex   =   9

    Top   =   2040

    Width   =   1695

End

Begin Label Label8

    Alignment   =   2   'Center

    BackColor   =   &H0080FFFF&

    Caption   =   "0"

    Height   =   255

    Left   =   2160

    TabIndex   =   8

    Top   =   1560

    Width   =   1695

End

Begin Label Label7

    Alignment   =   2   'Center

    BackColor   =   &H0080FFFF&

    Caption   =   "0"

    Height   =   255

    Left   =   2160

    TabIndex   =   7

    Top   =   1080

```
        Width          =   1695
End
    Begin Label Label6
    Alignment      =   2    'Center
    BackColor      =   &H0080FFFF&
    Caption        =   "0"
    Height         =   255
    Left           =   2160
    TabIndex       =   6
    Top            =   600
    Width          =   1695
End
    Begin Label Label5
    BackColor      =   &H0080FFFF&
    Caption        =   "Filtered Offset"
    Height         =   255
    Left           =   240
    TabIndex       =   5
    Top            =   2520
    Width          =   1695
End
Begin Label Label4
        BackColor      =   &H0080FFFF&
        Caption        =:  "Tunneling Current"
        Height         =   255
        Left           =   240
        TabIndex       =   4
        Top            =   2040
        Width          =   1695
```

End

Begin Label Label3

    BackColor   =   &H0080FFFF&

    Caption   =   "BEES filtered"

    Height   =   255

    Left   =   240

    TabIndex   =   3

    Top   =   1560

    Width   =   1695

End

Begin Label Label2

    BackColor   =   &H0080FFFF&

    Caption   =   "BEES raw"

    Height   =   255

    Left   =   240

    TabIndex   =   2

    Top   =   1080

    Width   =   1695

End

Begin Label Label1

    BackColor   =   &H0080FFFF&

    Caption   =   "Tip Bias"

    Height   =   252

    Left   =   240

    TabIndex   =   1

    Top   =   600

    Width   =   1692

End

End

```
Begin Menu InitParams
        Caption        =   "Parameters"
        Index          =   1
    End
End



Begin Form Form2
        Caption         =       "Setup"
        ClientHeight    =       2868
        ClientLeft      =       1680
        ClientTop       =       2688
        ClientWidth     =       6480
        Height          =       3288
        Left            =       1632
        LinkTopic       =       "Form2"
        ScaleHeight     =       2868
        ScaleWidth      =       6480
        Top             =       2316
        Visible         =       0           'False
        Width           =       6576
        Begin Frame Frame1
            BackColor       =       &H000080FF&
            Caption         =       "ACQUISITION PARAMETERS"
            ForeColor       =       &H00FFFFFF&
            Height          =       2892
            Left            =       0
            TabIndex        =       0
            Top             =       0
```

```
Width            =    6492
Begin CommonDialog CMDialog2
    DefaultExt     =    "raw"
    DialogTitle    =    "Raw BEES Data"
    Filter         =    "raw File (*.raw) | *.raw"
    Left           =    600
    Top            =    1680
End
Begin CommonButton Command7
    Caption        =    "Update Filter"
    Height         =    492
    Left           =    4800
    TabIndex       =    16
    Top            =    1560
    Width          =    1332
End
    Begin CommonButton Command6
    Caption        =    "Update Bias"
    Height         =    492
    Left           =    4800
    TabIndex       =    15
    Top            =    1560
    Width          =    1332
End
Begin CommonDialog CMDialog1
    DefaultExt     =    "dat"
    DialogTitle    =    "Data File"
    Filter         =    "Data File (*.dat) | *.dat"
    Left           =    600
```

189

```
        Top           =    720
End
Begin Hscrollbar Hscroll3
        Height        =    255
        LargeChange   =    10
        Left          =    1920
        Max           =    200
        TabIndex      =    14
        Top           =    2400
        Width         =    2655
End
Begin CommandButton Command5
        Caption       =    "Fine"
        Height        =    255
        Left          =    3240
        TabIndex      =    11
        Top           =    1800
        Width         =    1335
End
Begin CommandButton Command4
        Caption       =    "Course"
        Height        =    255
        Left          =    1920
        TabIndex      =    10
        Top           =    1800
        Width         =    1335
End
Begin CommandButton Command3
        Caption       =    "Fine"
```

Height	=	255
Left	=	3240
TabIndex	=	9
Top	=	840
Width	=	1335

End

Begin CommandButton Command2

Caption	=	"Course"
Height	=	255
Left	=	1920
TabIndex	=	8
Top	=	840
Width	=	1335

End

Begin CommomButton Command1

Caption	=	"DONE"	
FontBold	=	-1	'Ture
FontItalic	=	0	'False
FontName	=	"MS Sans Serif"	
FontSize	=	12	
FontStrikethru	=	0	'False
FontUnderline	=	0	'False
Height	=	492	
Left	=	4800	
TabIndex	=	7	
Top	=	2160	
Width	=	1332	

End

Begin Hscrollbar Hscroll1

```
            Height        =    255

            LargeChange   =    100

            Left          =    1920

            Max           =    2048

            Min           =    -2048

            SmallChange   =    20

            TabIndex      =    2

            Top           =    600

            Width         =    2655
End

Begin Hscrollbar Hscroll2

            Height        =    255

            LargeChange   =    100

            Left          =    1920

            Max           =    2500

            Min           =    -2500

            SmallChange   =    20

            TabIndex      =    1

            Top           =    1560

            Width         =    2655
End

Begin Label Label6

            Alignment     =    2    'Center

            BackColor     =    &H008080FF&

            BorderStyle   =    1    'Fixed single

            Caption       =    "0"

            Height        =    252

            Left          =    4800

            TabIndex      =    18
```

Top	=	1320
Width	=	1332

End

Begin Label Label5

Alignment	=	2 'Center
BackColor	=	&H008080FF&
BorderStyle	=	1 'Fixed single
Caption	=	"0"
Height	=	252
Left	=	4800
TabIndex	=	17
Top	=	360
Width	=	1332

End

Begin Label Label4

Alignment	=	2 'Center
BackColor	=	&H00FFFF80&
BorderStyle	=	1 'Fixed single
Caption	=	"0"
Height	=	255
Left	=	1920
TabIndex	=	13
Top	=	2160
Width	=	2655

End

Begin Label Label3

BackColor	=	&H0000FFFF&
Caption	=	"BEES (filtered) number of samples"
Height	=	375

```
    Left          =    120

    TabIndex      =    12

    Top           =    2160

    Width         =    1695

    WordWrap      =    -1  'True
End

Begin Label Label1

    Alignment     =    2    'Center

    BackColor     =    &H0000FFFF&

    Caption       =    "Tip Bias (mV)"

    Height        =    255

    Left          =    120

    TabIndex      =    6

    Top           =    360

    Width         =    1335
End

Begin Label Bias

    Alignment     =    2    'Center

    BackColor     =    &H00FFFF00&

    BorderStyle   =    1    'Fixed single

    Caption       =    "0"

    Height        =    255

    Left          =    1920

    TabIndex      =    5

    Top           =    360

    Width         =    2655
End

Begin Label Label2

    BackColor     =    &H0000FFFF&
```

```
            Caption      =     "Filter Offset (mV)"

            Height       =     255

            Left         =     120

            TabIndex     =     4

            Top          =     1320

            Width        =     1455

      End

Begin Label Label6

            Alignment    =     2    'Center

            BackColor    =     &H00FFFF80&

            BorderStyle  =     1    'Fixed single

            Caption      =     "0"

            Height       =     255

            Left         =     1920

            TabIndex     =     3

            Top          =     1320

            Width        =     2655

         End

      End

End
```

Appendix 3. BEES Program

```
Function GetVal2 (Inum As Integer) As Integer
        Dim Mess As String
        AMP = Chr (72)
        Mess = Hex$ (Inum)
        Mess = Left$ (Mess, 3)
        Mess = AMP & CAPH & Mess
        GetVal2 = Val (Mess)
End Function


Sub Command1_Click ()


        ' Convert Tip Bias to mV
        daserr = K_ADRead (Devhandle, 0, 2, MyCnt)
        If daserr <> 0 Then
                MsgBox "K_ADread Error" + Hex$ (daserr), 16, "DAS-1600 Error"
                End
        End If
        MyCnt = GetVal2 (MyCnt)
        tbvolt = (((MyCnt - 2048#) x span4) / 4096#) x 1000#
        Label6.Caption = Cstr (tbvolt)


        ' Convert BEES raw to mV
        daserr = K_ADRead (DevHandle, 1, 0, MyCnt)
        If daserr <> 0 Then
                MsgBox "K_ADRead Error" + Hex$ (daserr), 16, "DAS-1600 Error"
                End
```

End If

MyCnt = GetVal2 (MyCnt)

brvolt = (((MyCnt - 2048#) x span1) / 4096#) x 1000#

Label7.Caption = Cstr (brvolt)

' Convert BEES filtered to mV

daserr = K_ADRead (DevHandle, 2, 0, MyCnt)

If daserr <> 0 Then

    MsgBox "K_ADRead Error" + Hex$ (daserr), 16, "DAS-1600 Error"

    End

End If

MyCnt = GetVal2 (MyCnt)

bfvolt = (((MyCnt - 2048#) x span1) / 4096#) x 1000#

Label8.Caption = Cstr (bfvolt)

' Convert Tunneling Current to mV

daserr = K_ADRead (DevHandle, 3, 0, MyCnt)

If daserr <> 0 Then

    MsgBox "K_ADRead Error" + Hex$ (daserr), 16, "DAS-1600 Error"

    End

End If

MyCnt = GetVal2 (MyCnt)

brvolt = (((MyCnt - 2048#) x span1) / 4096#) x 1000#

Label9.Caption = Cstr (tcvolt)

' Convert Filter Offset to mV

daserr = K_ADRead (DevHandle, 4, 1, MyCnt)

If daserr <> 0 Then

    MsgBox "K_ADRead Error" + Hex$ (daserr), 16, "DAS-1600 Error"

197

```
            End

      End If

      MyCnt = GetVal2 (MyCnt)

      fovolt = (((MyCnt - 2048#) x span2) / 4096#) x 1000#

      Label10.Caption = Cstr (fovolt)


End   Sub


Sub   Command2_Click ()

      ' Turn on Timer

      Timer1.Enabled = 1

      Timer1.Interval =250

End   Sub

Sub   Command3_Click ()

      Print #1, tbvolt, brvolt, bfvolt, tcvolt, fovolt, bavg


      Print #2, BeeCount, bavg

      btot = BeeCount

      If btot < 5 Then

            For I = 1 to btot

                  Print #2, BeeVolt (I), " ";

            Next I

            Print #2,

      Else

            J = 1

            While btot > 5

                  For I = J To J + 4

                        Print #2, BeeVolt (I), " ";

                  Next I
```

198

```
                Print #2
                btot = btot - 5
                J = J + 5
        End
        For J = I to BeeCount
                        Print #2, BeeVolt (I), " ";
        Next I
        Print #2
    End If
End  Sub


Sub  Command4_Click ()
    Close #1
    Close #2
    FileFlag1 = 0
    FileFlag2 = 0
End  Sub


Sub  Command5_Click ()
    Timer1.Enabled = False
    Graph1.DataReset = 1
    BeeStop = 1
Ens  Sub


Sub  Form_Load ()
    ' OPEN & INITIALIZE DREVER & HARDWARE
    daserr  =  DAS1600_DEVOPEN ( "C:\DAS1600\ASOWIN\DAS1600.CFG",
BOARD)
    If dasser <> 0 Then
```

```
            MsgBox "DAS1600_DevOpen Error" + Hex$ (daserr) + ", please specify the
complete path to the configuration file.", 16, "DAS-1600 Error"
            End
      End If
      ' GET HANDLE TO DEVICE
      daserr = DAS1600_GETDEVHANDLE (0, DevHandle)
        If dasser <> 0 Then
            MsgBox "DAS1600_GetDevHandle Error" + Hex$ (daserr), 16, "DAS-1600
Error"
            End
      End If
      'Default value for # of data points
      BeeCount = 30
      'span based on gain for specific channel
      span1 = 20
      span2 = 10
      span3 = 5
      Fileflag = 0
      BeeStop = 0
      ' LOAD SETUP FORM
      LOAD FORM2
End  Sub


Sub  InitParams_Click (Index As Integer)
      Form2.Show
      Form2.Hscroll1.SetFocus
End  Sub


Sub  timer1_Timer ()
```

200

```
Static Bcnt, bsum
If Beestop = 1 Then
        bcnt = 0
        bsum = 0
        BeeStop = 0
End If
Graph1.NumPoints = BeeCount
Bcnt = Bcnt + 1
'Take a reading
daserr = K_ADRead (DevHandle, 2, 0, MyCnt)
If daserr <> 0 Then
        MsgBox "K_ADread Error" + Hex$ (daserr), 16, "DAS-1600 Error"
        End
End If
' Convert BEES filtered to mV
MyCnt = GetVal2 (MyCnt)
BeeVolt (Bcnt) = (((MyCnt - 2048#) x span1) / 4096#) x 1000#
BEEP
Graph1.GraphData = BeeVolt (Bcnt) / 1000
Graph1.DrawMode = 3
Label17.Caption = Str$ (Bcnt)
If Bcnt = BeeCount Then
        ' Calculate the Average & Display
        For I = 1 To BeeCount
                bsum = bsum + BeeVolt (I)
        Next I
        bavg = bsum / BeeCount
        Label15.Caption = Str$ (bavg)
        Bcnt = 0
```

```
            bsum = 0
            graph1.dataReset = 1
            Timer1.Enabled = False
        End If
    End  Sub
```

Appendix 4. Declaration

DAS1600.BAS

Declare Function DAS1600_DEVOPEN Lib "DAS1600.DLL" (ByVal szCfgName$, pNumOfBoards As Integer) As Integer

Declare Function DAS1600_GETDEVHANDLE Lib "DAS1600.DLL" (ByVal nBrdNum As Integer, phDev As Long) As Integer

Declare Function DAS1600_SETSETTLINGTIME Lib "DAS1600.DLL" (ByVal nBrdNum As Integer, ByVal nGain Code As Integer, ByVal nCount As Integer) As Integer

Declare Function DAS1600_SETSETTLINGTIME Lib "DAS1600.DLL" (ByVal nBrdNum As Integer, ByVal nGain Code As Integer, pCount As Integer) As Integer

Declare Function DAS1600_8254CONTROL Lib "DAS1600.DLL" (ByVal nBrdNum As Integer, ByVal nCtrlData As Integer) As   Integer

Declare Function DAS1600_8254SETCOUNTER Lib "DAS1600.DLL" (ByVal nBrdNum As Integer, ByVal nCntr As Integer, ByVal nCntrData As Integer) As Integer

Declare Function DAS1600_8254SETCOUNTER Lib "DAS1600.DLL" (ByVal nBrdNum As Integer, ByVal nCntr As Integer, pCntrData As Integer) As Integer

Declare Function DAS1600_8254SETCLK0 Lib "DAS1600.DLL" (ByVal nBrdNum As Integer, ByVal nClkSrc As Integer) As Integer

Declare Function DAS1600_8254SETCLK0 Lib "DAS1600.DLL" (ByVal nBrdNum As Integer, pClkSrc As Integer) As Integer

Declare Function DAS1600_8254SETTRIG0 Lib "DAS1600.DLL" (ByVal nBrdNum As Integer, ByVal nTrigEnable As Integer) As Integer

Declare Function DAS1600_8254SETTRIG0 Lib "DAS1600.DLL" (ByVal nBrdNum As Integer, pTrigEnable As Integer) As Integer

DASDECL.BAS

Declare Function K_ADRead Lib "DASSELL.DLL" (ByVal hDev As Long, ByVal
    nChan As Integer. ByVal nGain As Integer, pData As Integer) As Integer

Declare Function K_BufListReset Lib "DASSELL.DLL" (ByVal hFrame As Long,
    ByVal pBuf As Long, ByVal dwSize As Long) As Integer

Declare Function K_BufListReset Lib "DASSELL.DLL" (ByVal hFrame As Long) As
    Integer

Declare Function K_ClearFrame Lib "DASSELL.DLL" (ByVal hFrame As Long) As
    Integer

Declare Function K_CloseAllDriverHandles Lib "DASSELL.DLL" () As Integer

Declare Function K_CloseDriver "DASSELL.DLL" (ByVal hDrv As Long) As Integer

Declare Function K_ClrAboutTrig Lib "DASSELL.DLL" (ByVal hFrame As Long) As
    Integer

Declare Function K_ClrADFreeRun Lib "DASSELL.DLL" (ByVal hFrame As Long) As
    Integer

Declare Function K_ClrContRun Lib "DASSELL.DLL" (ByVal hFrame As Long) As
    Integer

Declare Function K_DASDevInit Lib "DASSELL.DLL" (ByVal hDev As Long) As
    Integer

Declare Function K_DAWrite Lib "DASSELL.DLL" (ByVal hDev As Long, ByVal
    nChan As Integer, ByVal dwData As Integer) As Integer

Declare Function K_DIRead Lib "DASSELL.DLL" (ByVal hDev As Long, ByVal
    nChan As Integer, pData As Any) As Integer

Declare Function K_DMAAlloc Lib "DASSELL.DLL" (ByVal hFrame As Long, ByVal
    dwSamples As Long, pBuf As Long, phMem As Integer) As Integer

Declare Function K_DMAFree Lib "DASSELL.DLL" (ByVal hMem As Integer) As
    Integer

Declare Function K_DMAStart Lib "DASSELL.DLL" (ByVal hFrame As Long) As
Integer

Declare Function K_DMAStatus Lib "DASSELL.DLL" (ByVal hFrame As Long,
pStatus As Integer, pCount As Long) As Integer

Declare Function K_DMAStop Lib "DASSELL.DLL" (ByVal hFrame As Long, pStatus
As Integer, pCount As Long) As Integer

Declare Function K_DOWrite Lib "DASSELL.DLL" (ByVal hDev As Long, ByVal
nChan As Integer, ByVal dwData As Long) As Integer

Declare Function K_FormatChanGAry Lib "DASSELL.DLL" Alias
"K_FormatChnGAry" (pArray As Integer) As Integer

Declare Function K_FormatChanGAry Lib "DASSELL.DLL" (pArray As Integer) As
Integer

Declare Function K_FreeDevHandle Lib "DASSELL.DLL" (ByVal hDev As Long) As
Integer

Declare Function K_FreeFrame Lib "DASSELL.DLL" (ByVal hFrame As Long) As
Integer

Declare Function K_GetAboutTrig Lib "DASSELL.DLL" (ByVal hFrame As Long,
pSamples As Long) As Integer

Declare Function K_GetADCommonMode Lib "DASSELL.DLL" (ByVal hDev As
Long, pMode As Integer) As Integer

Declare Function K_GetADConfig Lib "DASSELL.DLL" (ByVal hDev As Long,
pMode As Integer) As Integer

Declare Function K_GetADFrame Lib "DASSELL.DLL" (ByVal hDev As Long,
phFrame As Long) As Integer

Declare Function K_GetADFreeRun Lib "DASSELL.DLL" (ByVal hFrame As Long,
pStatus As Integer) As Integer

Declare Function K_GetADMode Lib "DASSELL.DLL" (ByVal hDev As Long, pMode
As Integer) As Integer

Declare Function K_GetADTrig Lib "DASSELL.DLL" (ByVal hFrame As Long,
    pOpt   As Integer, pChan As Integer, pLevel As Long) As Integer

Declare Function K_GetBuf Lib "DASSELL.DLL" (ByVal hFrame As Long, pBuf As
    Long, pSamples As Long) As Integer

Declare Function K_GetBufB Lib "DASSELL.DLL" (ByVal hFrame As Long, pBuf As
    Long, pSamples As Long) As Integer

Declare Function K_GetBurstTicks Lib "DASSELL.DLL" (ByVal hFrame As Long,
    pTicks As Integer) As Integer

Declare Function K_GetChn Lib "DASSELL.DLL" (ByVal hFrame As Long, pChan As
    Integer) As Integer

Declare Function K_GetChnGary Lib "DASSELL.DLL" (ByVal hFrame As Long,
    pArray As Long) As Integer

Declare Function K_GetClk Lib "DASSELL.DLL" (ByVal hFrame As Long, pMode As
    Integer) As Integer

Declare Function K_GetClkRate Lib "DASSELL.DLL" (ByVal hFrame As Long, pRate
    As Long As Long) As Integer

Declare Function K_GetContRun Lib "DASSELL.DLL" (ByVal hFrame As Long,
    pMode As integer) As Integer

Declare Function K_GetDAFrame Lib "DASSELL.DLL" (ByVal hDev As Long,
    phFrame As Long) As Integer

Declare Function K_GetDevHandle Lib "DASSELL.DLL" (ByVal hDrv As Long,
ByVal pBrdNum As Integer, phDev As Long) As Integer

Declare Function K_GetDIFrame Lib "DASSELL.DLL" (ByVal hDev As Long,
phFrame   As Long) As Integer

Declare Function K_GetDITrig Lib "DASSELL.DLL" (ByVal hFrame As Long, pOpt As
    Integer, pChan As Integer, pPattern As Long) As Integer

Declare Function K_GetDOCurval Lib "DASSELL.DLL" (ByVal hFrame As Long,
    pValue As Long) As Integer

206

Declare Function K_GetDOFrame Lib "DASSELL.DLL" (ByVal hDev As Long, phFrame As Long) As Integer

Declare Function K_GetExtClkEdge Lib "DASSELL.DLL" (ByVal hFrame As Long, pMode As Integer) As Integer

Declare Function K_GetG Lib "DASSELL.DLL" (ByVal hFrame As Long, pGain As Integer) As Integer

Declare Function K_GetGate Lib "DASSELL.DLL" (ByVal hFrame As Long, pMode As Integer) As Integer

Declare Function K_GetSecondAddr Lib "DASSELL.DLL" (ByVal hMem As Long, pBuf As Long) As Integer

Declare Function K_GetPreTrig Lib "DASSELL.DLL" (ByVal hFrame As Long, pCount As Integer) As Integer

Declare Function K_GetShellVer Lib "DASSELL.DLL" (pVersion As Integer) As Integer

Declare Function K_GetSSH Lib "DASSELL.DLL" (ByVal hFrame As Long, pMode As Integer) As Integer

Declare Function K_GetStartStopChn Lib "DASSELL.DLL" (ByVal hFrame As Long, pStart As Integer, pStop As Integer) As Integer

Declare Function K_GetStartStopG Lib "DASSELL.DLL" (ByVal hFrame As Long, pStart As Integer, pStop As Integer, pGain As Integer) As Integer

Declare Function K_GetSync Lib "DASSELL.DLL" (ByVal hFrame As Long, pMode As Integer) As Integer

Declare Function K_GetTrig Lib "DASSELL.DLL" (ByVal hFrame As Long, pMode As Integer) As Integer

Declare Function K_GetTrigHyst Lib "DASSELL.DLL" (ByVal hFrame As Long, pHyst As Integer) As integer

Declare Function K_GetTrigOut Lib "DASSELL.DLL" (ByVal hFrame As Long, pMode As Integer, pTics As Long) As Integer

Declare Function K_GetVer Lib "DASSELL.DLL" (ByVal hDev As Long, pSpecVer As
    Integer, pDrvVer As Integer) As Integer

Declare Function K_InitFrame Lib "DASSELL.DLL" (ByVal hFrame As Long) As
    Integer

Declare Function K_IntAlloc Lib "DASSELL.DLL" (ByVal hFrame As Long, ByVal
    dwSamples As Long, pBuf As Long, phMem As Integer) As Integer

Declare Function K_IntFree Lib "DASSELL.DLL" (ByVal hMem As Integer) As Integer

Declare Function K_IntStartLib "DASSELL.DLL" (ByVal hFrame As Long) As Integer

Declare Function K_IntStatus Lib "DASSELL.DLL" (ByVal hFrame As Long, pStatus
    As Integer, pCount As Long) As Integer

Declare Function K_IntStop Lib "DASSELL.DLL" (ByVal hFrame As Long, pStatus
    As Integer, pCount As Long) As Integer

Declare Function K_MoveArrayToBuf Lib "DASSELL.DLL" Alias "K_MoveDataBuf"
    (pDest As Integer, ByVal hSource As Long, ByVal nCount As Integer) As Integer

Declare Function K_MoveDataBuf Lib "DASSELL.DLL" (pDest As Integer, ByVal
    hSource As Long, ByVal nCount As Integer) As Integer

Declare Function K_OBMDataMove Lib "DASSELL.DLL" (ByVal hFrame As Long)
As   Integer

Declare Function K_OBMGetAddressStep Lib "DASSELL.DLL" (ByVal hFrame As
    Long, pStep As Integer) As Integer

Declare Function K_OBMGetChanAry Lib "DASSELL.DLL" (ByVal hFrame As Long,
    pArray As Integer) As Integer

Declare Function K_OBMGetMode Lib "DASSELL.DLL" (ByVal hFrame As Long,
    pMode As Integer) As Integer

Declare Function K_OBMGetPosttrigger Lib "DASSELL.DLL" (ByVal hFrame As
    Long, pCount As Long) As Integer

Declare Function K_OBMGetPretrigger Lib "DASSELL.DLL" (ByVal hFrame As
    Long, pCount As Long) As Integer

Declare Function K_OBMGetRepeatCount Lib "DASSELL.DLL" (ByVal hFrame As
Long, pCount As Long) As Integer

Declare Function K_OBMGetTriggerAddress Lib "DASSELL.DLL" (ByVal hFrame As
Long, pAddr As Long) As Integer

Declare Function K_OBMSetAddressStep Lib "DASSELL.DLL" (ByVal hFrame As
Long, ByVal nStep As Integer) As Integer

Declare Function K_OBMSetChanAry Lib "DASSELL.DLL" (ByVal hFrame As
Long, pArray As Integer) As Integer

Declare Function K_OBMSetMode Lib "DASSELL.DLL" (ByVal hFrame As Long,
ByVal nMode As Integer) As Integer

Declare Function K_OBMSetPortTrigger Lib "DASSELL.DLL" (ByVal hFrame As
Long, ByVal dwCount As Long) As Integer

Declare Function K_OBMSetRepeatCount Lib "DASSELL.DLL" (ByVal hFrame As
Long, ByVal dwCount As Long) As Integer

Declare Function K_OBMSetStartAddress Lib "DASSELL.DLL" (ByVal hFrame As
Long, ByVal dwAddr As Long) As Integer

Declare Function K_OBMSetTriggerAddress Lib "DASSELL.DLL" (ByVal hFrame As
Long, ByVal dwCount As Long) As Integer

Declare Function K_OBMStart Lib "DASSELL.DLL" (ByVal hFrame As   Long)
As   Integer

Declare Function K_OBMStatus Lib "DASSELL.DLL" (ByVal hFrame As Long,
pStatus As Integer, dwCount As Long) As Integer

Declare Function K_OBMStop Lib "DASSELL.DLL" (ByVal hFrame As Long, pStatus
As Integer, dwCount As Long) As Integer

Declare Function K_OpenDriver Lib "DASSELL.DLL" (ByVal szDASName As String,
ByVal szCfgName As String, phDrv As Long) As Integer

Declare Function K_RestoreChnGAry Lib "DASSELL.DLL" (pArray As Integer) As
Integer

Declare Function K_RestoreChnGAry Lib "DASSELL.DLL" Alias

"K_RestoreChnGAry" (pArray As Integer) As Integer

Declare Function K_SetAboutTrig Lib "DASSELL.DLL" (ByVal hFrame As Long,

ByVal dwSamples As Long) As Integer

Declare Function K_SetADCommonMode Lib "DASSELL.DLL" (ByVal hDev As

Long, ByVal nMode As Integer) As Integer

Declare Function K_SetBuf Lib "DASSELL.DLL" (ByVal hFrame As Long, pBuf As

Integer, ByVal dwSamples As Long) As Integer

Declare Function K_SetBufI Lib "DASSELL.DLL" Alias "K_SetBuf" (ByVal hFrame

As   Long, pBuf As Integer, ByVal dwSamples As Long) As Integer

Declare Function K_SetBufIL Lib "DASSELL.DLL" Alias "K_SetBuf" (ByVal hFrame

As Long, pBuf As Long, ByVal dwSamples As Long) As Integer

Declare Function K_SetBurstTicks Lib "DASSELL.DLL" (ByVal hFrame As Long,

ByVal nTicks As Integer) As Integer

Declare Function K_SetChn Lib "DASSELL.DLL" (ByVal hFrame As Long, ByVal

nChan As Integer) As Integer

Declare Function K_SetChnGAry Lib "DASSELL.DLL" (ByVal hFrame As Long,

pArray As Integer) As Integer

Declare Function K_SetClk Lib "DASSELL.DLL" (ByVal hFrame As Long, ByVal

nMode As Integer) As Integer

Declare Function K_SetClkRate Lib "DASSELL.DLL" (ByVal hFrame As Long, ByVal

dwDivisor As Long) As Integer

Declare Function K_SetContRun Lib "DASSELL.DLL" (ByVal hFrame As Long) As

Integer

Declare Function K_SetDITrig Lib "DASSELL.DLL" (ByVal hFrame As Long, ByVal

nOpt As Integer, ByVal nChan As integer, ByVal dwPattern As Long) As Integer

Declare Function K_SetDMABuf Lib "DASSELL.DLL" (ByVal hFrame As Long,

ByVal pBuf As Long, ByVal dwSamples As Long) As Integer

Declare Function K_SetDMABufB Lib "DASSELL.DLL" (ByVal hFrame As Long,
ByVal pBuf As Long, ByVal dwSamples As Long) As Integer

Declare Function K_SetExtClkEdge Lib "DASSELL.DLL" (ByVal hFrame As Long,
ByVal nMode As Integer) As Integer

Declare Function K_SetG Lib "DASSELL.DLL" (ByVal hFrame As Long, ByVal
nGain As Integer) As Integer

Declare Function K_SetGate Lib "DASSELL.DLL" (ByVal hFrame As Long, ByVal
nMode As Integer) As Integer

Declare Function K_SetPreTrig Lib "DASSELL.DLL" (ByVal hFrame As Long, ByVal
nCount As Integer) As Integer

Declare Function K_SetSSH Lib "DASSELL.DLL" (ByVal hFrame As Long, ByVal
nMode As Integer) As Integer

Declare Function K_SetStartStopChn Lib "DASSELL.DLL" (ByVal hFrame As Long,
ByVal nStart As Integer, ByVal nStop As Integer) As Integer

Declare Function K_SetStartStopG Lib "DASSELL.DLL" (ByVal hFrame As Long,
ByVal nStart As Integer, ByVal nStop As Integer, ByVal nGain As Integer) As
Integer

Declare Function K_SetSync Lib "DASSELL.DLL" (ByVal hFrame As Long, ByVal
nMode As Integer) As Integer

Declare Function K_SetTrig Lib "DASSELL.DLL" (ByVal hFrame As Long, ByVal
nMode As Integer) As Integer

Declare Function K_SetTrigHyst Lib "DASSELL.DLL" (ByVal hFrame As Long, ByVal
nHyst As Integer) As Integer

Declare Function K_SetTrigOut Lib "DASSELL.DLL" (ByVal hFrame As Long, ByVal
nMode As Integer, ByVal nticks As Long) As Integer

Declare Function K_SyncStart Lib "DASSELL.DLL" (ByVal hFrame As Long) As
Integer